Fundamentals of Positrodes for Proton Ceramic Electrochemical Cells

Madeeha Khalid Pedersen

Thesis for the degree of
Master of Science

Department of Chemistry
Faculty of Mathematics and Natural Science
UNIVERSITY OF OSLO

May 2019

© Madeeha Khalid Pedersen

2019

Fundamentals of Positrodes for Proton Ceramic Electrochemical Cells

Madeeha Khalid Pedersen

http://www.duo.uio.no/

Trykk: Reprosentralen, Universitetet i Oslo

“The general qualification necessary for scientific advancement is that which is usually denominated common sense, though added to this, imagination, induction, and trained logic, either of common language or mathematics, are important adjuncts.”

– Joseph Henry

Preface

This thesis represents part of the required work for the degree of Master of Science (M.Sc.) at the Department of Chemistry, Faculty of Mathematics and Natural Sciences, University of Oslo. The work was carried out at the group of Solid-State Electrochemistry (ELCHEM) under the supervision of Professor Truls E. Norby and Dr Ragnar Strandbakke during the period from August 2017 to May 2019.

First of all, I would like to thank my main and co-supervisor Professor Truls E. Norby and Dr Ragnar Strandbakke for their guidance, encouragement and motivation through the entire process. I much appreciate their patience and am thankful for the time they have spent on many insightful discussions. I am also grateful to Linn Katinka Emhjellen, Yang Hu, Amir Masoud Dayaghi and Einar Vøllestad for their help and support. A big thank to the whole research group for contributing to a great working environment.

Last, but not least, a big thank to my dear husband Hans Børge, for all the love and support, and the endless patience through this process.

Oslo, May 2019

Madeeha Khalid Pedersen

Summary

Proton Ceramic Electrochemical Cells (PCECs) based on mixed protonic and electronic conducting oxides are promising alternatives to Solid Oxide Electrochemical Cells (SOECs) for future energy technologies such as hydrogen separation, water electrolysis, and intermediate temperature fuel cells. One of the main obstacles in the development of competitive PCECs is the functionality of positrode materials. The electrode kinetics currently limits the performance of PCECs. The main challenge associated with this is the sparse knowledge of the reaction mechanism at the oxygen/steam side electrode, the *positrode*.

The primary goal of the thesis is to expand the understanding of the reactions taking place at positrode in PCECs and, moreover, identify the role of bulk vs surface transport in the electrode materials resulting from the mixed conduction by different charge-carriers. In this respect, performance and kinetics of two positrode materials, $BaGd_{0.8}La_{0.2}Co_2O_{6-\delta}$ (BGLC1082) and $SrFe_{0.75}Mo_{0.25}O_{3-\delta}$ (SFM25) has been thoroughly studied. Previous work has identified BGLC as a mixed protonic and electronic conductor (MPEC) in water-rich atmospheres at low temperatures (~400°C). SFM is mainly a *p*-type electronic conductor under oxidising conditions although some oxide ion conduction is reported at high temperatures. The main objective is to develop reaction models for describing the positrode reaction mechanism for both materials based on the research findings.

SFM was synthesised by solid-state reaction, while a supplier delivered powder of BGLC. Both materials were pressed to dense pellets and sintered. Sample characterisation exposed secondary phases containing cubic cobalt oxide on the BGLC surface. X-ray diffraction (XRD) analysis of BGLC showed a tetragonal structure of the double perovskite in addition to other peaks corresponding to secondary phases identified as cubic CoO and Co_3O_4. SFM exhibited a simple cubic structure and showed no secondary phases.

A model electrode with point contact was made by placing the dense positrode pellet vertically on the state-of-the-art proton ceramic $BaZr_{0.7}Ce_{0.2}Y_{0.1}O_3$ (BZCY72) button electrolyte. Counter and reference electrodes of Pt paste were carefully painted on the electrolyte before it was fired at 900°C. Potentiostatic Electrochemical Impedance Spectroscopy (EIS) with a four-probe three-electrode setup was utilised to study the electrode processes under controlled atmospheres and varying temperatures for both systems. The semi-circles at high, middle and low frequencies were assigned to the ohmic, charge transfer and mass transfer contribution, respectively.

The temperature dependencies were carried out at 700 – 350°C for BGLC and 650 – 400°C for SFM in wet air, at 0.20 atm pO_2 and 0.025 atm pH_2O. The following results revealed that the performance of BGLC, especially at lower temperatures was higher than that of SFM. The mass transfer activation energy for SFM was about 2.1 eV, while for BGLC, the value changed drastically from 1.4 to 0.4 eV at lower temperatures. BGLC exhibited polarisation resistance (R_p) of 5 kΩcm^2 at 350°C, which was relatively low compared to the R_p of 173 kΩcm^2 for SFM at 400°C.

Whereas the charge transfer resistance did not show any pO_2-dependency, the mass transfer $1/R_p$ increased with decreasing pO_2 with the order of ¼ for both materials. The pH_2O dependencies varied between ¼ and ½ for charge transfer resistances. In contrast to these results, the mass transfer $1/R_p$ exhibited a negative pH_2O-dependency for both oxides.

The main difference in the reaction models developed for the two systems was assumed to be situated in the charge transfer reaction. In Reaction Model 1, based on BGLC, the charge transfer was predicted to take place between the proton ceramic electrolyte and the positrode bulk, followed by bulk transport of protons. Conversely, in Reaction Model 2, developed for SFM, the charge transfer reaction occurs between electrolyte a TPB.

These suggestions were supported by the pre-exponential values of charge transfer, which was higher for BGLC that than for SFM, indicating more active reaction sites. Moreover, the double layer capacitance, $C_{dl,}$ of 10^{-5} Fcm^{-2} for BGLC was larger than that for SFM, which was about 10^{-8} $Fcm^{-2,}$ meaning a larger reaction area at BGLC than at SFM positrode.

The theoretical reaction rate models assume an abundance of adsorption sites on the surface, though the experimental results revealed that ambient water has a negative effect on the reaction rate. The surfaces appear to be saturated with OH^-/H_2O. The surface reaction between adsorbed oxide ions and proton followed by the water formation appeared to be rate-limiting steps for both positrode materials.

This work on the positrode reaction kinetics has contributed to a new understanding of the overpotential originated from the charge transfer reaction and, moreover, the relation to the mass transfer limitations.

List of Abbreviations

AC	Alternating Current
ASR	Area Spesific Resistance
BCY	Yttrium-doped $BaCeO_3$
BGCF	$BaGdCo_{1.8}Fe_{0.2}O_{6-\delta}$
BGLC	$BaGd_{0.8}La_{0.2}Co_2O_{6-\delta}$
BPC	$BaPrCo_2O_{6-\delta}$
BPCF	$BaPrCo_{1.4}Fe_{0.6}O_{6-\delta}$
BSCF	$Ba_{0.5}Sr_{0.5}Co_{0.8}Fe_{0.2}O_{3-\delta}$
B-V	Butler-Volmer
BZCY	$BaZr_{0.7}Ce_{0.2}Y_{0.1}O_3$
BZY	Yttrium-doped $BaZrO_3$
CE	Counter Electrode
CPE	Constant Phase Element
CT	Charge Transfer
DC	Direct Current
DL	Double Layer
EDS	Energy Dispersive Spectroscopy
EIS	Electrochemical Impedance Spectroscopy
GB	Grain Boundary
HOR	Hydrogen Oxidation Reaction
K-V	Kröger-Vink

LSCF	$La_{0.6}Sr_{0.4}Fe_{0.8}Co_{0.2}O_{3-\delta}$
LSM	$La_{0.8}Sr_{0.2}MnO_3$
MIEC	Mixed Ionic and Electronic Conductor
MPEC	Mixed Protonic and Electronic Conductor
MT	Mass Transfer
OCV	Open Circuit Voltage
O-MIEC	O^{2-}/e^- Mixed Ionic and Electronic Conductor
ORR	Oxygen Reduction Reaction
PBC	$PrBaCo_2O_{5+\delta}$
PCE	Proton Ceramic Electrolyser
PCEC	Proton Ceramic Electrochemical Cell
PCFC	Proton Ceramic Fuel Cell
PDF	Powder Diffraction File
PN	$Pr_2NiO_{4+\delta}$
RDS	Rate-Determining Step
RE	Reference Electrode
SEM	Scanning Electron Microscope
SFM	$SrFe_{0.75}Mo_{0.25}O_{3-\delta}$
SOE	Solid Oxide Electrolyser
SOEC	Solid Oxide Electrochemical Cell
SOFC	Solid Oxide Fuel Cell
SSD	$Sm_{0.5}Sr_{0.5}CoO_3$
TCO	Triple Conducting Oxides ($O^{2-}/H^+/e^-$)
TPB	Triple Phase Boundary

WE	Working Electrode
XRD	X-Ray Diffraction
YSZ	Yttrium stabilised ZrO_3

Contents

Preface V

Summary VII

List of Abbreviations IX

1 Introduction 1

1.1 Background and Motivation 1

1.2 Aims and Contents 4

2 Theory 7

2.1 Transport in Oxides 7
- 2.1.1 Defect chemistry 7
- 2.1.2 Kröger-Vink Notation 7
- 2.1.3 Defects in Oxides 8
- 2.1.4 Electrical Conductivity 11
- 2.1.5 Proton Transport 13

2.2 Electrochemical cells 14
- 2.2.1 Half-Cell Reactions 14
- 2.2.2 Redox Potential 15

2.3 The Positrode 18
- 2.3.1 Interfaces 18
- 2.3.2 Triple Phase Boundary 19
- 2.3.3 Reaction Mechanism – Positrode Processes 19
- 2.3.4 Electrode Polarisation 21

2.4 Reaction Kinetics and Thermodynamics 22
- 2.4.1 Rate of Reactions 22
- 2.4.2 Current-Potential Relation – Rate of Charge Transfer 23
- 2.4.3 Rate of Mass Transfer 27

2.5 Electrochemical Impedance Spectroscopy (EIS) 30
- 2.5.1 Direct and Alternating Current 30
- 2.5.2 Impedance and Admittance 30
- 2.5.3 Equivalent Circuit and Circuit Elements 32
- 2.5.4 Time Constants 32

2.5.5 Constant Phase Element 34
2.5.6 Impedance Spectra 35
2.5.7 Potentiostatic EIS 36

3 Literature 38

3.1 Proton Ceramic Electrochemical Cells 38
3.1.1 Proton Ceramic Electrolytes 39

3.2 Positrode Materials for PCECs 41
3.2.1 Mixed Ionic and Electronic Conductors 42
3.2.2 Mixed Protonic and Electronic Conductors 43

3.3 Positrode Kinetics 47
3.3.1 Reaction Mechanism 47
3.3.2 Elementary Reactions and Rate-Determining Step 48

4 Experimental 52

4.1 Sample Preparation 52
4.1.1 Positrode Materials 52
4.1.2 Proton Conducting Electrolyte 53

4.2 Sample Characterisation 54
4.2.1 Scanning Electron Microscopy (SEM) 54
4.2.2 X-Ray Diffraction (XRD) 54

4.3 Electrochemical Measurements 55
4.3.1 Instrumental Setup 55
4.3.2 Measurement Series 57

4.4 Data Analysis 58
4.4.1 Deconvolution 58
4.4.2 Electrochemical Analysis 59

4.5 Error and Uncertainty 59

5 Results 61

5.1 Sample Characterisation 61

5.2 Electrochemical Measurements 66
5.2.1 Temperature Dependencies 67
5.2.2 Partial Pressure Dependencies 71
5.2.3 Effect of DC Bias 77

5.3 Electrochemical Interpretation 78

6 Discussion 82

6.1 Crystal Structure and Phase Analysis 82

6.2 Positrode Performance 82

6.3 Positrode Reaction – Insight 83
6.3.1 Charge Transfer 83
6.3.2 Mass Transfer 85

6.4 Positrode Reaction Models and Kinetics 87
6.4.1 Elementary Reactions and Rate-Determining Step 89
6.4.2 Further Work 96

7 Conclusions 98

Bibliography 101

Appendix A 107

1 Introduction

1.1 Background and Motivation

Climate change is the biggest environmental threat that humanity is held accountable for. The society's dependency on the primary energy source, fossil fuels, stands before a great challenge. As the population grows and living standards develop, the demand for energy increases. Along with the industrial revolution, the increasing emission of greenhouse gases (GHG) such as CO_2, from burning fossil fuels has resulted in increasing global temperatures.

As a consequence of the limited amount of fossil fuels and their detrimental effects, the development of new technologies based on clean, efficient and climate-friendly energy as a combination of renewable resources and hydrogen has become a common interest worldwide. Within this scenario, fuel cell and electrolyser technologies are advocated to play a crucial role in the future.

“The Hydrogen Economy” has caught the most attention among several alternative sustainable energy approaches. The term refers to the idea of using hydrogen as a fuel in industrial systems for heating and transport. An energy system based on hydrogen and electricity is an attractive replacement for fossil fuels [1, 2]. Hydrogen is abundant in the environment, stored in water and hydrocarbons. Hydrogen can be produced from electrolysis of water from renewable electricity, compressed for storage and then utilised in fuel cells to regenerate the electricity when required for various applications [3].

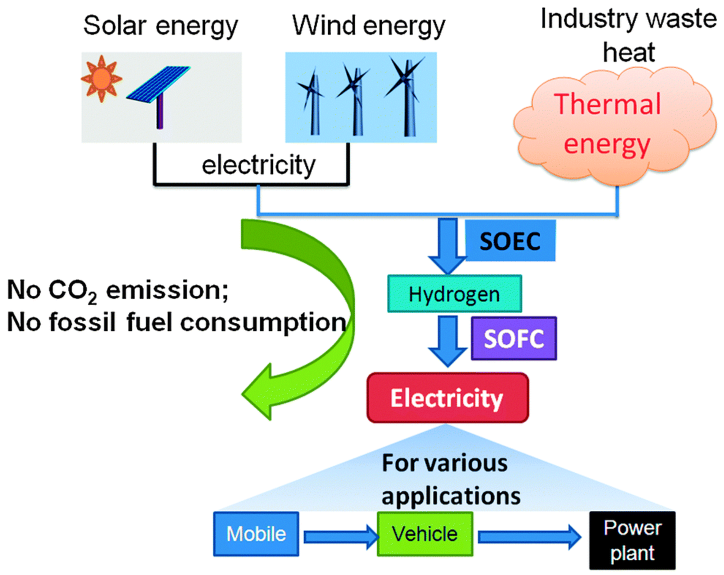
Solar energy
Wind energy
Industry waste heat
Thermal energy
electricity
SOEC
Hydrogen
SOFC
Electricity
No CO₂ emission;
No fossil fuel consumption
For various applications
Mobile
Vehicle
Power plant

Figure 1.1 Concept a system based on renewable energy sources based on fuel cells and electrolysers [4].

However, the electrolysis of water is not energy efficient. The energy of the produced hydrogen does not compensate the overpotentials needed to split water molecules. Most hydrogen is currently produced from hydrocarbons, and not renewable energy sources.

Commercially implemented fuel cells based on water-containing polymers struggle with poor tolerance toward fuel impurities and slow electrode kinetics due to low operating temperatures (< 100 °C). Among various types of fuel cells, solid oxide fuels cells (SOFCs) are attractive energy generators primarily due to their high conversion efficiency (> 60 %) and fuel flexibility and do not require expensive catalysts, such as platinum [5]. Also, they show potential both for commercial applications and large-scale power generation. The electrolytes in solid oxide electrochemical cells (SOECs) are typically oxide-ion conductors such as yttrium-stabilised ZrO_2 (YSZ), which require high operating temperatures (700 - 1000°C) [6]. High temperature solid oxide electrolysers (SOEs) have the advantage that they can utilise heat as part of the energy supplied to vaporise water to steam and thus lower the voltage and required electricity for the process. Regardless of the advantages, high operating temperatures in SOECs due to slow kinetics and high activation energies for ionic transport also introduces challenges such as lower durability, faster degradation rates and material instability. Furthermore, the accelerated thermal ageing results in a shorter lifespan of the cell as well as higher material cost [7]. Thus, it is desired to lower the operating temperature.

In this regard, Proton Ceramic Electrochemical Cells (PCECs), i.e. fuel cells (PCFCs) and electrolysers (PCEs) have received great attention most recently [5]. As the activation energy for proton transport is lower than that for oxide ion transport, lower operating temperatures are required (400 - 600°C) [8]. Thus, PCECs is a promising alternative to SOECs due to their potential to perform with higher efficiencies at lower temperatures. The proton conducting electrolyte is typically an acceptor doped oxide such as Y: $BaCeO_3$ (BCY) or Y: $BaZrO_3$ (BZY) [9].

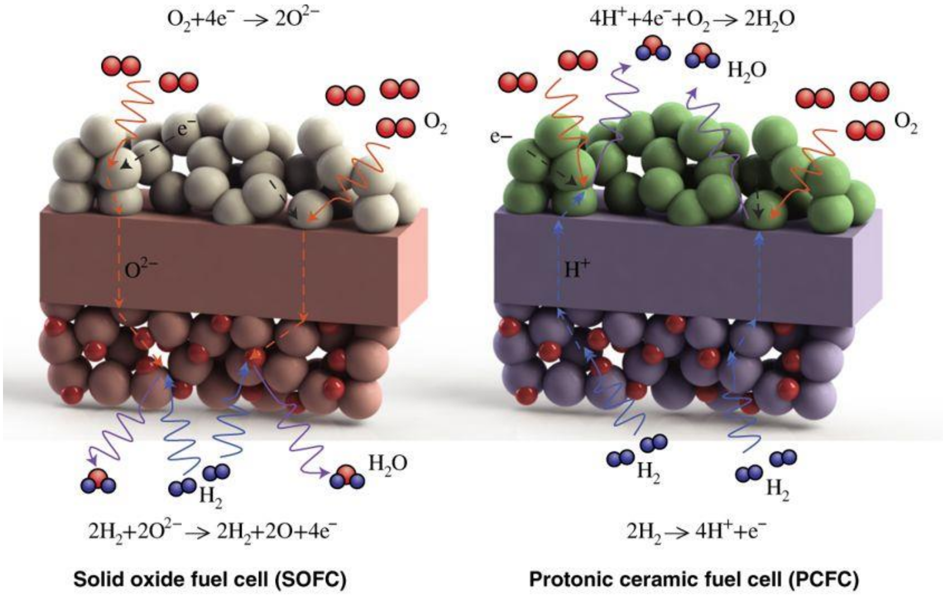
$O_2+4e^- \rightarrow 2O^{2-}$
e^-
O_2
O^{2-}
H_2O
H_2
$2H_2+2O^{2-} \rightarrow 2H_2+2O+4e^-$
$4H^++4e^-+O_2 \rightarrow 2H_2O$
H_2O
O_2
e−
H^+
H_2
H_2
$2H_2 \rightarrow 4H^++e^-$

Solid oxide fuel cell (SOFC)

Protonic ceramic fuel cell (PCFC)

Figure 1.2 Schematics of the electrode reaction taking place at the cathode (top) and anode (bottom) of SOFC and PCFC [5]. The reactions are reversed when operating is SOE and PCE mode. In PCECs, the oxygen/steam electrode is referred to as positrode while the hydrogen electrode is termed negatrode.

In PCFCs, the water is formed by at the positrode and hence does not dilute the fuel at the negatrode; this gives higher operating cell voltage and efficiency. The Nernst potential stays almost constant due to low pH_2O at the positrode until the maximum utilisation of fuel is reached, followed by a rapid decrease of the Nernst potential. On the contrary, the Nernst potential in SOFCs has a steep linear decrease, resulting in lower potential than in PCFCs at the same fuel utilisation [10].

As the development of proton ceramic electrolytes based on acceptor doped $Ba(Zr, Ce)O_3$ have matured, the necessity for high-performance electrodes has slowed the industrial application of PCECs. Regardless of the advantages, PCECs possesses some weaknesses which have a considerable influence on the electrode performance. The low operating temperatures reduce ionic conductivity and increase the polarisation resistances, especially at the positrode. Furthermore, PCECs suffers from low power output and poor chemical stability, and the performance is currently limited by electrode kinetics [11]. There are also problems with PCECs related to production cost, degradation issues, and space charge effects in grain boundaries limiting the proton conductivity.

Electrode materials for SOECs have been frequently applied in PCECs but have resulted in high polarisation resistances [8]. Research on SOECs electrode materials suggests that the best electrode materials are those with mixed ionic and electronic conductivity (MIEC). Materials with mixed O^{2-}/e^- conductivity, also referred to as O-MIECs, are good candidates for SOFC cathode applications but limits the positrode reaction to the reaction zone, i.e. the Triple Phase boundary (TPB). In order to extend the reaction zone, materials with mixed protonic and ionic conductivity (MPEC) are desired.

BGLC exhibit mixed protonic and electronic (*p*-type) conductivity, the low activation energy for water splitting and has the lowest reported apparent polarisation resistance (Rp) of 0.05 Ωcm^2 at 650°C currently. Together with Faradaic efficiencies close to 100%, BGLC is thus considered as the-state-of-the-art positrode material [12-15]

1.2 Aims and Contents

Having knowledge of the interactions of species at the interface of an electrochemical cell forms a significant part in the fundamentals of electrochemistry. The kinetics of the electrode, the double layer structure and interfacial singularities belongs to this area. The literature on the reaction at the positrode suggests that it involves hydroxide surface species and that these may compete with oxygen adsorption. However, the details of these mass transfer steps, and especially the charge transfer reaction step, for PCECs are mostly unspecified.

Given the limitations associated with a lack of stable MIEC positrode materials and insufficient understanding of the rate-limiting elementary steps, two different positrode materials are investigated. The first positrode material is the double perovskite oxide $BaGd_{0.8}La_{0.2}Co_2O_{6-\delta}$ (BGLC1082) which exhibit protonic conductivity under wet atmospheres, have the lowest reported apparent polarisation resistance [12] currently and is a promising candidate for PCEC application. $SrFe_{0.75}Mo_{0.25}O_{3-\delta}$ (SFM25), a cubic perovskite oxide, exhibit high electronic conductivity and have shown good performance in SOECs due to the high thermally and chemical stability in both oxidising and reducing atmospheres [16]. The positrode materials will be synthesised, pressed to dense pellets before sintering. The samples will be characterised by means of electron microscopy and x-ray diffraction.

Point contact electrode made of the positrode on a thick electrolyte of Y-doped $BaZr_{0.7}Ce_{0.2}Y_{0.1}O_3$ (BZCY72), with counter- and reference electrodes of platinum (Pt) will be studied by potentiostatic electrochemical impedance spectroscopy (EIS) under controlled atmospheres. Impedance spectroscopy is used to delineate the electrode response in ohmic, charge transfer, and mass transfer contributions. Variations in temperatures, oxygen and water vapour partial pressures allow modelling of these contributions further into partial protonic, oxide ionic, and electronic currents. The dependencies of the positrode resistances and kinetic parameters will be investigated concerning temperature, pO_2 and pH_2O. Through evaluating all the parameters for the different positrodes, their performance will be compared and further analysed regarding rate limiting the availability of reactant species and microstructural sites.

Furthermore, pre-exponential factors are interpreted in terms of active area and length of reaction zones and compared with the area and circumference of the point electrode footprint on the electrolyte, as analysed by light microscope.

The main aim of the thesis is to expand the understanding of the reactions taking place at positrode in PCECs and, moreover, identify the role of bulk vs surface transport in the electrode materials resulting from the mixed conduction by different charge-carriers.

In this respect, reaction models for describing the positrode reaction mechanism for both systems will be developed based on results from the electrochemical measurements. Owing to the lower activation temperature for proton transport than that of oxide-ions, it is assumed that diffusion of oxygen species is highly unfavourable at the tested temperatures and will thus not be considered. The significant difference between the two models is presumed the charge transfer across electrolyte and BGLC bulk vs TPB. The following path of the proton transport may be a decisive factor for the reaction kinetics.

Reaction orders will be calculated utilising Butler-Volmer theory, Nernst equation and Langmuir adsorption isotherm. RDS will be pointed out for the reaction models by comparing the theoretical reaction orders with experimental. Also, a further goal is to determine the source of the overpotential limiting the positrode reaction, which will provide new information about how to address the issues related to the materials properties, microstructure and geometry.

With this, the final goal to be able to predict directions to go in terms of microstructure, materials compositions, and conditions to optimise the performance of positrodes for PCECs.

2 Theory

Firstly, an introduction of the general theoretical background relevant to this work is presented. Further, theoretical concepts are elaborated and described concerning the system of interest

2.1 Transport in Oxides

Oxides that consists of two or more different cations are known as mixed oxides. The cation can, in some cases, be of the same element in different oxidation states. The diversity in the oxidations states, ionic radii or coordination numbers of the cations gives rise to many different properties of mixed oxides. The presence of defects facilitates transport in oxides, and the temperature and oxygen and water vapour partial pressure firmly impact their concentration and mobility.

The formation and transport of defects are crucial to understanding other mechanisms and properties of the material.

2.1.1 Defect chemistry

Any imperfection or deviation from the ideal periodicity in crystalline solids is called a defect. At temperatures above 0 K, entropy favours the formation of defects to reduce Gibbs energy.

In this thesis, non-dimensional defects, known as point defects, are primarily in focus. Point defects may be intrinsic, i.e. formed by internal reactions within the material or extrinsic, i.e. formed through interaction with other phases, such as gases in the surrounding. Defect electrons or electron holes that are relatively free to move in the crystal structure are electronic defects. Electronic defects are formed by internal excitation of valence electrons or in association with structural defects.

2.1.2 Kröger-Vink Notation

Kröger-Vink (K-V) notation for point defects is applied to formulate chemical equations for defects reactions and is further used to describe defect equilibria under varying conditions. In general form $\mathrm{A}_\mathrm{s}^\mathrm{c}$, *A* refers to the entity of interest as an element or vacancy (v). Subscript *s* refers to the site of occupation, usually a chemical symbol or an interstitial (i). Superscript *c* denotes the effective charge on the defect, defined as the difference between the valence state of the defect and the valence state of the occupied state. The notations for effective charges are superscript $^\bullet$, $^/$ and $^\mathrm{x}$ for positive, negative and neutral defects, respectively. Electrons and holes are denoted $e^{/}$ and $h^{\bullet}$, respectively. Defects reactions are written similarly as ordinary chemical reactions and are balanced by conservation of mass, charge and ratios of sites.

2.1.3 Defects in Oxides

The activity of metal in metal oxides is negligibly small compared to that of the oxygen under most experimental conditions. Thus, the non-stoichiometry is, in general, a consequence of the oxygen exchange between the oxide and the atmosphere. Such materials have either excess or deficiency of oxygen compared to that of the stoichiometric material. The degree of non-stoichiometry varies with temperature and oxygen partial pressure.

An ideal perovskite oxide has the general formula ABO_3. The cations occupying the A-site are large, often alkaline or alkaline earth metals, compared to the B-site cations, often transition metals.

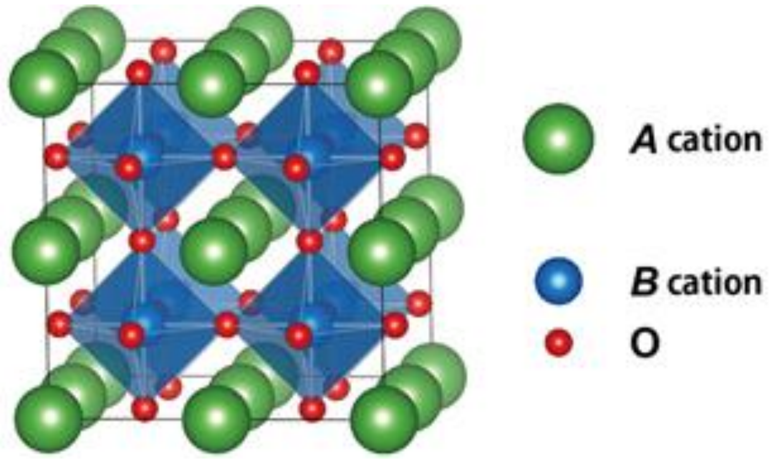

Figure 2.1 Crystal structure of a cubic perovskite oxide [17].

Proton ceramic electrolytes are typically hydrated, acceptor doped perovskite oxides such as Y-doped $BaZrO_3$ (BZY). The proton conductivity of $BaZrO_3$ can be increased by introducing an aliovalent dopant to promote further defect formation. Barium zirconate is commonly acceptor doped with Y^{3+}, forming monovalent, effectively negative sites: Y'_{Zr}, which may be charge compensated by oxygen vacancies.

$$Y_2O_3 = 2Y'_{Zr} + v_O^{\bullet\bullet} + 3O_O^{\times} \tag{2.1}$$

Oxygen vacancies can also be formed intrinsically by Schottky disorder or oxygen deficiency, charge compensated by metal vacancies (v''_{Ba} and v''''_{Zr}) or electrons. The acceptors and vacancies, under dry, or protons under wet conditions are dominating defects while the electronic defects are minor in a typical electrolyte material.

An ionic conductor such as BZY also exhibits electronic defects in small concentrations which contributes to *n*- and *p*-type conductivities. These minority defects may form to charge compensate for defects that are caused by deviation from the stoichiometry of the material due temperature, partial pressure or doping.

The defect reaction of formation of oxygen vacancies at low oxygen partial pressures, charge-compensated by electrons, through the release of oxygen gas is written as:

$$\mathrm{O_O^{\times} = v_O^{\bullet\bullet} + 2e' + \frac{1}{2}O_2(g)} \tag{2.2}$$

At high oxygen partial pressures, the oxygen vacancies oxidise to form electron holes, which are the minority defects:

$$\mathrm{\frac{1}{2}O_2(g) + v_O^{\bullet\bullet} = 2h^{\bullet} + O_O^{\times}} \tag{2.3}$$

Equations 2.2 and 2.3 shows that the concentration of oxygen vacancies, electrons and holes is dependent on oxygen partial pressure. The equilibrium constant[1] for the reduction reaction:

$$\mathrm{K_{red}} = [\mathrm{v_O^{\bullet\bullet}}]\mathrm{n}^2 p_{\mathrm{O_2}}^{1/2} \tag{2.4}$$

The corresponding equilibrium constant for the oxidation becomes:

$$\mathrm{K_{ox}} = \frac{\mathrm{p}^2}{[\mathrm{v_O^{\bullet\bullet}}]} p_{\mathrm{O_2}}^{-1/2} \tag{2.5}$$

The concentration of acceptor defects is constant. Under dry conditions and at low oxygen partial pressures, oxygen vacancies are dominating defects. The electroneutrality can be assumed:

$$2[\mathrm{v_O^{\bullet\bullet}}] = [\mathrm{Y'_{Zr}}] = \mathrm{constant} \tag{2.6}$$

---

[1] The standard partial pressure is $p^0_{\mathrm{O_2}}$=1 atm and defect activity or site fraction is assumed $[\mathrm{O_O^{\times}}]$ = 1. They are therefore not included in the equilibrium constants.

Following that, the concentration of the minor electronic defects is dependent on oxygen partial pressure:

$$\mathrm{n} = (2\mathrm{K_{red}})^{1/2}[\mathrm{Y'_{Zr}}]^{-1/2}\, p_{\mathrm{O_2}}^{-1/4} \tag{2.7}$$

Likewise, the concentration of electron holes is dependent on oxygen partial pressure:

$$\mathrm{p} = (2\mathrm{K_{ox}})^{1/2}[\mathrm{Y'_{Zr}}]^{1/2}\, p_{\mathrm{O_2}}^{1/4} \tag{2.8}$$

Furthermore, metal oxides may form protonic defects in hydrogen-containing atmospheres. In a water-rich atmosphere, the oxygen vacancies hydrates and form protons:

$$\mathrm{H_2O(g)} + \mathrm{v_O^{\bullet\bullet}} + \mathrm{O_O^{\times}} = 2\mathrm{OH_O^{\bullet}} \tag{2.9}$$

The corresponding equilibrium constant for the hydration reaction is a function of the standard hydration entropy and enthalpy:

$$\mathrm{K_{hyd}} = \frac{[\mathrm{OH_O^{\bullet}}]^2}{[\mathrm{v_O^{\bullet\bullet}}]}\, p_{\mathrm{H_2O}}^{-1} = \exp\left(\frac{\Delta \mathrm{S^{\circ}_{hyd}}}{\mathrm{R}}\right)\exp\left(-\frac{\Delta \mathrm{H^{\circ}_{hyd}}}{\mathrm{RT}}\right) \tag{2.10}$$

The formation of electrons in the hydrated state can be described by combining Equations 2.2 and 2.9:

$$\mathrm{H_2O(g)} + \mathrm{O_O^{\times}} = 2\mathrm{OH_O^{\bullet}} + 2\mathrm{e'} + \frac{1}{2}\mathrm{O_2(g)} \tag{2.11}$$

In the same way, the formation of electron holes can be given by combining Equations 2.3 and 2.9:

$$\frac{1}{2}\mathrm{O_2(g)} + 2\mathrm{OH_O^{\bullet}} = 2\mathrm{O_O^{\times}} + 2\mathrm{h^{\bullet}} + \mathrm{H_2O(g)} \tag{2.12}$$

Moreover, in a wet atmosphere, the oxygen vacancies are hydrated; thus, the acceptors are charge compensated by protons:

$$[\mathrm{OH}_\mathrm{O}^\bullet] = [\mathrm{Y}'_\mathrm{Zr}] = \mathrm{constant} \tag{2.13}$$

The proton concentration in oxides varies when oxygen vacancies are the dominating defects and protons are in the minority:

$$[\mathrm{OH}_\mathrm{O}^\bullet] = \mathrm{K}_\mathrm{hyd}^{1/2}[\mathrm{v}_\mathrm{O}^{\bullet\bullet}]^{1/2}\, p_{\mathrm{H_2O}}^{1/2} \tag{2.14}$$

The concentration of the electronic defects under wet conditions are dependent on partial pressures of oxygen and water vapour:

$$\mathrm{n} = \left(\mathrm{K}_\mathrm{hyd}\mathrm{K}_\mathrm{red}\right)^{1/2}[\mathrm{Y}'_\mathrm{Zr}]^{-1}\, p_{\mathrm{H_2O}}^{1/2}\, p_{\mathrm{O_2}}^{-1/4} \tag{2.15}$$

$$\mathrm{p} = \left(\frac{\mathrm{K}_\mathrm{ox}}{\mathrm{K}_\mathrm{hyd}}\right)^{1/2}[\mathrm{Y}'_\mathrm{Zr}]\, p_{\mathrm{H_2O}}^{-1/2}\, p_{\mathrm{O_2}}^{1/4} \tag{2.16}$$

2.1.4 Electrical Conductivity

When a material with charge carrier *i* with charge z_ie is exposed to an electric field, E, the charge carrier will be affected by a force proportional to the electric field and the concentration, c_i. This force gives rise to a current with current density *i* expressed as:

$$i_i = \sigma_i E = z_i e c_i u_i E \tag{2.17}$$

In Equation 2.17, σ_i is the partial electrical conductivity of the charged species, *i*, and u_i is the corresponding mobility. The unit for the electrical conductivity is Siemens per cm (S/cm). The concentration of the charge carriers is measured in the number of charge carrier of type *i* per cm^3. The mobility of the charge carriers is expressed in units of cm^2/Vs.

The total electrical conductivity is the sum of partial conductivities of the contributing charge carriers:

$$\sigma_{tot} = \sum_i \sigma_i \tag{2.18}$$

Often, one type of charge carrier dominates the charge transport; hence, the contributions from the minority carriers are, in many cases, neglected. The mobilities of the electronic charge carriers are much higher than the mobilities of ionic charge carriers, even with a smaller concentration, most MIEC oxides are electronic conductors at high temperatures. The ionic mobility increases with increasing temperature. In order to increase the ionic conductivity of an oxide, two parameters of the charge carriers can be modified: their concentrations and mobilities.

The electronic conductivity is related to the motion of mobile electrons and electron holes through the material. The contributions to electronic conductivity from electrons or holes are known as n- and p-type conductivity, respectively. The total electronic conductivity may be expressed in terms of the concentration of the electronic charge carriers, electrons n and holes p with their corresponding mobilities u_n and u_p:

$$\sigma_{el} = \sigma_\mathrm{n} + \sigma_\mathrm{p} = e\mathrm{n}u_\mathrm{n} + e\mathrm{p}u_\mathrm{p}, \tag{2.19}$$

in which e is the elementary charge, and σ_n and σ_p represent the n- and p-type conductivities, respectively.

Ionic conductivity occurs in the presence of vacancies or interstitials of ions, i.e. if the crystal structure has enough space for ions to hop from one site to another. Ionic conduction is due to thermally activated ion hopping. The charge carrier mobility and electrical conductivity are related to diffusion and follow the Nernst-Einstein relationship:

$$D_i = u_i \frac{k_B T}{z_i e} = \sigma_i \frac{k_B T}{c_i (z_i e)^2}, \tag{2.20}$$

where D_i is the diffusion coefficient of species i, k_B is the Boltzmann's constant ($8.6174 \cdot 10^{-5}$ eV/K) and T is the temperature in Kelvin.

The Nernst-Einstein relation interprets that the conductivity will have a temperature dependence, which is the product of the dependencies on the diffusion coefficient and the formation of the charge carriers. The Arrhenius-type plot gives the activation energy

$$\sigma_i = \frac{\sigma_0}{T} exp\left(-\frac{\Delta E_a}{k_B T}\right) \tag{2.21}$$

The pre-exponential factor, σ_0, contains the formation entropy and the entropy of mobility. Likewise, the activation energy involves the enthalpy of formation and mobility.

In general, the electronic conductivity of oxides at elevated temperatures is dependent on oxygen partial pressure, pO_2, in the atmosphere. As shown in Equations 2.15 and 2.16, the concentration of electrons and electron holes have a dependency of - ¼ and ¼ respectively on oxygen partial pressure. Following this, as illustrated in Figure 2.2, the electronic conductivity changes from *n*- to *p*-type with increasing pO_2.

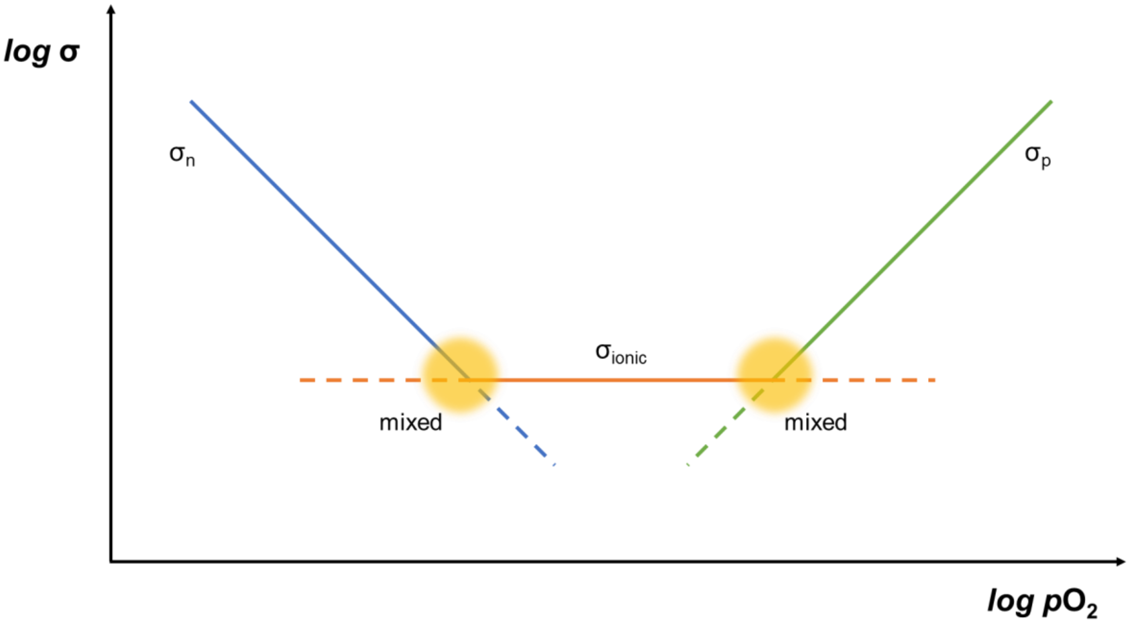

Figure 2.2 Electronic and ionic conductivity as a function of oxygen partial pressure. The slope for *n*- and *p*-type conductivities are typical - ¼ and ¼, respectively. Ionic conductivity is not dependent on pO_2.

2.1.5 Proton Transport

In principle, protons do not occupy lattice positions due to their small size but are instead bound to oxide ions. Protons are mobile through two primary mechanisms: the *Grotthuss mechanism,* i.e. free transport and the vehicle mechanism. The Grotthus mechanism occurs by rotational diffusion of the proton around an oxygen ion, followed by proton hopping between adjacent oxide ions. After each hop, the proton in the hydroxide rotates until a new possibility for proton transfer occurs and reorients in the electron cloud and aligns for succeeding hop. The rotation and reorientation are assumed to involve activation energy, and the hop itself is considered to be the rate-determining step. This mechanism is acknowledged to be the primary mode for proton transport in oxides such as BZY.

In the vehicle mechanism, protons are considered to be carried as passengers on oxide ions. The hydroxide ion may transfer by an oxygen vacancy or as a hydroxide ion interstitial.

2.2 Electrochemical cells

Electrochemical cells convert chemical energy into electrical energy from redox reactions or consume electrical energy to drive a chemical reaction. When current flows through an electrochemical cell, the cell potential changes from the equilibrium potential; this change, also known as the overpotential, can be described as the required potential for the electrode reaction to occur. In other words, the potential needed to overcome the energy barrier, e.g. for the transport of species at the electrode surface or across the interface of electrode/electrolyte.

An electrochemical cell consists of two electrodes separated by an electrolyte. The electrolyte is an ionic conductor, and the electrodes are typically electronic conductors, connected through an external circuit. When an ionic and an electronic conductor are in contact, a Faradaic reaction may occur. A Faradaic reaction is a heterogeneous reaction at an electrode/electrolyte interface that involves electron transfer, i.e. redox reactions. Hence a Faradaic current is a current generated by electron transfer.

2.2.1 Half-Cell Reactions

In this work, the electrode of interest is the one at which the oxygen/steam half-cell reaction takes place. In fuel cell mode, the electrode works as a cathode and reduces the oxygen, likewise in electrolyser mode, the electrode oxidises water and is thus an anode. In both modes, the standard reduction potential is higher than the counter electrode, and the electrode is hereafter called *positrode*. The hydrogen electrode is hence called *negatrode*.

In a proton ceramic fuel cell (PCFC), hydrogen gas oxidises and forms protons and electrons at the negatrode. The electrons flow through an external circuit, generating electricity, while the protons migrate through a dense ceramic electrolyte to the cathode. At the positrode/electrolyte interface, they react with oxygen gas and form water. In electrolytic cells, however, the reactions are reversed. Energy from an external source is applied to drive the redox reactions in the opposite or non-spontaneous direction.

The electrochemical reactions at each half-cell:

Hydrogen reaction at the negatrode:

$$\mathrm{H_2(g) \rightleftarrows 2H^+ + 2e^-} \tag{2.22}$$

Oxygen reaction at the positrode:

$$\mathrm{O_2(g) + 4H^+ + 4e^- \rightleftarrows 2H_2O(g)} \tag{2.23}$$

Net cell reaction is the sum of the two half-cell reactions:

$$\mathrm{2H_2(g) + O_2(g) \rightleftarrows 2H_2O(g)} \tag{2.24}$$

2.2.2 Redox Potential

The driving force for a half-cell (often redox) reaction is the electrochemical potential gradient across the electrolyte/electrode interface.

The potential difference stems from the different electrochemical potentials. The difference in electrochemical potential, $\Delta\tilde{\mu}$, is the sum of the difference in chemical potential, $\Delta\mu$, and electrical potential, $\Delta\phi$:

$$\Delta\tilde{\mu}_i = \Delta\mu_i + z_i F \Delta\phi_i \tag{2.25}$$

Here z is the charge of species i and F is the Faradays constant (96 485 C/mol).

The chemical potential describes how the Gibbs free energy varies with the number of moles, n, of component i while temperature, pressure and the number of moles of all other components are constant. The electrochemical potential for electrons is equal to the Fermi level. The chemical potential for a chemical species i is defined by:

$$\mu_i = \left(\frac{\partial G}{\partial n_i}\right)_{T,p,n_{j\neq i}} = \mu_i^\circ + RT\ln(a_i) \tag{2.26}$$

In Equation 2.26, μ_i° is the chemical potential in the standard state. The activity, a, is related to the concentration c through $a = \gamma c$, where γ is the activity coefficient.

$$\Delta G = \Delta G^{\circ} + RT \ln Q \tag{2.27}$$

Here R is the gas constant (8.3145 J/Kmol), T is the temperature in Kelvin. At equilibrium $\varDelta G=0$, thus the reaction quotient Q is replaced by the equilibrium constant K. The Gibbs energy is the chemical energy that governs the feasibility of chemical reactions. The standard[2] Gibbs energy, $G°$, have the same unit as Gibbs free energy, kJ/mol. When all species involved in the reaction are in their standard state,

$$\Delta G^{\circ} = -nFE^{\circ}_{cell} \tag{2.28}$$

In order to measure the potential of an electrode, a complete electrochemical cell with two electrodes and two half-cell Faradaic reactions are required. The standard cell potential, E°_{cell}, is the difference in standard the electrical potentials of the two electrodes:

$$E^{\circ}_{cell} = \phi^{\circ}_{cathode} - \phi^{\circ}_{anode} = -\frac{\varDelta G^{\circ}}{nF} \tag{2.29}$$

Another way to look at the relation given in Equation 2.29 is that the electrical work by the redox reaction is $nF\phi$, which is equal to the Gibbs free energy, $\varDelta G$.

Change in the electrochemical potential for the positrode reaction given in Equation 2.22:

$$\Delta\tilde{\mu} = 2\mu_{H_2O(g)} - \mu_{O_2(g)} - 4\tilde{\mu}_{H^+} - 4\tilde{\mu}_{e^-} \tag{2.30}$$

where for an ideal gas,

$$\mu_{H_2O} = \mu^{\circ}_{H_2O} + RT \ln\left(p_{H_2O}\right) \tag{2.31}$$

$$\mu_{O_2} = \mu^{\circ}_{O_2} + RT \ln\left(p_{O_2}\right) \tag{2.32}$$

Also,

$$\tilde{\mu}_{H^+} = \mu^{\circ}_{H^+} + RT \ln(a_{H^+}) + F\phi_{H^+} \tag{2.33}$$

---

[2] Standard state: 10^5 Pa (1 bar), 298.15 K if temperature is not defined.

$$\tilde{\mu}_{e^-} = \mu^{\circ}_{e^-} - F\phi_{e^-} \tag{2.34}$$

At equilibrium, $\Delta\tilde{\mu} = 0$, Equation 2.34 can then be written:

$$2\mu_{H_2O(g)} = \mu_{O_2(g)} + 4\tilde{\mu}_{H^+} + 4\tilde{\mu}_{e^-} \tag{2.35}$$

By inserting Equations 2.31-2.34 into Equation 2.30 and combining with Equation 2.35:

$$-4F(\phi_{e^-} - \phi_{H^+}) = -4F\Delta\phi^{\circ} = RT\ln\left(\frac{p^2_{H_2O}}{a^4_{H^+}p_{O_2}}\right) \tag{2.36}$$

By dividing Equation 2.36 on *-4F*, the electrical potential can be expressed as:

$$\Delta\phi = \Delta\phi^{\circ} - \frac{RT}{4F}\ln\left(\frac{p^2_{H_2O}}{a^4_{H^+}p_{O_2}}\right), \tag{2.37}$$

where $\Delta\phi^{\circ}$ is the standard half-cell potential.

Multiplying the chemical equation with a numerical factor will increase the standard Gibbs energy for the reaction while the standard cell potential will remain unchanged. That is because the number of electrons that are transferred increases by the same factor; hence, the cell potential is not dependent on the (physical) size of the cell.

Nernst Potential

The net cell voltage, also known as the cell potential, E_{cell}, is the difference in electrical potential between the oxidation and reduction reactions at the two electrolyte/electrode phase boundaries. It is a measure of the energy required to move one unit of charge when the electrochemical cell is at equilibrium. When the overall reaction is at equilibrium, the potential difference is zero, and there is no net current flow, this is referred to as the Nernst potential, E_N, also known as the open circuit voltage (OCV) of the positrode:

$$E_N = E^\circ + \frac{RT}{4F}\ln\left(\frac{pO_2 a_{H^+}^4}{pH_2O^2}\right) \tag{2.38}$$

The standard potential E^o is the cell potential when all reactants and products are in their standard state. Since all activities are then 1, the reaction quotient Q is also equal to 1 (ln Q = 0).

The relation given in Equation 2.38 is also used to determine reaction equilibrium constants and concentration potentials. The Nernst equation is only valid for reversible reactions and at equilibrium.

2.3 The Positrode

2.3.1 Interfaces

In contrast to Faradaic reactions, a non-Faradaic reaction causes a current flow by capacitive properties of the electrical double layer in an electrode. Non-Faradaic processes involve chemical changes at the electrode/electrolyte interface without the occurrence of electron transfer, i.e. no current flow. However, non-Faradaic processes can generate external transient currents.

When an electrode and an electrolyte is brought into contact, a reaction may occur and induce an electric potential across the two phases. The accumulation and separation of charge are referred to as an electric double layer at the interface. Generally, it is a charge in one phase which is balanced by a charge of opposite sign on the contacting phase. The structure of the double layer is analogous to a parallel plate capacitor, i.e. layers of charges of opposite sign are separated by a fixed distance. The double layer capacitance is given by:

$$C_{dl} = \varepsilon\frac{A}{d} = \frac{q}{\Delta E} \tag{2.39}$$

In Equation 2.39, ε is permittivity (also known as the dielectric constant) of the material between the plates; A is the area of the plates separated by distance d. The double layer capacitance, C_{dl}, is a measure of the amount of electric charge, q, stored, which is linearly proportional to the potential difference, ΔE, between the plates. The unit of capacitance is farad, F (C/V).

2.3.2 Triple Phase Boundary

In solid state electrochemistry, electrode reactions take place not only across the electrode/electrolyte phase boundary but also at the interface between the electrode surface and the gas phase. The area of contact between these three different phases, i.e. electrons, ions and gas, is referred to as the triple phase boundary (TPB). TPB is the reaction zone, thus expanding the TPB will increase the reaction rate as well as cell performance.

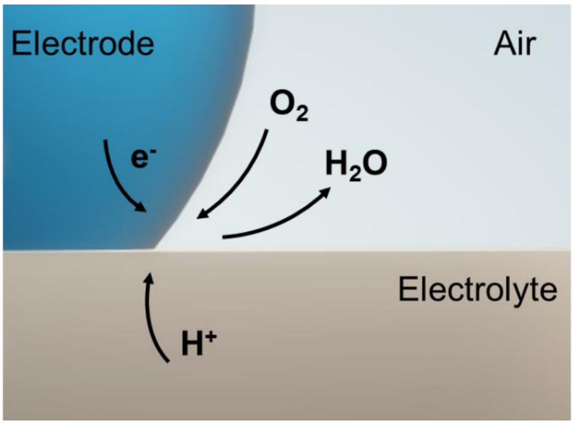

Figure 2.3 The triple phase boundary when the electrode is a pure electronic conductor.

The oxygen reduction reaction that occurs at the positrode can be written as follow:

$$O_2(\text{gas}) + 4e^-(\text{electrode}) + 4H^+(\text{electrolyte}) \rightleftarrows 2H_2O(\text{gas}) \qquad (2.40)$$

Different mechanisms transport the reactants to the triple phase boundary to carry out this reaction. The combined effects of reaction kinetics coupled with the transfer of mass and electrons, establish the total resistance.

2.3.3 Reaction Mechanism – Positrode Processes

It is expected that the reaction mechanism at the positrode in a PCFC includes the following processes:

i. Surface adsorption of oxygen
ii. Electron transfer (reduction or ionisation of adsorbed oxygen)
iii. Proton transfer from the electrolyte (charge transfer)
iv. Proton diffusion (through electrode bulk or surface) to the reaction zone
v. Formation and desorption of water

The positrode reaction is a multistep process that can be divided into at least two distinguishable partial contributions; the mass transfer (*mt*) and charge transfer (*ct*). The kinetics at the electrode surface is associated with mass and charge transfer. These two processes are driven by the concentrations of the species, the interactions between them and their mobility. The mass transfer involves the exchange of chemical species in the gas phase, surface and bulk, i.e. diffusion, adsorption and desorption. In general, the charge transfer is associated with electron transfer, i.e. the reduction reaction of oxygen species. However, in the positrode reaction, the charge transfer process describes the exchange or transfer of charges across a phase boundary. In this context, the charge transfer is the transfer of protons from the electrolyte bulk to the electrode bulk or the TPB. The reaction pathways depend on the properties of the electrode material, which also impact the rate of reaction.

Altogether, the positrode reaction can be divided into the following elementary reactions:

$$\mathrm{O_2(g)} + *_{\mathrm{ads}} \xleftrightarrow{\text{adsorption (mt)}} 2\mathrm{O_{ads}} \tag{2.41}$$

$$\mathrm{O_{ads}} + 2\mathrm{e}^- \xleftrightarrow{\text{electron transfer}} \mathrm{O_{ads}^{2-}} \tag{2.42}$$

$$\mathrm{H_{BZY}^{+}} \xleftrightarrow{\text{charge transfer (ct)}} \mathrm{H_{TPB}^{+}} \tag{2.43}$$

$$\mathrm{O_{ads}^{2-}} + 2\mathrm{H_{TPB}^{+}} \xleftrightarrow{\text{mass transfer}} \mathrm{H_2O_{ads}} \xleftrightarrow{\text{desorption (mt)}} \mathrm{H_2O(g)} + *_{\mathrm{ads}} \tag{2.44}$$

The diffusion processes are excluded as diffusion is not a chemical reaction. The reaction rate of each step depends on various factors such as involved species, properties of the positrode material, active reaction sites (*) microstructure and geometry. When a net current runs, all reaction steps are considered to be in virtual equilibrium, except the rate-determining step (RDS), which causes the overpotential. The RDS is the slowest of these steps, thus determines the overall reaction rate.

In order to get a better understanding of the electrode reactions and understand the kinetics, it is necessary to look further into the details of the physical chemistry of both charge and mass transport processes.

2.3.4 Electrode Polarisation

An electrode is said to be totally polarised if no Faradaic current flows through the electrode/electrolyte interface at any potential, i.e. no charge transfer occurs across the interface. The electrode behaves like a capacitor and shows a significant change in the potential for the current flow, which is a displacement current. An ideally non-polarisable electrode remains at its equilibrium potential when a current is applied across the electrode/electrolyte interface. The electrode behaves like a resistor as the charge freely crosses the interface.

When current runs through an electrochemical cell, there will be potential losses. The overpotential, η, measures the extent of polarisation:

$$\eta = E - E_N \tag{2.45}$$

The overpotential is caused by a deviation from the equilibrium potential when a current is running through the cell and depends on the current density. Current-voltage curves for electrochemical cells obtained under steady-state conditions are known as polarisation curves.

The sources of electrode polarisation are associated with its overpotential;

Ohmic polarisation leads to an ohmic overpotential, η_{ohm}, and arises from resistance in the electrode or the electrolyte when an electric current is running. Ohmic overpotential is the linear region of the polarisation curve and is related to ohms law, $\eta_{ohm} = IR$, where R is the sum of electronic, ionic and contact resistance. Ohmic losses occur during the electronic or ionic transport through the electrode and the electrolyte.

Charge transfer polarisation (also known as activation polarisation) describes the electrochemical loss mechanism taking place mainly at the TPB and leads to a charge transfer overpotential, η_{ct} due to slow kinetics, i.e., slow charge transfer. Charge transfer overpotential is the potential difference required to overcome the energy barrier for the charge transfer reaction.

Mass transport or *concentration polarisation* is caused by sluggishness in the supply of reactants to the electrode reaction sites or removal of products. The concentration difference between the electrode and the electrolyte due to the flow of current through the interface leads to a mass transport overpotential, η_{mt}. The current differs distribution of ions at the electrode/electrolyte interface, and a concentration gradient leads to an overpotential, as a result of the slow mass transport process.

Polarisation resistance, R_p, is the transition resistance between the electrode and the electrolyte. Chemical reactions at the electrode increase the resistance to the current flow in the electrochemical cell.

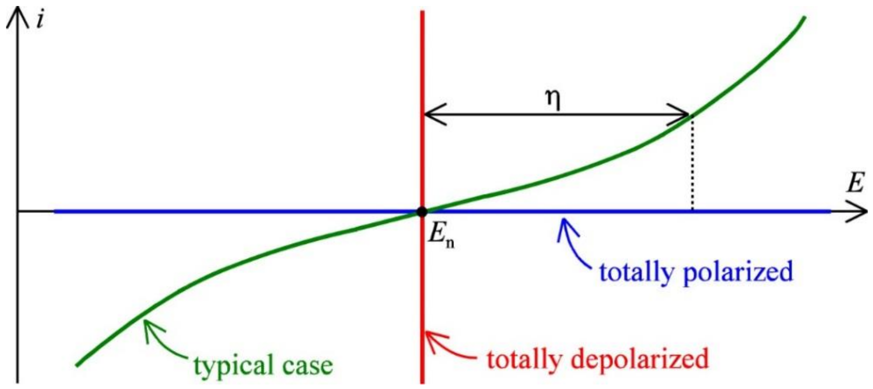

Figure 2.4 Polarisation curves.

The total voltage output can be written:

$$E_{tot} = E_N - \eta_{ct} - \eta_{mt} \tag{2.46}$$

2.4 Reaction Kinetics and Thermodynamics

In thermodynamic equilibrium, both reactions (forward and backwards) occurs at the same rate. When a potential is applied, the current flow gives rise to two phenomena: electrode reactions and transport of species across the electrode/electrolyte interface. While the thermodynamics describes the feasibility of an electrode reaction to occur, kinetics define the reaction rates.

2.4.1 Rate of Reactions

When elementary reaction steps take place at the electrode surface, the interface and the phase boundaries, there are energy barriers to overcome. The kinetics of a chemical reaction is dependent on the activation energy and the temperature through the Arrhenius equation:

$$k = A_o exp\left(-\frac{E_a}{RT}\right) \tag{2.47}$$

The rate constant k of the reaction is expressed in terms of a pre-exponential factor A_o, also known as the frequency factor, and an exponential term containing the activation energy, E_a, measured in J/mol. The temperature independent pre-exponential depends on geometric factors, the concentration of species, active reaction sites and vibrational attempt rates. As illustrated in

Figure 2.4, the activation energy is the height of the energy barrier. The reaction coordinate is, in general, a geometrical perception, which includes molecular distances, bond angles and interatomic distance. The maximum energy, also known as the transition state or activated complex, is where the molecules have the right distance, configuration and distortion to form the product.

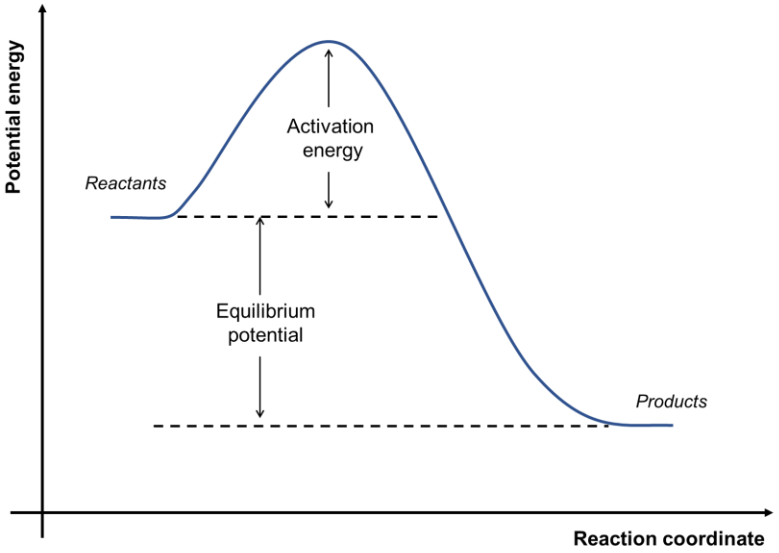

Figure 2.5 Potential energy surface for an exothermic reaction such as oxygen reduction. The maximum point of the activation energy is the transition state or activated complex – where the coordination of the reactant molecules is desirable to proceed with the reaction and form products.

Moreover, the rate of a process is also affected by available active sites on a surface. A high value of the pre-exponential factor indicates an increased number of active sites. Consequently, the rate of reaction will also increase.

2.4.2 Current-Potential Relation – Rate of Charge Transfer

Whereas an electron transfer is considered to be fast quantum mechanical tunnelling, an electrochemical charge transfer requires thermal activation to overcome the energy barrier to move across the phase boundary.

Faradaic current describes the rate of an electrochemical reaction. The Faradaic rate is a general correlation between current and the rate at which a species reduces or oxidises. Since all electrode reactions are heterogeneous, they typically occur at the electrode surface or phase boundaries and are dependent on mass transfer and kinetic limitations. It is thus beneficial to describe current per unit area, i.e. current density i:

$$i = \frac{I}{A} = nFr \tag{2.48}$$

Current, I, per area, A (cm^2), give the rate, r, for an electrochemical reaction. Unit for current density, i, is Acm^{-2}. The rate can be considered in terms of volume, area or length of the reaction zone. The unit is hence reliant on the designation. However, in this work, the rate will be expressed in terms of activity; the unit is thus mol·cm^{-2} s^{-1}.

Considering the charge transfer reaction at the electrolyte/positrode interface described in Equation 2.43, a proton sitting on oxygen in BZY jumps to another oxygen at the TPB:

$$\mathrm{OH}^{\bullet}_{\mathrm{O(BZY)}} + \mathrm{O}^{\times}_{\mathrm{O(TPB)}} \rightleftarrows \mathrm{OH}^{\bullet}_{\mathrm{O(TPB)}} + \mathrm{O}^{\times}_{\mathrm{O(BZY)}} \tag{2.49}$$

The forward reaction describes the transfer of charge from the proton conducting electrolyte to the TPB (or positrode bulk) where it eventually reacts with adsorbed oxide ions to form water in fuel cell mode. The reaction is thus cathodic. Correspondingly, the backward reaction is anodic when running in fuel cell mode. The following reaction rates for the cathodic and anodic charge transfer reaction, respectively, can be written as:

$$r_c = k_c a_{H^+_{BZY}} = -\frac{i_c}{nF} \tag{2.50}$$

$$r_a = k_a a_{H^+_{TPB}} = \frac{i_a}{nF} \tag{2.51}$$

In terms of current density, the charge transfer reaction rate becomes:

$$i_{ct} = i_a + i_c = nF\left[k_a a_{H^+_{TPB}} - k_c a_{H^+_{BZY}}\right] \tag{2.52}$$

The activations of H$^+$ are in equilibrium with $p\mathrm{O}_2$ and $p\mathrm{H}_2\mathrm{O}$ in the atmosphere. The rate of a charge-transfer reaction depends on the potential difference between the two phases. As mentioned, charge-transfer is a thermally activated process and needs activation energy to overcome the energy barrier.

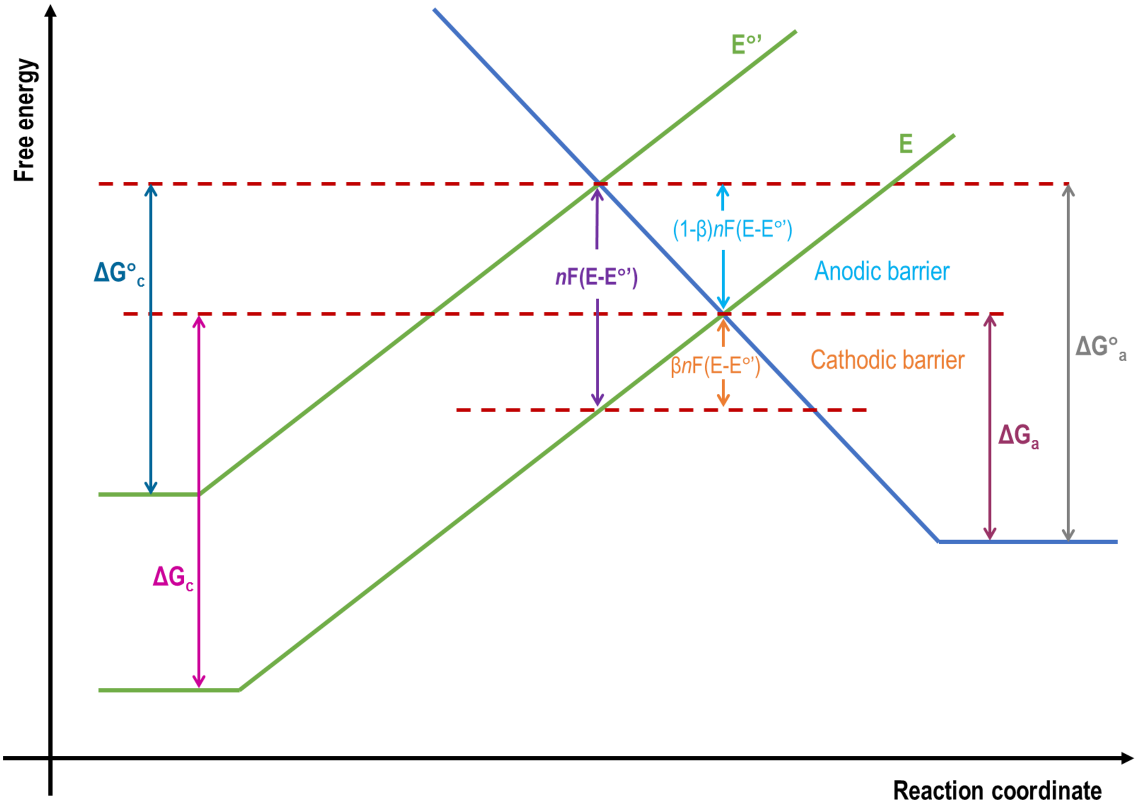
Free energy
E°'
E
ΔG°c
nF(E-E°')
(1-β)nF(E-E°')
Anodic barrier
ΔG°a
βnF(E-E°')
Cathodic barrier
ΔGa
ΔGc
Reaction coordinate

Figure 2.6 The change in standard free energy when a potential E is applied. The reactant is stabilised, i.e. lowered energy by nF(E-E°') and the height of the barrier is decreased by (1-β)nF(E-E°'). The net change in the cathodic barrier is βnF(E-E°'). Assume E°'=E$_{eq}$.

The Gibbs energy of activation for the cathodic and anodic reaction, respectively, when a potential *E* is applied:

$$\Delta G_c = \Delta G_c^\circ + \beta nF(E - E^{\circ\prime}) \tag{2.53}$$

$$\Delta G_a = \Delta G_a^\circ - (1-\beta)nF(E - E^{\circ\prime}) \tag{2.54}$$

The charge transfer coefficient, *β*, also called the symmetry factor, is the fraction of *E*-*E*°', applied to the cathodic reaction, which leads to a change in the rate constant. By substituting Equations 2.53 and 2.54 in the Arrhenius equation, the following rate constant is expressed as:

$$k_c = A_{o,c}\, exp\left(\frac{-\Delta G_c}{RT}\right) = A_{o,c}\, exp\left(\frac{-\Delta G_c^\circ}{RT}\right) \boldsymbol{exp}\left(\frac{\boldsymbol{-\beta nF(E - E^{\circ\prime})}}{\boldsymbol{RT}}\right) \tag{2.55}$$

$$k_a = A_{o,a}\, exp\left(\frac{-\Delta G_a}{RT}\right) = A_{o,a}\; exp\left(\frac{-\Delta G_a^\circ}{RT}\right) \boldsymbol{exp}\left(\frac{\boldsymbol{(1-\beta)nF\left(E - E^{\circ'}\right)}}{\boldsymbol{RT}}\right) \tag{2.56}$$

The first expression in Equation 2.55 and 2.56, including pre-exponential and standard Gibbs free energy, is potential independent and can be written as $k_c^\circ = k_a^\circ = k_{ct}^\circ$. The second expression (in bold) is potential dependent. The charge transfer current density becomes:

$$i_{ct} = i_a + i_c = nFk_{ct}^\circ \left(a_{H_{TPB}^+} exp\left(\frac{(1-\beta)nF\eta_{ct}}{RT}\right) - a_{H_{BZY}^+} exp\left(-\frac{\beta nF\eta_{ct}}{RT}\right)\right) \tag{2.57}$$

The charge transfer overpotential η_{ct} is the difference between the applied potential E and the equilibrium potentials $E^{\circ'}$.

Although the net current is zero at equilibrium, there is still Faradaic activity, which is known as the exchange current density, i_0. It is the continuous current in both directions, i.e. the cathodic current is balanced by the anodic current. The exchange current density is equal in the magnitude of cathodic or anodic current, $i_{0,ct} = i_a = -i_c$ and when $n = 1$:

$$i_{0,\mathrm{ct}} = Fk_{ct}^\circ a_{H_{TPB}^+} exp\left(\frac{(1-\beta)F\eta_{ct}}{RT}\right) = Fk_{ct}^\circ a_{H_{BZY}^+} exp\left(-\frac{\beta F\eta_{ct}}{RT}\right) = Fk_{ct}^\circ a_{H_{BZY}^+}^{(1-\beta)} a_{H_{TPB}^+}^{\beta} \tag{2.58}$$

The exchange current density is proportional to the standard rate constant k_{ct}°, which is a measure of the kinetic facility of a charge transfer reaction. A large value of exchange current density means that a small overpotential is needed to attain sizeable current flow, whereas a large overpotential is needed if the exchange current is small. The exchange current density increases with increasing activity (concentration) of protons in the electrolyte and TPB (or electrode bulk) with an order of ½ if β = ½.

The current-potential relation is given by the Butler-Volmer equation (B-V), which in general is written:

$$i = i_0 \left[exp\left(\frac{\alpha nF\eta}{RT}\right) - exp\left(-\frac{\beta nF\eta}{RT}\right)\right] \tag{2.59}$$

The sum of the anodic charge-transfer coefficient α and the cathodic charge-transfer coefficient β is equal to 1 and $\alpha = 1-\beta$. The Butler-Volmer equation describes how the charge-transfer current is proportional to the overpotential, which is the required potential to overcome the energy barrier associated with the electrochemical reaction.

If the overpotential is small ($\eta << RT/\beta nF$), a Taylor expansion of the exponential term the Butler-Volmer equation can be written in a linear form:

$$i_{ct} = i_{0,ct}\frac{nF\eta_{ct}}{RT} \tag{2.60}$$

The ratio between the charge-transfer overpotential and current density is known as the charge transfer resistance:

$$R_{ct} = \frac{\eta_{ct}}{i_{ct}} = \frac{RT}{i_{0,ct}nF} \tag{2.61}$$

If the overpotential is large ($\eta >> RT/nF$), one of the exponential terms, either the anodic or the cathodic, in the B-V equation (2.59) will go towards zero, and the other exponential term will dominate. In other words, the reaction becomes irreversible in one direction.

For large anodic overpotentials, the current density becomes:

$$i = i_a = i_0\left[exp\left(\frac{\alpha nF\eta}{RT}\right)\right] \Longrightarrow \ln|i| = \ln|i_a| = \ln i_0 + \frac{\alpha nF}{RT}\eta \tag{2.62}$$

The Tafel equation assumes that the reaction rate in one direction is negligible compared to the reaction rate in the opposite direction.

$$\eta_{ct} = -\frac{RT}{\alpha nF}\ln i_0 + \frac{RT}{\alpha nF}\ln i = a + b\log i \tag{2.63}$$

where a is the first term containing ln i_0, multiplied with 2.303 and b is called the Tafel slope.

The higher the Tafel slope, the slower the kinetics of the electrode reaction.

2.4.3 Rate of Mass Transfer

The process of mass transport, as described above, includes the exchange of chemical species between the gas phase, electrode surface and electrolyte bulk, which includes diffusion, adsorption and desorption. The rate of mass transfer processes, expressed in terms of the rate constant and concentration, is indirectly dependent on the electrode potential.

In solid-state electrochemistry, the first step of the electrode[3] reaction is considered as adsorption of oxygen gas. The adsorption can either be associative or dissociative. The rate of adsorption is expressed using the Langmuir isotherm, assuming that on the surface, there are a certain number of binding sites per unit area.

The fractional coverage, $\Theta = \frac{occupied\ sites}{vacant\ sites}$, describes the extent of surface coverage.

One of the assumptions of Langmuir isotherms is that all sites are equivalent, and adsorption can only proceed within monolayer coverage, i.e. $\Theta < 1$.

Under isothermal conditions, the adsorbate is assumed to behave as an ideal gas. The adsorption rate, i.e. the rate of change of the surface coverage for associative adsorption of oxygen gas at the electrode surface is:

$$\frac{d\Theta}{dt} = p_{O_2} k_{ads}^{+}(1-\Theta) - k_{des}^{-}\Theta \tag{2.64}$$

The k_{ads}^{+} and k_{des}^{-}, given in $s^{-1}Pa^{-1}$, represent the rate constants for adsorption and desorption reaction respectively. The partial pressure is given in Pa^{-1}.

In equilibrium, the rate of adsorption is equal to the rate of adsorption:

$$\Theta = K_{O_2} p_{O_2}(1-\Theta) \tag{2.65}$$

Here $K_{O_2} = k_{ads}^{+}/k_{des}^{-}$.

$$\Theta = \frac{K_{O_2} p_{O_2}}{1 + K_{O_2} p_{O_2}} \tag{2.66}$$

Langmuir isotherm for dissociative adsorption of oxygen gas at the electrode surface:

$$\frac{d\Theta}{dt} = p_{O_2} k_{ads}^{+}(1-\Theta)^2 - k_{des}^{-}\Theta^2 \tag{2.67}$$

which at equilibrium is written as:

$$\Theta^2 = K_{O_2} p_{O_2}(1-\Theta)^2 \tag{2.68}$$

---

[3] Referring to the reaction mechanisms of cathode and anode reactions for SOFCs and PCFCs as proposed in literature where the first step is considered as adsorption of gas.

$$\Theta = \frac{\sqrt{K_{O_2}p_{O_2}}}{1+\sqrt{K_{O_2}p_{O_2}}} = \frac{K_{O_2}^{1/2}p_{O_2}^{1/2}}{1+K_{O_2}^{1/2}p_{O_2}^{1/2}} \tag{2.69}$$

At large surface coverage, the $\Theta \approx 1$. However, under ideal, i.e. dilute condition, the number of vacant adsorption sites are considered infinitely large, and Θ can thus be neglected.

The adsorption is often followed by electron and charge transfer before diffusion. The so-called chemical diffusion is a physical process which causes transport of a species due to a concentration gradient. As the diffusion process is not a chemical reaction, it is not influenced by changes in the potential. However, the particle flux of diffusion can be expressed by Fick's 1st law:

$$J_i = -D_i\frac{d\Theta_i}{dx} \tag{2.70}$$

The flux, J, i.e. number of moles of particles of type i, is expressed in terms of the diffusion coefficient D (cm^2s^{-1}), and the concentration gradient $d\Theta/dx$ (adsorbed particles cm^{-1}). The unit of J is number or mole of particles $cm^{-2}s^{-1}$. The negative sign indicates that the particles move down the concentration gradient.

Although an applied potential does not influence the diffusion process, it can still affect the reaction rate through concentration limitations. If the mass transfer is limited by diffusion, the diffusion coefficient, defined by the Nernst-Einstein relation in Equation 2.20, contribute to the R_{ct} at low-frequencies and give the mass transfer resistance, R_{mt}.

When the positrode reaction is mass transfer limited, the concentration differences of the involved species result in mass transfer overpotential, which is a sum of all overpotentials. The concentration changes are compensated by either decreasing the Nernst potential or increasing the charge transfer loss. The total rate, i.e. current density, for the positrode reaction can be expressed in terms of the B-V equation:

$$i = i_a + i_c = nFk_{mt}^{\circ}\left(p_{H_2O}^2 exp\left(\frac{(1-\beta)nFE_{tot}}{RT}\right) - p_{O_2}exp\left(-\frac{\beta nFE_{tot}}{RT}\right)\right) \tag{2.71}$$

Following this, the total exchange current density for the total reaction then becomes:

$$i_0 = nFk_{mt}^{\circ}p_{H_2O}^2 exp\left(\frac{(1-\beta)nFE_{tot}}{RT}\right) = nFk_{mt}^{\circ}p_{O_2}exp\left(-\frac{\beta nFE_{tot}}{RT}\right) = nFk_{mt}^{\circ}\, p_{O_2}^{1/2}p_{H_2O}^{1/2} \tag{2.72}$$

2.5 Electrochemical Impedance Spectroscopy (EIS)

EIS is a method to characterise the dynamics of an electrochemical system by using alternating current (AC) to analyse the response of an electrochemical system to an applied sinusoidal voltage. The electrochemical impedance of the electrode reaction is dependent on frequency. The impedance varies as the frequency of the applied voltage changes.

2.5.1 Direct and Alternating Current

A direct current (DC) is a continuous current where the electric charge only flows in one direction. Because DC does not have a change in sign, the frequency is zero.

An alternating current (AC) is an electrical current with varying magnitude and direction. Due to this periodically reverse of charge direction, the waveform for an AC can be sinusoidal. The frequency, *f*, angular frequency, $\omega = 2\pi f$, and the amplitude U_0 characterise the sine wave voltage for AC voltage

$$U = U_0 \sin(\omega t) \tag{2.73}$$

U is the potential at time t. The product of angular frequency and time, ωt, is the phase angle.

The sine wave voltage produces current with the same wave pattern and frequency, but a different amplitude, I_0

$$I = I_0 \sin(\omega t + \theta) \tag{2.74}$$

The phase angle, θ, expresses the shift in phase from the applied signal that results from capacitive or inductive elements in the circuit.

2.5.2 Impedance and Admittance

Impedance, *Z*, is a measure of complex resistance of alternating current (AC) through a circuit. While resistance mainly applies to DC-circuits, impedance also includes AC-circuits.

Similarly, electrical impedance is the measure of the opposition to current flow when an AC voltage is applied. Ohm’s law expresses this for AC as for DC. The unit for impedance is ohm (Ω).

$$Z(\omega) = \frac{U}{I} = \frac{U_0 \sin(\omega t)}{I_0 \sin(\omega t + \theta)} = |Z| \frac{\sin(\omega t)}{\sin(\omega t + \theta)} \tag{2.75}$$

Electrical impedance is a complex number involving a real component, given by the resistance, R, in phase with the applied voltage and an imaginary component involving inductive or capacitive reactance, X, which is out of phase. The two components are independent. Impedance expressed as a complex number in the Cartesian form:

$$Z^* = R + jX \tag{2.76}$$

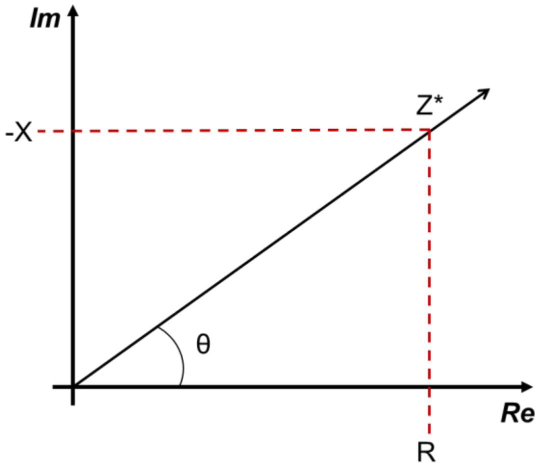

Figure 2.7 A graphical representation of complex impedance.

The resistance expresses the number of charges that pass through a resistor when the current and voltage is in phase. The reactance, in contrast, represents the imaginary flow of charges and is frequency dependent. Capacitors stores electrical charges which give negative reactance. Similarly, when a current running through an inductor (coil) changes direction, a magnetic field will induce a voltage, the inductive reactance is thus positive. The total reactance is the sum of capacitive and inductive reactance:

$$X = X_C + X_L = -\frac{1}{\omega C} + \omega L \tag{2.77}$$

Where C and L are capacitance and inductance, respectively. Combining equation 2.76 and 2.77, the total impedance for is:

$$Z^* = R - j\frac{1}{\omega C} + j\omega L \quad (2.78)$$

An ideal resistor does not have any reactance. Likewise, an ideal capacitor (or inductor) has no resistance. The unit for capacitance and inductance is farad (F = Ω^{-1}s) and Henry (H = Ωs), respectively.

In contrast to impedance, admittance, *Y*, is a measure of how easy an alternating current (AC) flows through a circuit and is expressed as a complex number with conductance, *G*, as the real component and susceptance, *B*, as the imaginary component:

$$Y^* = G + jB \quad (2.79)$$

Admittance is measured in S (Siemens).

The relation between impedance and admittance is:

$$Y^* = \frac{1}{Z^*} = \frac{I}{U} \quad (2.80)$$

2.5.3 Equivalent Circuit and Circuit Elements

In this thesis, the EIS measurements aim to describe the electrochemical processes taking place at the electrode/electrolyte interface. Equivalent circuits are a tool to analyse the contributions of different processes of the system by the electrical response. Electrical elements as resistor, capacitor or inductor (RCL) are connected to complex impedance elements in an equivalent electrical circuit to give a simplified representation of the electrochemical system.

Two or more elements connected in series experiences the same current and the total potential difference is the sum of the potential difference of each element. When connected in parallel, the elements experience the same voltage; hence, the total current is the sum of the current flowing through each element. The impedance contributions are added for elements connected in series, while for elements connected in parallel the admittance contributions are added.

2.5.4 Time Constants

The time constant is considered as a measure of the rate of change in the electric double layer and determines the time interval over which voltages, charges and currents changes in the circuit. The time constant, τ, is given by:

$$\tau = \frac{1}{\omega_{max}} = RC, \quad (2.81)$$

where ω_{max} is the relaxation frequency, R and C is the resistance and capacitance, respectively. The time constant of the circuits defines the timescales on which the different processes occur. Equivalent circuit model for the complex plane fit consist of several time constants. A semi-circle with peak frequency is characteristic of a single time constant in the Nyquist plot. The number of the time constants is equal to the number of RC-parallels.

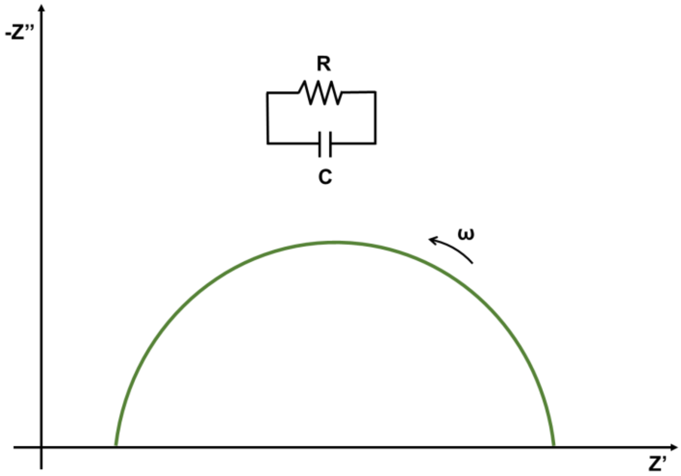

Figure 2.8 Schematics of impedance spectra containing a single time constant.

The magnitude of the capacitance can be assigned to a particular phenomenon in the sample.

Table 2.1 Capacitance values and their possible interpretation [18].

Capacitance (Fcm^{-1})	Responsible effect
10^{-12}	Bulk (b)
10^{-11} - 10^{-8}	Grain boundary (gb)
10^{-8} - 10^{-6}	TPB/interface
10^{-6} - 10^{-3}	Charge transfer (ct)
10^{-3} - 1	Mass transfer (mt)

2.5.5 Constant Phase Element

The constant phase element (CPE) is a model element developed to describe a non-ideal response of a capacitor. A CPE is recognised as a depressed semi-circle in the Nyquist plot, indicating a distribution of time constants. It is a combination of resistance and capacitance and contains admittance.

$$Z_{CPE} = \frac{1}{Y_0 (j\omega)^n} \tag{2.82}$$

The parameter *n* is typically between 0 and 1 and is related to the phase angle. If n = 1, Y_0 acts like pure capacitor and yields no resistive behaviour.

The pseudo-capacitance is calculated by:

$$C_{CPE} = Y_0^{\frac{1}{n}} R_p^{\frac{1}{n}-1}, \tag{2.83}$$

where R_p is the corresponding polarisation resistance.

Gerischer Element

The Gerischer impedance represents processes at very low frequencies and describes reactions that typically occur along the diffusion path and impacts the concentration of at least one of the diffusing species (e.g. by forming electrochemically inactive complexes). In other words, the Gerischer element accounts for a distributed chemical-electrochemical reaction. The Gerischer impedance is:

$$Z_{GE} = \frac{1}{Y_0 \sqrt{K_a + j\omega}} \tag{2.84}$$

When ω → 0, the term K_a represents the effective transfer rate of the chemical reaction. For the Gerischer impedance, Y_0 represents the electrochemical admittance at $\omega = 1$ rad/s$^{1/2}$.

Randles circuit

The most common model of an electrochemical interface is the Randles circuit. The typical Randles circuit consists of an electrolyte resistor in series with the parallel combination of polarisation or charge transfer resistance and double layer capacitance. At low frequencies, the effects of mass transfer are considered.

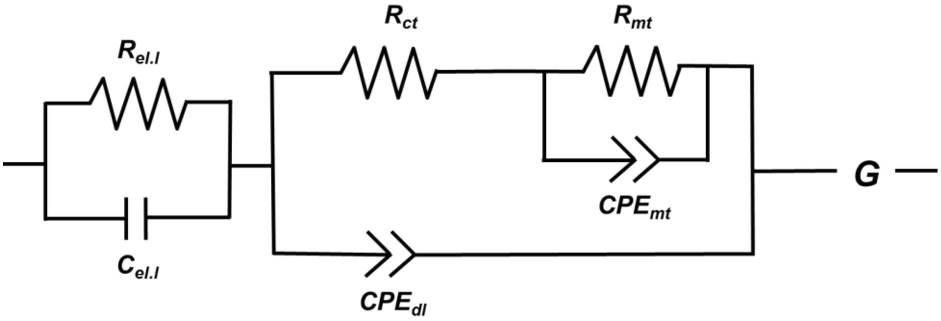

Figure 2.9 Randles-type equivalent circuit used to resolve the impedance spectra in this work. The first RC-parallel is assigned to the electrolyte, i.e. bulk or grain boundary resistance. The second RCPE(RCPE)-parallel is associated with electrode processes along with the Gerischer element. All resistances are coupled in series.

2.5.6 Impedance Spectra

EIS sweeps contain information about specific parts of the system. The impedance spectra of am electrochemical system measured over a broad range of frequencies are often represented graphically by Bode and Nyquist plots. A suitable equivalent circuit that describes the physical system is fitted to the spectra to extract the values of interest.

Bode plot

A Bode plot gives a combination of two plots of frequency response on a logarithmic scale. One shows the relationship between input and output impedance in terms of the magnitude and second shows the phase shift. The horizontal axis shows the frequency, while the vertical axis showed the magnitudes and phase shift. The frequency dependence is visible in the Bode plot; single components are easier understood. However, the Bode plot is not sensitive to changes in the system measured.

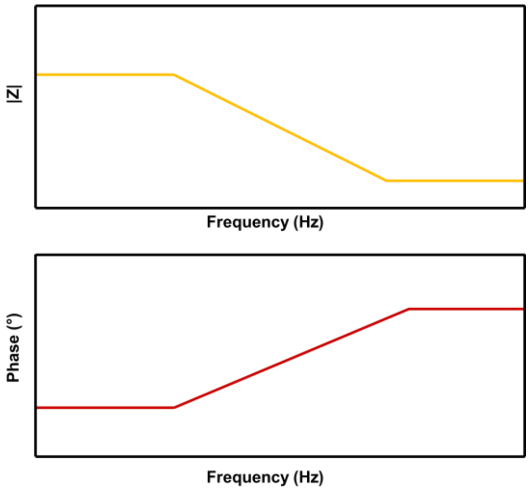

Figure 2.10 Illustration of a typical Bode plot for a parallel resistor and capacitor, as illustrated in Figure 2.8.

Nyquist plot

The Nyquist plot is the most common graphical representation of measured impedance values for both real and imaginary components. The negative reactance is plotted against the resistance at the same frequency. The Nyquist plot is sensitive to changes in the system and hence more complicated to interpret.

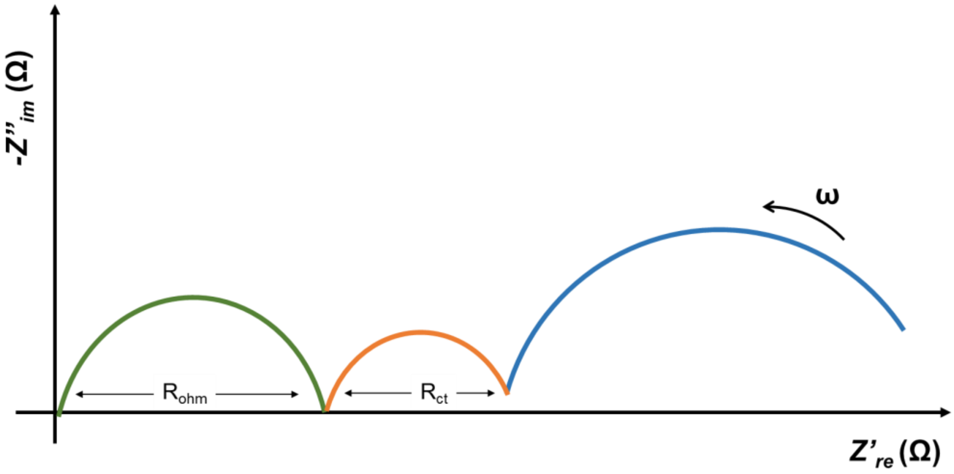

Figure 2.11 Illustration of a Nyquist plot with three time-constants. The first semi-circle is typically the bulk response at high frequencies while the third semi-circle is due to the slow processes at the electrode surface such as mass transfer and diffusion.

2.5.7 Potentiostatic EIS

Among several techniques for electrochemical impedance measurements depending on the system of interest, potentiostatic EIS was utilised in this work. The impedance is measured by applying a sinusoidal AC-voltage to an electrochemical cell and measure the responding sine wave current signal. A potentiostat controls the potential of an electrode while measuring the current flowing through it.

The three-electrode setup is commonly used in aqueous electrochemistry, where the reference electrode (RE) is immersed in the electrolyte solution. However, in solid-state electrochemistry, the RE is commonly placed on the electrolyte surface next to the working electrode with a distance of three times the electrolyte thickness to avoid potential gradients along the electrolyte surface. The three electrode configuration consists of a working electrode (WE), which is the electrode of interest, a reference electrode (RE) and a counter electrode (CE), also known as an auxiliary electrode. The reference electrode aims to control the potential of the WE without passing any current. The potential is applied between the WE and the RE, while the current flows through WE and CE. This way, a constant reference point for the potential is maintained. The CE passes all the current required to balance the current experienced at the WE. Furthermore, the material of CE is chosen such that the redox reaction at the electrode does not interfere with the electrochemical processes at the WE.

Point Electrode Setup

Point-contact electrode setup is a useful configuration to obtain detailed information about the reaction kinetics at the electrode-electrolyte interface. The simple geometry of point electrodes eliminates variables such as porosity and microstructure.

3 Literature

In this section, a review of the reported work relevant to this thesis is presented. Firstly, the background for discussing the positrode materials for PCECs is presented, followed by a review of the positrode materials regarding the backdrop of similar materials found in the literature. Lastly, a review of relevant reported work on electrode kinetics and reaction models are introduced, which will be further elaborated in the following sections from the experimental results from this work.

3.1 Proton Ceramic Electrochemical Cells

Compared to Proton Ceramic Electrochemical Cells (PCECs), Solid Oxide Fuel Cells (SOFCs) and Electrolysers (SOEs) are well studied. SOFCs exhibit high energy conversion efficiency, fuel flexibility and have a low environmental impact [7, 19]. The electrolyte is typically a solid ceramic oxide-ion conductor, such as yttria-stabilised ZrO_2 (YSZ). Oxygen gas reduces to oxide-ions at the cathode and migrates through the electrolyte to the anode, where they react with oxidised hydrogen to form water [6, 20].

The oxygen reduction reaction (ORR) at the SOFC cathode:

$$\mathrm{O_2(g) + 4e^- \rightarrow 2O^{2-}} \tag{3.1}$$

The hydrogen oxidation reaction (HOR) at the SOFC anode:

$$\mathrm{H_2(g) + O^{2-} \rightarrow H_2O + 2e^-} \tag{3.2}$$

Similarly, in PCFCs, the anode oxidises hydrogen gas to protons, which are conducted to the cathode by the electrolyte. The cathode reduces oxygen gas to oxide-ions, which reacts with the protons to form water at the electrode/electrolyte interface with access to gas, electrons and protons.

The reaction taking place at the negatrode of PCEC:

$$\mathrm{H_2(g) \rightleftarrows 2H^+ + 2e^-} \tag{3.3}$$

The reaction taking place at the positrode of PCEC:

$$O_2(g) + 4H^+ + 4e^- \rightleftarrows 2H_2O(g) \tag{3.4}$$

In contrast to SOECs, water is formed and split at the positrode of PCECs and thus prevents the dilution of the fuel, which facilitates higher fuel utilisation [10, 21].

High operating temperatures (600 - 1000°C) are required to achieve sufficient ionic conductivity and fuel utilisation, for SOECs. Although high operating temperature provides excellent electrical efficiency, there are several challenges such as thermal stressing, slow start-up and limited compatible materials in addition to the high costs [19, 20, 22, 23].

Altogether, electrode reactions and ionic transport in solid electrolytes are thermally activated processes. Reducing the operating temperature will, therefore, cause a decrease in the ionic conductivity of the electrolyte and an increase in the polarisation losses at the electrode [24]. Hence, proton conducting oxides are a suitable alternative to oxide-ion conducting electrolytes at intermediate temperatures due to their low activation energy for proton transport [25, 26].

3.1.1 Proton Ceramic Electrolytes

Proton conduction at high temperature in $SrCeO_3$-based oxides was first reported by Iwahara et al. in the early 1980s [27]. Ever since, proton conducting perovskite-type oxides, $ABO_{3-\delta}$, based on $BaCeO_3$, $SrZrO_3$ and $BaZrO_3$ have been extensively studied for materials for electrochemical applications such as fuel cells, electrolysers and electrochemical reactors. Among numerous of studied perovskite-type oxides [26-29], $BaZrO_3$-based materials are considered as benchmarked materials due to their almost pure protonic conductivity, above 10^{-2} Scm^{-1}. Moreover, they exhibit mixed ionic (H^+/O^{2-}) conductivity at higher temperatures and in a hydrogen-containing atmosphere [9, 30].

Transport of protons in oxides is, in no small extent, facilitated by the presence of oxygen vacancies in the lattice structure. Modification of the structure to induce vacancy formation can be achieved through substitutional acceptor doping, i.e. introduce foreign aliovalent metal oxide. Iwahara et al. [31] studied the effect of the dopant on the B-site in acceptor-doped perovskite-type oxide $BaCe_{1-x}M_xO_{3-\delta}$ where the dopant, M, were a trivalent cation. The study revealed that the transference number for protons decreased with increasing ionic radius of de dopant M^{3+} because the lattice structure became asymmetric. Contrary, the transference number of oxide ion increased with reduced symmetry as oxide ions migrate easier through orthorhombic crystal rather than cubic [31]. The basicity of the oxide induces the formation of protonic charge carriers. In addition to the chemical or thermodynamic stability of the oxides, structural stability is also necessary to consider. The ionic radius of cations occupying the A- and B-sites of the perovskite along with their electronegativity influences the structural stability and the protonic conductivity. Among the tested dopants, $BaCe_{1-x}M_xO_{3-\delta}$ doped with Yttrium appeared to perform almost as a pure proton conductor below 600°C.

Furthermore, in a study by Norby & Larring, protonic conductivities of various oxides were calculated from available data on proton concentrations and mobilities [25]. Figure 3.1 presents the summarised data over a broad range of temperature composed by Kreuer [9]. Although $BaCeO_3$-based oxides exhibit highest protonic conductivity, they are chemically unstable in atmospheres containing acidic and amphoteric gases such as CO_2 and H_2O, which reacts with the basic oxides to form carbonates and alkaline earth hydroxides [26].

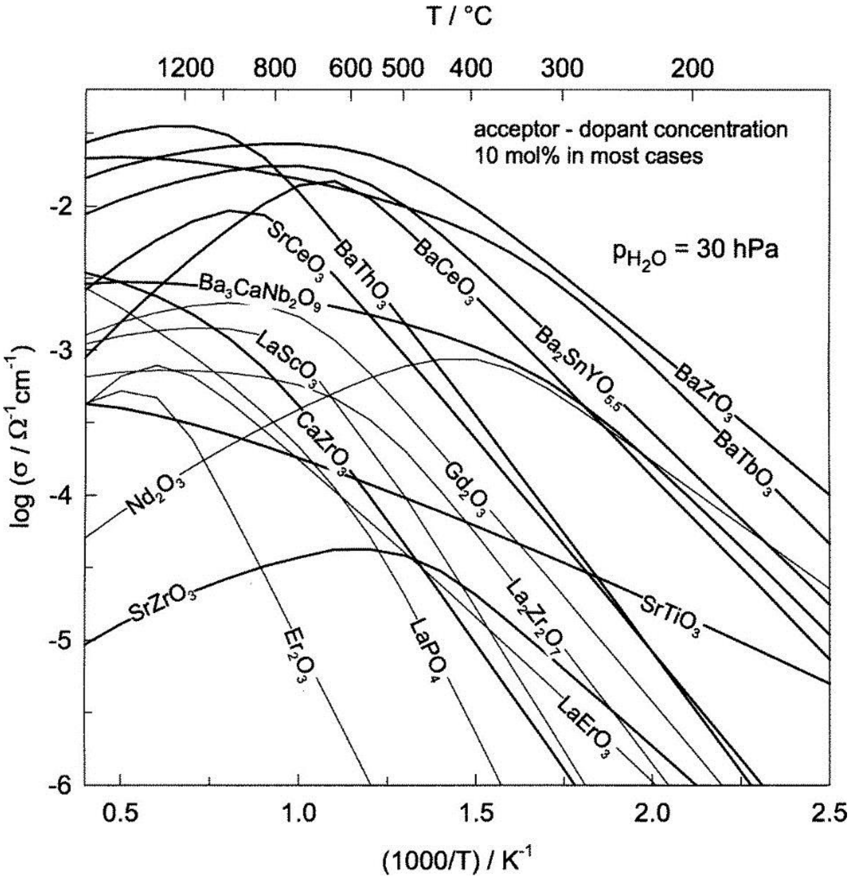

Figure 3.1 Partial proton conductivities as a function of the temperature of various proton conducting oxides [9]. The conductivities were calculated from data on proton concentrations and mobilities and parameters from hydration thermodynamics, according to Norby and Larring [25]. The bold lines represent the perovskite-type structure of the oxide.

Based on these calculations, yttrium-doped $BaZrO_3$ (BZY) was identified as the most promising candidate for commercial applications. However, BZY-electrolytes have shown high poor protonic conductivity in bulk due to the high grain boundary resistance and reduced sinterability [9, 25]. Yttrium-doped $BaCeO_3$ (BCY), on the other hand, exhibits high protonic conductivity and the grain boundary resistance is thus lower but suffers from poor chemical stability in carbon-containing atmospheres [32]. In 2000, Iwahara's group [33] reported that by partial substitution of Zr for Ce in BCY the chemical stability of $BaZr_xCe_{1-x}Y_{0.1}O_{3-\delta}$ (BZCY) was improved along with mixed conductivity at high temperature. However, the protonic conductivity decreased with increased content of Zr [33]. Owing to its improved chemical stability and increased protonic conductivity, BZCY has attracted much interest ever since for PCECs and membrane applications [34-36].

3.2 Positrode Materials for PCECs

Numerous factors need to be considered in the choice of electrode materials for PCEC as the electrochemical performance relies on the characteristics of all the components, from the anode to cathode. Although the half-cell reaction mainly takes place at the interface between the gas phase, electrode and electrolyte, the process already starts at the electrode surface. Whereas the cathode reaction for SOFCs comprises oxygen gas and oxide ions, PCFCs involves protons and water vapour as well. Furthermore, the positrode reaction mechanism is, to a large extent, based on the SOFC cathode reaction mechanism. The performance of PCEC is thus limited by electrode kinetics. Therefore, the requirements for electrode materials for PCECs are different from that for SOECs [19, 37].

Although the development of good proton ceramic electrolytes has matured, the performance of positrode materials for PCECs still needs to be improved for industrial applications. Without considering the specific reactions occurring at the interface of proton conducting electrolytes, cathode materials for SOFCs have been applied in PCFCs at reduced temperatures, which results in larger overpotentials and polarisation resistances [38].

The electrodes are stacked together with electrolyte and interconnect materials; it is therefore required that they are compatible. The structural and chemical stability should be maintained in a broad range of temperatures and atmospheres. The stability under various operating conditions becomes even more critical for materials with the potential to work as an electrode in both oxidising and reducing atmospheres, i.e. symmetrical cells. For promising positrode materials, as mentioned, it is crucial to consider the physical and chemical properties such as type of charge carriers and their conductivities, catalytic activity and microstructure. The desired electronic conductivity is of 100 Scm^{-1} but should not be lower than 1 Scm^{-1} [39]. Moreover, the positrode materials should also exhibit a sufficient proton conductivity to utilise a larger area of the electrode surface [24, 40]. Recent studies on materials with a perovskite-type structure for PCFCs cathode are getting much attention due to their mixed ionic and electronic conductivities [12, 41-43].

Electrode materials of Pt have been used broadly in the earlier studies of proton conducting electrolytes due to their high catalytic activity. However, Pt is not preferred for practical applications, besides the high costs, it is reported that the area specific resistance (ASR) increases with increasing content of Zr in electrolyte compositions, such as $BaZrO_3$ [35].

In the late 90s, Tao et al. [40] first proposed the idea that suitable cathode materials for PCFCs should exhibit both high ionic and electronic conductivity, i.e. mixed O^{2-}/e^- conductivity (O-MIEC) or mixed protonic and electronic conductivity, i.e. H^+/e^- (MPEC). Moreover, Tao et al. suggested that the cathode reaction given in Equation 3.4 can be divided into the following steps:

$$\frac{1}{2}\mathrm{O}_2(\mathrm{g}) + 2\mathrm{e}^- \rightarrow \mathrm{O}^{2-} \tag{3.5}$$

$$2\mathrm{H}^+ + \mathrm{O}^{2-} \rightarrow \mathrm{H}_2\mathrm{O} \tag{3.6}$$

In principle, whereas reaction 3.5 takes place at the electrode surface, reaction 3.6 is restricted to occur at the triple-phase boundary (TPB) if the electrode is an O-MIEC. Cathode materials with mixed protonic and electronic conductivity would extend the reaction zone to the entire electrode surface [40]. Figure 3.2 illustrates the PCFC positrode reaction when taking place at an O-MIEC and an MPEC, interpreted by Dailly et al. [41].

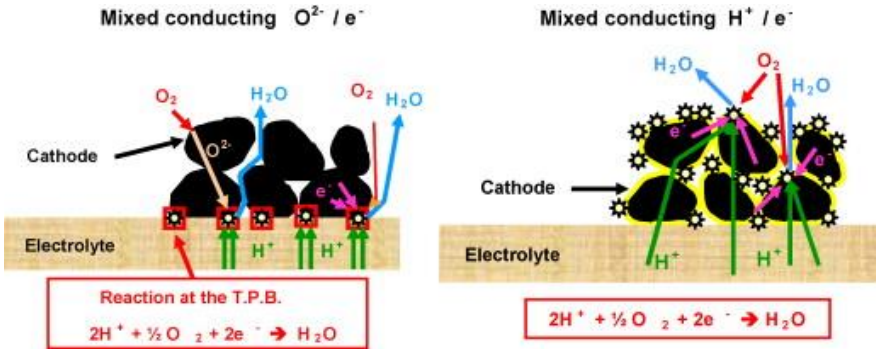

Figure 3.2 Schematics of the PCFC cathode reaction when the electrode material is an O-MIEC (left) and an MPEC (right) [41].

There has been a great interest in positrode materials with mixed ionic and electronic conductivities for PCECs; the idea has been discussed by several types of research ever since. Electrode materials with protonic conductivity show great potentials as promising positrode materials for PCECs. In fuel cell mode, the protons from the electrolyte can diffuse through the electrode bulk, which would lead to faster kinetics of the electrochemical processes due to the extended reaction active area from TPB to the whole electrode surface [41, 44, 45].

3.2.1 Mixed Ionic and Electronic Conductors

Perovskite oxides with the general formula $ABO_{3-\delta}$ have been used extensively as cathode material for SOFCs due to their mixed ionic and electronic conductivities. The structures flexibility makes it possible to modify the properties over a broad range by choice of the cations on the perovskites A- and B-site and additional doping. Commonly the A-sites are occupied by alkaline earth or rare earth metals while the B-site cations are redox-active transition metals. These B-site transition metals make the oxygen lattice flexible by changing their valence to compensate charge imbalance and contribute to the electronic conductivity and catalytic activity [46]. Furthermore, the oxygen non-stoichiometry, δ, accelerates oxygen transport through uptake and release of oxygen. Along with the multiple oxidation states of transition metals, facilitates potential proton uptake, which makes perovskites good candidates for PCFC cathode materials [41].

The properties of MIECs are modified by doping, the, i.e. substitution of transition metal (on the B-site) in perovskite oxides. Iron-based perovskite oxides such as $AFeO_{3-\delta}$ (A = alkaline or rare earth metals) and $A_2Fe_{1-x}M_xO_{6-\delta}$ (M = transition metals) have been studied extensively over the past decades [47-50]. Most of the MIEC perovskite electrode materials are based on $LaCoO_3$ or $LaMnO_3$, often with Sr and Fe substituted on the A- and B-site, respectively. One of the most studied electrode materials for high temperature systems is $La_{0.8}Sr_{0.2}MnO_3$ (LSM). LSM-based cathodes have been commercialised for SOFCs at > 800 °C due to their high thermal and chemical stability, electrical conductivity and catalytic activity [51]. However, as the ionic conductivity is negligibly low, ~ 10^{-8} Scm^{-1} [52], LSM is thus considered as a pure *p*-type conductor. Moreover, the slow oxygen surface kinetics results are high cathodic overpotential for both PCFCs and SOFCs. [53].

Cobalt oxides exhibit catalytic activity towards the oxygen reduction reaction thus Co-containing perovskite-type MIECs, such as $Sm_{0.5}Sr_{0.5}CoO_{3-\delta}$ (SSC) [54], $Ba_{0.5}Sr_{0.5}Co_{0.8}Fe_{0.2}O_{3-\delta}$ (BSCF) and $La_{0.6}Sr_{0.4}Co_{0.2}Fe_{0.8}O_{3-\delta}$ (LSCF) [55, 56] have shown high efficiency as cathode materials for SOFCs. However, these have shown either poor chemical stability under operating conditions or too high polarisation resistances and overpotentials at intermediate temperatures as PCFC cathodes [56].

With the ionic and electronic conductivities of the order of 10^{-1} and 10^{2} Scm^{-1}, respectively, $SrFeO_{3-\delta}$ ($0 < \delta < 0.5$) is considered as the best MIEC among strontium ferrite based materials [57]. In oxidising atmospheres, $SrFeO_{3-\delta}$ acts as a *p*-type conductor and turn out to be an *n*-type conductor under reducing conditions. In a study of the effect of substituting the B-site cation with higher valent transition metals, Fernández-Ropero et al. [16] reported the highest conductivity of the compound $SrFe_{0.75}Mo_{0.25}O_{3-\delta}$ (SFM) under reducing conditions (5 Scm^{-1} at 800 °C). Substituting Mo-ions into the Fe-site of $SrFeO_{3-\delta}$ gives mixed oxidation states on the B-site, and thus the rich redox chemistry of molybdenum facilitates the formation of electronic charge carriers and also introduce oxygen vacancies into the lattice due to large oxygen non-stichometry. Furthermore, the high chemical stability makes SFM suitable as both cathode and anode materials in symmetrical SOFCs [16].

3.2.2 Mixed Protonic and Electronic Conductors

The protonic conductivity of perovskite oxides can be increased by water uptake, i.e. hydration ($ABO_{3-\delta}(OH)_x$). The presence of oxygen vacancies allows for insertion of protons ($OH^{\bullet}$) in vacant sites in the structure [40, 41]. High concentration and mobility of oxygen vacancies are necessary to enhance hydration, i.e. proton uptake, or induce the formation of protonic defects within the crystal structure. Instead of occupying lattice sites, protons prefer to jump between the oxide ions due to their small size. The hydration reaction of perovskite oxides in a water-rich atmosphere can be written as follow:

$$H_2O(g) + v_O^{\bullet\bullet} + O_O^{\times} \rightleftarrows 2OH_O^{\bullet} \tag{3.7}$$

Furthermore, the basicity of the oxide is significant as well. In a comprehensive study of trends in proton uptake for MIEC perovskites by Thermogravimetric Analysis (TGA), Zohourian et al. [58] found that the basicity of the oxide ions determines the uptake of protons for the most part. The proton concentration increased with increasing substitution of Ba on the A-sites in $Ba_xLa_{1-x}FeO_{3-\delta}$ (BL_xF) perovskites. As a result of the lower electronegativity of Ba^{2+} compared to La^{3+}, the basicity of the oxide ions increases, as well as the concentration of oxygen vacancies. When exposed to water vapour, the oxygen vacancies may hydrate according to Equation 3.7. Figure 3.3 presents the trends of proton uptake in the various mixed conducting oxides investigated by Zohourian et al. [58]. Although increased substitution of Ba on the A-site enhance the proton uptake, a small amount of La is still necessary to stabilise the cubic perovskite phase caused by size mismatch of the cations located at A- and B-sites. Furthermore, the basic character of the oxide impacts the stability of protonic defects, which are among the essential factors to consider for optimisation of PCEC positrode material [59-61].

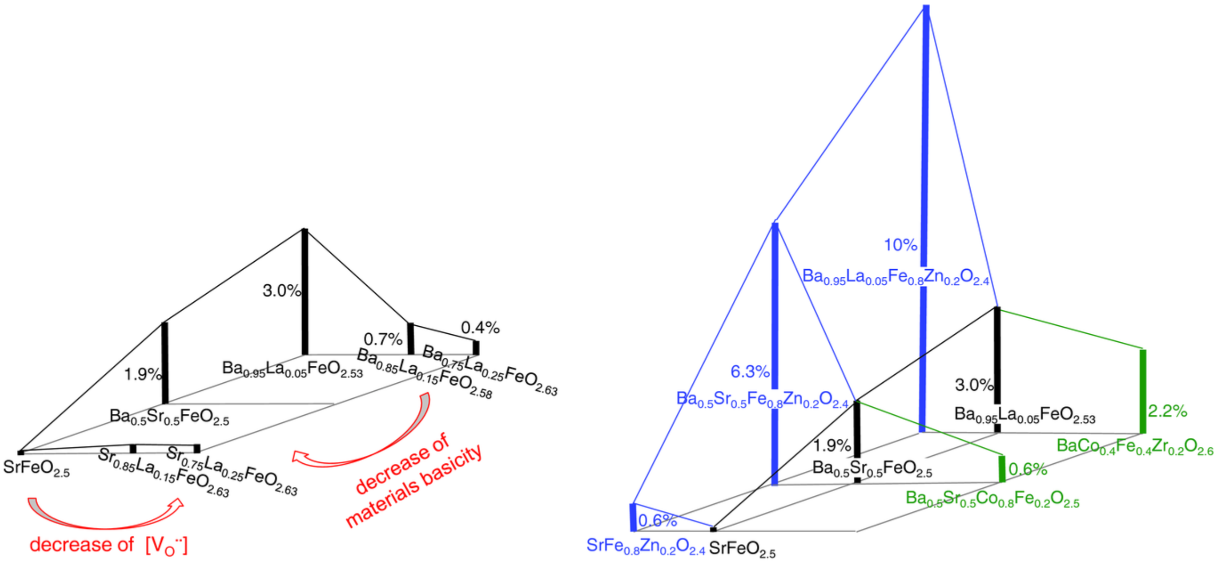

(a) (b)

Figure 3.3 Proton concentration in mol% (z-axis) based on the concentration of oxygen vacancies and the basicity of various perovskites at 250 °C and 16mbar H_2O. (a) Different content of La and Sr on the A-site. (b) Influence of substitution of Zn and Co on the B-site. All materials are in the hydration regime [58].

Dailly et al. studied various MIEC oxides, perovskites $AMO_{3-\delta}$ (A = La, Ba, Sr; M = Mn, Fe) and layered Ruddlesden-Popper $A_2MO_{4+\delta}$ (A = La, Nd, Pr, Sr; M = Ni), as cathode materials for PCFCs under water-rich atmosphere. Whereas the layered Ruddlesden-Popper structure exhibit electrocatalytic activity for oxygen reduction, the perovskites are suitable for proton uptake due to oxygen deficiency. Although the TGA data designated on a small amount of water uptake for all the perovskites, the increase in protonic conductivity could not be proved experimentally; the change in protonic conductivity was not significant due to the low hydration of the oxides. However, BSCF perovskite and $Pr_2NiO_{4+\delta}$ (PN) showed to be promising cathode materials for PCFCs as the ASRs for both was measured close to 1 Ωcm^2 at 600 °C, lowest of the studied materials [41]. Hydration properties of these two materials along with LSCF and the double perovskite $PrBaCo_2O_{5+\delta}$ (PBC) have been studied by Grimaud et al. [56]. For Ba- and Sr-containing oxides PBC and BSCF, larger oxygen deficiency gave higher water uptake due to the basicity of the compounds. Whereas PN showed a small amount of water uptake, no hydration was observed for LSCF. Based on the observed mixed conductivity BSCF, PBC and PN are also referred to as triple-conducting ($e^-/O^{2-}/H^+$) oxides (TCOs). Batocchi et al. further studied the electrical and electrochemical properties of BSCF and PN along with the compatibility as cathode materials for PCFCs with proton conducting $BaCe_{0.9}Y_{0.1}O_{3-\delta}$ (BCY10) electrolyte. Whereas the perovskite BSCF was stable with BCY10 electrolyte small amount of secondary phases was observed for the Ruddlesden-Popper PN. Furthermore, above 500 °C PN single phase electrode shows lower polarisation resistance than BCFC electrode [43].

Basic Co-based perovskites such as $ACoO_{3-\delta}$ (A = Ba, Sr, La) have shown high stability upon water uptake, the effective cobalt valence state and oxygen non-stoichiometry (δ) gives rise to high ionic and electronic conductivity [59]. Rare earth (RE) double layered perovskite oxides with the general formula $BaRECo_2O_{6-\delta}$ exhibit high affinity to water, i.e. high oxide basicity. The layered double perovskites possess an ordered structure with alternating Ba and RE-layers on the A^I and A^{II} -sites (along the *c*-axis of the crystal) and oxygen vacancies localised within the RE-layers. The oxygen vacancies, also present in the Co-plane (along the *b*-axis), facilitate the diffusion of oxygen species [62]. Materials with this structure, such as $GdBaCo_2O_{5+\delta}$ (GBC) and $GdBaCoFeO_{5+\delta}$ (GBCF), have shown great potential for electrode and membrane applications at high and intermediate temperatures [61, 63-65].

$BaGd_{0.8}La_{0.2}Co_2O_{6-\delta}$ (BGLC)

The double perovskite oxide $BaGd_{0.8}La_{0.2}Co_2O_{6-\delta}$ (BGLC1082) was first proposed as a mixed protonic/electronic conductor (MPEC) by Strandbakke et al. in 2015 [12]. Together with the double perovskite cobaltites $BaGdCo_{1.8}Fe_{0.2}O_{6-\delta}$ (BGCF), $BaPrCo_2O_{6-\delta}$ (BPC) and $BaPrCo_{1.4}Fe_{0.6}O_{6-\delta}$ (BPCF), BGLC was investigated as positrode for PCECs on proton conducting BZCY72 electrolyte. The series of materials with the general formula $BaRE_{1-x}La_xCo_{2-y}Fe_yO_{6-\delta}$ (RE = Pr or Gd) exhibit the same crystal structure as rare earth double layered perovskites described above. Figure 3.5 illustrates the structure of the layered double perovskite BGLC, where some La is substituted for Gd on the A-site.

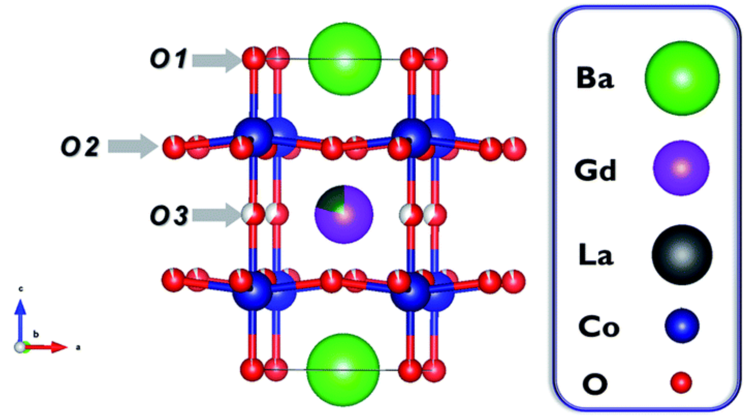

Figure 3.4 The layered structure of the double perovskite BGLC proposed by Vøllestad et al. [14]. O1 and O3 represent A^{I} and A^{II} -layers, respectively, O2 represents the B-layer containing oxygen vacancies.

Although the Gd-containing oxides exposed larger oxygen deficiencies (δ) than Pr-containing oxides, BGLC was the only material that showed hydration at 400°C. Among the four double perovskites, BGLC also had the lowest oxygen content (6-δ) at 400°C. A slight increase in weight for BGCF, BPC and BPCF were observed by TGA when changing the atmosphere from dry to wet, however, the change was not significant compared to BGLC, which had a weight gain corresponding to a proton concentration of 3 mol % [12].

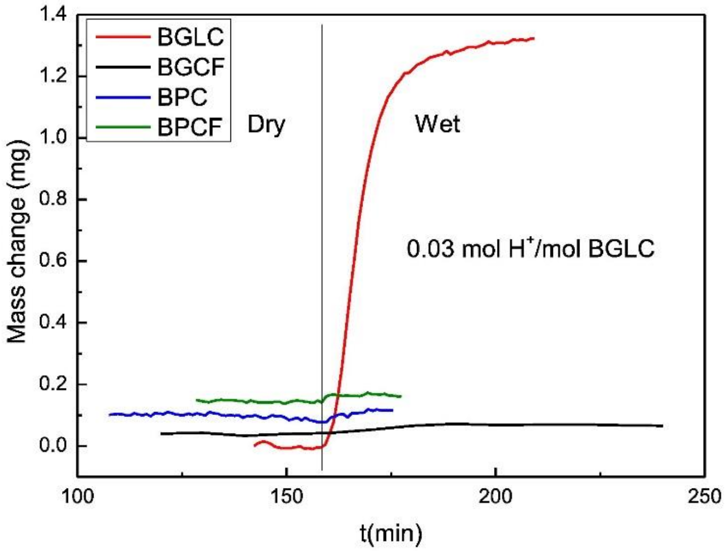

Figure 3.5 Mass change of the tested double perovskite oxides, $BaRE_{1-x}La_xCo_{2-y}Fe_yO_{6-\delta}$, after an isothermal switch of pH_2O from $3\cdot10^{-5}$ to 0.02 atm (grey line) at 400°C $4\cdot10^{-4}$ atm pO_2 by Strandbakke et al. [12]. Among the tested oxides, only BGLC showed significant water uptake when exposed to water vapour at 400°C.

Electrochemical measurements the using proton conducting BZCY electrolyte showed that in wet oxygen BGLC exhibited the lowest polarisation resistance of the four electrode materials, which was as low as 0.046 Ωcm^2 at 700 °C and 10 Ωcm^2 at 350 °C. The activation energies at high temperature region were higher than that at lower temperatures (1.3 and 0.5 eV respectively) [12].

BGLC is so far the positrode material with the lowest reported apparent polarisation resistance of 0.05 Ωcm^2 at 650 °C under water-rich atmosphere on BZCY electrolyte. Furthermore, BGLC exhibit an activation energy around 0.5 eV at the lower temperatures and an electronic conductivity > 800 Scm^{-1} [12, 14, 15].

3.3 Positrode Kinetics

The most critical challenge for both SOFCs and PCFCs has been the slow reaction kinetics at the cathode surface. In order to optimise the functional properties of positrode applications, a better understanding of the electrode processes is necessary. That includes a detailed study of the reaction mechanism in addition to reaction kinetics together with elementary steps, the contributing charge carriers and reaction intermediates. Theoretically, this may be identified by determining the “bottleneck,” i.e. rate-liming steps. Such analysis of the reaction processes and characterisation of the rate-determining step are often carried out through investigation of the polarisation resistances as a function of oxygen and water vapour partial pressures. It follows that the details in the mechanisms are dependent on the characteristics of the electrode material [66]. The reaction models for electrode reactions found in literature, at present, are based on the reaction mechanism for SOFC electrodes, which are examined well, unlike for PCEC electrodes. However, the positrode reaction involves three chemical species instead of two, making the kinetics more complex [54, 67].

3.3.1 Reaction Mechanism

The electrode redox reaction is a multistep process involving various species. The reaction rate of each elementary step is affected by the physical properties of the electrode material along with chemical factors as the concentrations, mobilities and interactions between the involved species [68]. Typical steps of the cathode reaction for both SOFCs and PCFCs are adsorption, diffusion and reduction of oxygen at the surface. Further, SOFC cathodes transfer the reduced oxygen ions into the electrolyte, an oxide ion conductor. Unique characteristics for PCFC electrode reaction, due to the proton conducting electrolyte, is the transfer and reaction of protons followed by formation and desorption of H_2O either at the surface of a mixed conducting oxide or close to the triple phase boundary (TPB) [22, 40, 41, 43, 45, 54, 69, 70].

Properties of the electrode material impact the reaction path, which also influences the transport or reaction kinetics. Electrode materials with high Ba-contents are expected to activate the bulk path for proton transport instead of TPB or surface path because of the sufficient protonic conductivity [58]. Furthermore, the positrode reaction may occur through different reaction paths simultaneously, each with a corresponding rate-determining step (RDS); however, the overall reaction rate will be dominated by the reaction path with fastest RDS.

Figure 3.6 illustrates possible reaction pathways for the PCFC cathode reaction on MPECs suggested by Poetzsch, Merkle and Maier [45].

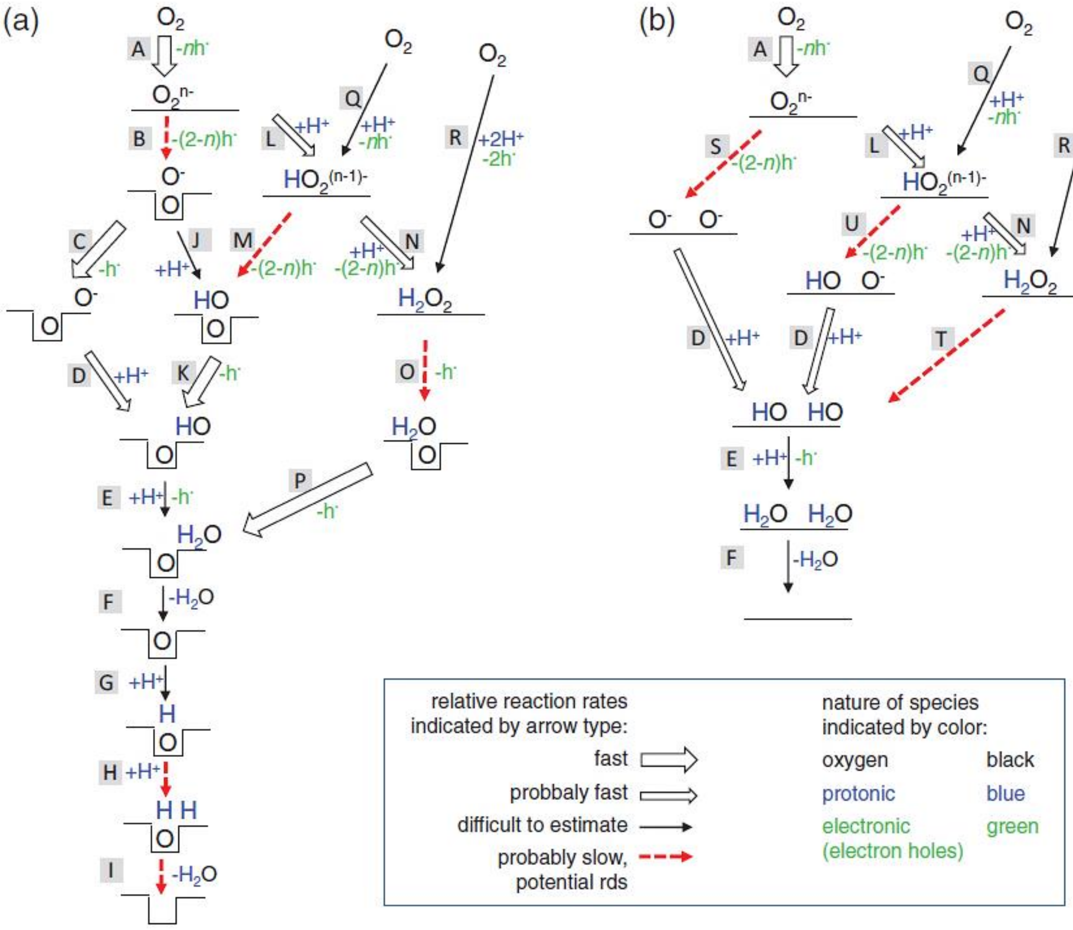
(a)
O2
A -nh·
O2n-
B -(2-n)h·
O-
O
C -h·
J +H+
M -(2-n)h·
Q +H+ -nh·
L +H+
HO2(n-1)-
N +H+ -(2-n)h·
R +2H+ -2h·
H2O2
O -h·
H2O
HO
D +H+
K -h·
P -h·
E +H+ -h·
F -H2O
G +H+
H
H +H+
H H
I -H2O
(b)
S -(2-n)h·
O- O-
U -(2-n)h·
HO O-
T
D +H+
HO HO
E +H+ -h·
H2O H2O
F -H2O
relative reaction rates indicated by arrow type:
fast
probbaly fast
difficult to estimate
probably slow, potential rds
nature of species indicated by color:
oxygen black
protonic blue
electronic (electron holes) green

Figure 3.6 Suggested reaction pathways for oxygen reduction on MPECs positrode materials [45]. Path (a) is through oxygen dissociation with $v_O^{\bullet\bullet}$ assistance and path (b) is through oxygen dissociation without $v_O^{\bullet\bullet}$ assistance.

3.3.2 Elementary Reactions and Rate-Determining Step

The rate of each elementary reaction is, as mentioned above, dependent on several factors such as active surface sites, transport pathways, involved species in a particular step, their mobilities and concentrations. At least one of these elementary steps limits the overall reaction rate and is hence referred to as the rate-determining step (RDS).

The polarisation resistance, R_p, is proportional to the partial pressure of oxygen (pO_2) and water vapour (pH_2O) through:

$$\frac{1}{R_p} \propto pO_2^m \, pH_2O^n \tag{3.8}$$

The reaction orders m and n relating to pO_2 and pH_2O, respectively, are commonly used to assign the polarisation resistance to one or more of the suggested reaction steps and depends on the type of species involved in the rate-limiting steps. Thereby, it is essential to keep in mind that these reaction orders are theoretical and only valid in dilute conditions, i.e. low surface coverages.

Uchida et al. first proposed the PCFC cathode reaction divided into a series of elementary steps in the 1980s [71]. The oxygen partial pressure dependence of the polarisation resistance of platinum electrode on $SrCe_{0.95}Yb_{0.05}O_{3-\delta}$, a proton conducting electrolyte, was investigated. The series of elementary reactions steps represented as a five-step process with the following reaction orders[4], m, are shown in Table 3.1.

Table 3.1 The first model of elementary reaction steps at the PCFC cathode and the corresponding reaction orders, *m*, associated with oxygen partial pressure presented by Uchida et al. [71]

Step	Elementary reaction	m in $R_p \propto pO_2^{-m}$
1	$O_2\,(g) \rightarrow O_2\,(ad)$	1
2	$O_2\,(ad) \rightarrow 2O(ad)$	1 - 0
3	Surface diffusion of O(ad)	½ - 0
4	$O(ad) + 2H^+ + 2e^- \rightarrow H_2O(ad)$	½ - 0
5	$H_2O(ad) \rightarrow H_2O(g)$	0
Overall: $\frac{1}{2}\,O_2(g) + 2H^+ + 2e^- \rightarrow H_2O(g)$		

They observed that polarisation resistance decreases with increasing oxygen partial pressure with a reaction order of ¼ and suggested that the rate-determining step for the cathode reaction was the surface diffusion of the adsorbed oxygen species of the platinum surface to TPB. It was emphasised that this was in contrast to observations made for SOFC cathode reactions; though reasoned the presence of water was sufficient reason to alter the dependencies. Afterwards, the reaction series has been elaborated. The variety of alternative mechanisms makes it challenging for identifying the reaction pathway and the rate-determining step. He et al. [2] suggested a reaction series subdivided into eight elementary steps based on characteristics of the transfer and reaction of protons. The proposed elementary steps and the corresponding reaction orders relating to oxygen and water vapour partial pressure and are presented in Table 3.2.

---

[4] In the article the reaction order is denoted *n*, to avoid any confusion the same notation as in Equation 3.8 is used.

Table 3.2 Series of elementary reactions steps proposed by He et al. for the PCFC cathode and their corresponding reaction orders $R_p \propto pO_2^{-m}\, pH_2O^{-n}$, for oxygen and water vapour partial pressure, respectively [2].

Step	Elementary reaction	*m*	*n*
1	$O_2(g) \rightarrow 2O_{ad}$	1	0
2	$O_{ad} + e^- \rightarrow O_{ad}^-$	⅜	0
3	$O_{ad}^- \rightarrow O_{TPB}^-$	¼	0
4	$O_{TPB}^- + e^- \rightarrow O_{TPB}^{2-}$	0	0
5	$H_{electrolyte}^+ \rightarrow H_{TPB}^+$	0	½
6	$H_{TPB}^+ + O_{TPB}^{2-} \rightarrow OH_{TPB}^-$	0	½
7	$H_{TPB}^+ + OH_{TPB}^- \rightarrow H_2O_{TPB}$	0	1
8	$H_2O_{TPB} \rightarrow H_2O(g)$	0	1

Whereas steps 5-8 are unique characteristics of the PCFC cathode reaction, the first four steps in Table 3.2 are similar to those for SOFC cathode reaction and describes dissociative adsorption and diffusion of oxygen together with electron transfer [72]. Step 3 describes the transport of adsorbed O^- at the electrode surface to the TPB without further elaboration of the transport mechanism. The oxygen species can diffuse neutral, singly- or doubly charged dependent on the properties of the cathode material. If the cathode is an O-MIEC, O^{2-} species might take the transport path through the electrode bulk [73]. The presence of ambient water also contributes to the oxide-ions to diffuse as hydroxyls or hydroxide ions.

As mentioned above, although the electron transfer processes are expected to occur fast; the charge transfer can be rate-limiting. In a comparison study between single phase and architectured electrodes for PCFCs, Batocchi et al. [43] observed a pH_2O dependence of - ½ for the charge transfer resistance for single phase electrodes that exhibit proton conductivity such as and PN. Batocchi et al. suggested the charge transfer reaction, i.e. proton transfer across the electrolyte/electrode interface to be the rate-determining step. Furthermore, the polarisation resistance for the architectured PN electrode exhibited a pH_2O dependency of -1. Hence, the RDS was suggested to be the formation or desorption of water [43]. A negative water vapour dependency for MPECs has been observed in a few studies [43, 45, 56]. These are relatively new findings, and it is, therefore, a deficiency of thorough interpretation as well as investigation.

4 Experimental

In this chapter, the experimental methods and equipment used for this work are described.

4.1 Sample Preparation

4.1.1 Positrode Materials

The perovskite $SrFe_{0.75}Mo_{0.25}O_{3-\delta}$ (SFM25) was synthesised by a solid-state reaction between the precursors listed in table 4.1. Stoichiometric quantities of each precursor powder were weighted and mixed.

Table 4.1 Starting materials used to synthesise SFM25

Precursor	Purity	Supplier
$SrCO_3$	≥ 99.9 %	Sigma-Aldrich
Fe_2O_3	99.5 %	Alfa Aesar
MoO_3	99.5 %	Alfa Aesar

All three precursors were mixed and crushed in an agate mortar. The powder was transferred to an agate vial with agate balls over for wet-grounding. Isopropanol was poured over before the vial was sealed and placed in a planetary ball mill at room temperature with 200 rpm for 3 hours. The slurry was poured into a beaker and placed in a heating cabinet at 110 °C to dry for about 24 hours. The dried powder was calcined in an alumina crucible at 800 °C for 12 hours with a heating/cooling ramp rate of 200 °C/h.

The sintered powder was pressed to pellets with a diameter of 10 mm and thickness of 1-2 mm (~ 0.5 g) by uniaxial cold-pressing at approximate 1 ton in a hydraulic Specac GS15011 press. The pellets were sintered at 1200 °C for 30 hours with a heating/cooling ramp rate of 200 °C/h.

Single phase powder of $BaGd_{0.8}La_{0.2}Co_2O_{6-\delta}$ (BGLC10-8-2) by Marion Technology® company was pressed to pellets using the same procedure as for SFM. The pellets were sintered at 1180 °C for 5 hours with a heating/cooling ramp rate of 180 °C/h.

The sintered pellets were weighed and measured before characterisation by SEM and XRD.

4.1.2 Proton Conducting Electrolyte

CoorsTek manufactured proton conducting ceramic electrolyte pellet with the composition BZCY72. The diameter and thickness were 19.27 mm and 1.20 mm, respectively. Three layers of Pt ink M-001511 by METALOR® was painted on each side of the electrolyte pellet, representing the reference (ring along the edge) and the counter electrode (circle in the middle) as shown in Figure 4.1.

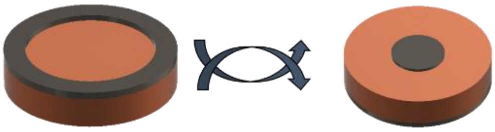

Figure 4.1 Schematics of the button electrolyte pellet (BZCY) with a platinum reference electrode (left) and counter electrode (right) painted on the electrolyte surface.

After each layer of paint, the electrolyte pellet was dried in a heating cabinet at 120 °C for 10 to 15 min before it was fired at 1100 °C for 1 hour with a heating/cooling ramp rate of 180 °C/h. Temperature profile for the various processes during sample preparation is presented in Figure 4.2.

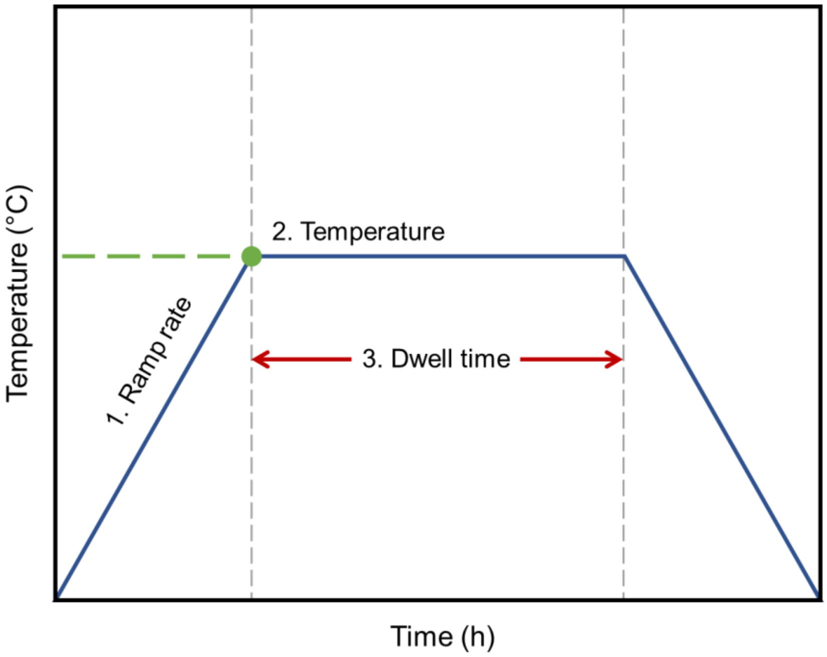

Figure 4.2 Temperature profile throughout the sample preparation, details of the various processes are given in Table 4.2.

Table 4.2 Specifics of the processes applied during sample preparation, the temperature profile is illustrated in Figure 4.2.

	1	2	3
Calcination of SFM	200 °C/h	800 °C	12 h
Sintering of SFM	200 °C/h	1200 °C	30 h
Sintering of BGLC	180 °C/h	1180 °C	5 h
Firing of BZCY	180 °C/h	1100 °C	1 h

4.2 Sample Characterisation

4.2.1 Scanning Electron Microscopy (SEM)

In order to study the microstructure, surface morphology and phase composition of the samples, an FEI-SEM with a field emission gun (FEI Quanta 200 FEG-ESEM) was used. The microscope has three detectors; an Everhart Thornley Detector (ETD) which detects the secondary electrons a Solid-State Detector (SSD) which detects the backscattered electrons and an Energy Dispersive X-ray Spectrometer (EDS) for detecting the different elements that are present in the sample. Whereas the ETD gives information about the topography, the SSD yields information about the phase composition of the sample. The instrument was operated under high-vacuum (10^{-5} Pa) mode with an acceleration voltage of 20 kV.

Elemental analysis was conducted using an EDAX Pegasus 2200 EDS (Energy Dispersive X-Ray Spectroscopy) detector, which is coupled to the FEI-SEM.

4.2.2 X-Ray Diffraction (XRD)

The phase composition and crystal structure of all samples were studied by XRD on a Bruker AXS D8 Discover with $CuK_{\alpha,1}$ ($\lambda = 1.54060$ Å) and $CuK_{\alpha,2}$ ($\lambda = 1.54439$ Å) radiation. The x-rays were scanned in the range $10° \leq 2\theta \leq 70°$ with a step size of 0.02 °/s. Longer time steps (8) were used for BGLC as Co gives rise to fluorescence.

Diffractograms were processed in DIFFRAC.EVA v4.3 by comparison to the Powder Diffraction File (PDF) database from the International Centre for Diffraction Data (ICDD). Structural refinements were achieved with TOPAS v5.0 by the Rietveld method.

4.3 Electrochemical Measurements

Potentiostatic EIS measurements were performed with a Gamry Reference 3000 instrument. Sweeps with an AC amplitude of 40 – 80 mV was conducted over a frequency range of 100 kHz to 1 mHz was applied for every 50 °C while decreasing the temperature from 750 to 350 °C for BGLC and 650 to 400 °C for SFM.

4.3.1 Instrumental Setup

Three-Electrode Setup

A point-contact three-electrode four-probe setup with a circular planar geometry (Figure) was used for the electrochemical measurement of the positrode reaction. The counter electrode (CE) is located on the opposite side of the WE. RE and CE of Pt paste were painted on the electrolyte as described above. The electrode pellet was placed vertically on the electrolyte to obtain point contact. Also, the area of CE is larger that WE to prevent limiting the overall current.

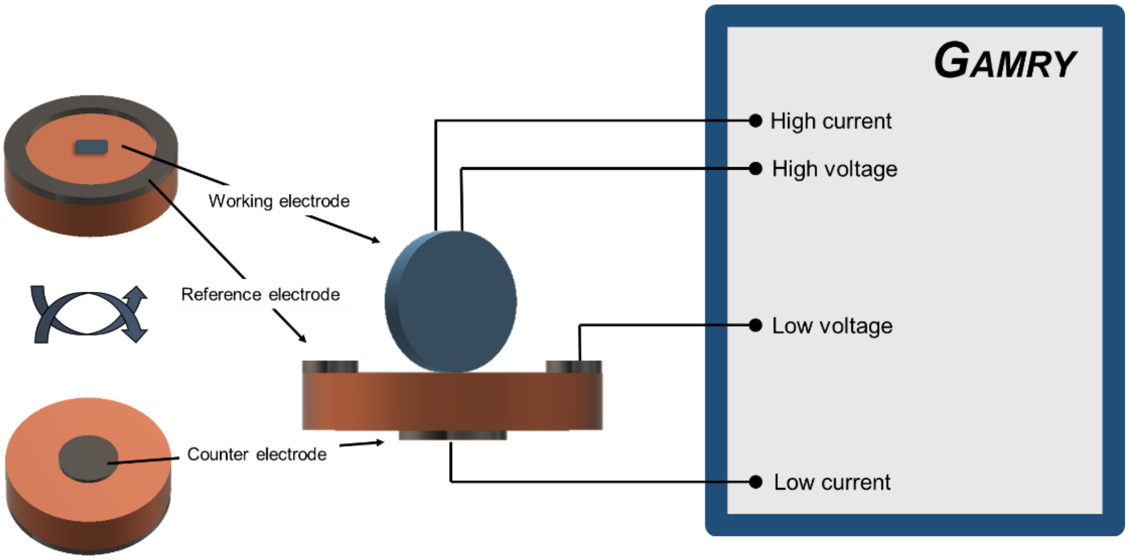

Figure 4.3 Schematics of the three-electrode four-probe setup with the working electrode placed vertically on the electrolyte making point contact. The applied potential is altered at the High current (HC) probe and measured at High voltage (HV) probe, both connected to the working electrode.

Footprint from the point electrode on the electrolyte surface shows the contact area, i.e. the active region of the positrode reaction.

Measurement Cell

Electrochemical measurements were carried out in a ProboStat™ measuring cell manufactured by NorECs AS. The ProboStat™ is supplied with electrode and thermocouple feedthroughs in addition to gas in- and outlets for inner and outer chambers, as shown in Figure 4.4.

The ProboStat™ was first heated up to 900 °C with a heating ramp rate of 3 °C/min in wet air (pH_2O = 0.025 atm and pO_2 = 0.20 atm) before the temperature was decreased to 700 °C for the electrochemical measurements.

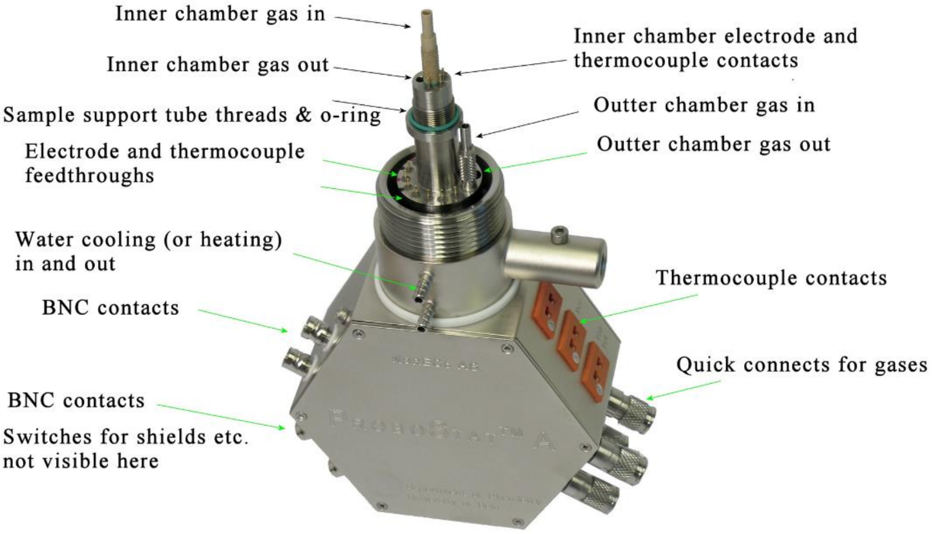
Inner chamber gas in
Inner chamber gas out
Inner chamber electrode and thermocouple contacts
Sample support tube threads & o-ring
Outter chamber gas in
Electrode and thermocouple feedthroughs
Outter chamber gas out
Water cooling (or heating) in and out
Thermocouple contacts
BNC contacts
Quick connects for gases
BNC contacts
Switches for shields etc. not visible here
ProboStat™ A

Figure 4.4 Illustration with a description of the main components of the ProboStat™ measurement cell by NorECs AS.

Gas Mixer

In order to obtain the desired atmosphere inside the measurement cell, the oxygen partial pressures were controlled by a mixture of O_2/Air + Ar of different ratios. Likewise, the water vapour partial pressure was controlled by passing the gas stream through a saturated solution of potassium bromide at room temperature, which provides a nominal pH_2O = 0.025 atm approximately. The various gas mixtures were obtained by an in-house built gas mixer containing a series of flow meters connected by Cu-tubing, as illustrated in Figure 4.5.

The setup allows for an initial gas (G1) to be diluted by a second gas (G2). G1 and G2 enter flow meter 1 and 2, respectively, and are mixed in flow meter 3 as mix 1 (M1). The flow of G1, G2 and M1-M4 is regulated by tuning a floater of either glass (gl) or tantalum (Ta) inside the flow meters. Excess gas of each mixture is sent through pressure regulators to ensure constant overpressure through the system, which consists of bubblers (B1-B4) connected to a ventilation system.

Followed by the three diluting stages, M3 is streamed through to either a drying stage or bypassed directly to the last flowmeter before entering the ProboStat™. Both are wetting stages where the gas is sent through KBr saturated H_2O bubbler. The gas also flows through a dehydrating agent of P_2O_5 in parallel with the drying stage.

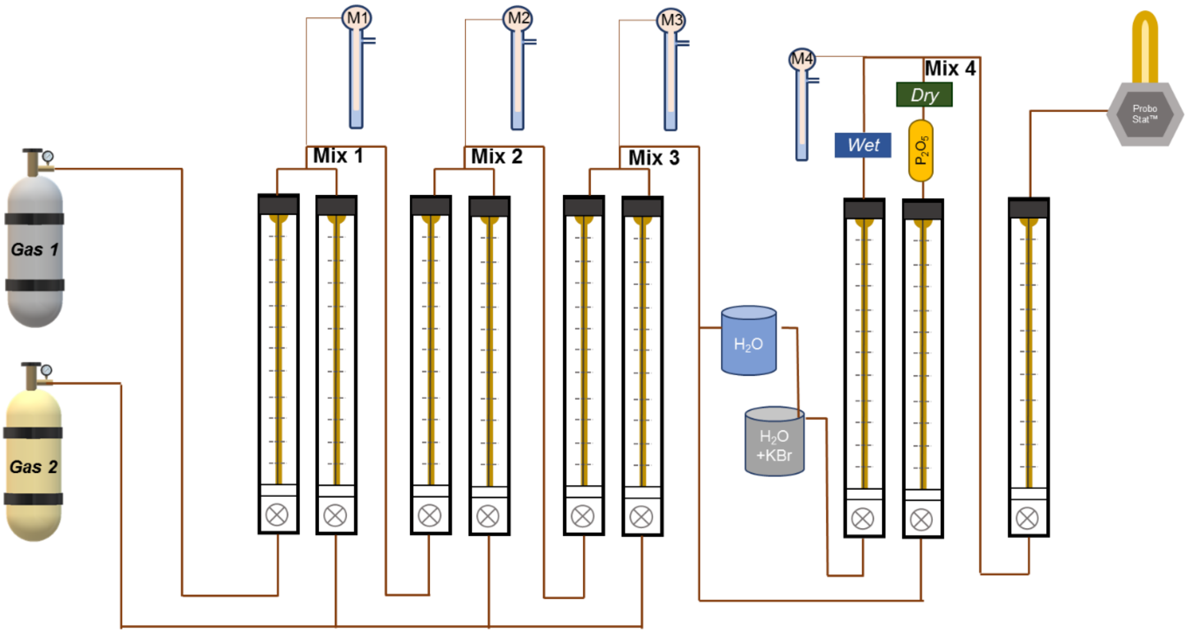

Figure 4.5 Schematics of the gas mixer and the measurement cell, ProboStat™.

The flow rates each input gases needed to obtain the desired gas compositions were determined through the software *ProGasMix* v0.7.1.

4.3.2 Measurement Series

Partial pressures of oxygen and water vapour were adjusted systematically; pO_2 at 1, 0.20, 0.05, 0.0020 and 0.0005 atm and pH_2O at 0.025, 0.01, 0.0065, 0.0035 and 0.0023 atm was measured at each temperature step. The temperature dependencies were carried out in air (pO_2 = 0.20 atm and pH_2O = 0.025 atm). For every change in either the temperature or the atmosphere of the cell, a single frequency test was conducted to ensure that the chemical equilibrium of the systems was obtained.

4.4 Data Analysis

4.4.1 Deconvolution

The impedance data were deconvoluted using the analysis software ZView® v3.5e by Scribner Associates, Inc. Three semi-circles; one in the high-frequency (HF) range and two arcs in the mid and low frequency (MF and LF) range was observed in the Nyquist diagram. Each was assigned to a particular contribution from the system. The semi-circle observed in the HF range corresponds to the electrolyte response while the MF and LF ranges correspond to the response from the electrode; charge transfer resistance and double layer capacitance in the MF range and mass transfer resistance and capacitance in LF range. Gerischer element was used due to the asymmetrical shape of the low-frequency arcs, and the contribution was attributed to the mass transfer process. Similarly, in the HF range, inductance was observed instead of capacitance in some cases.

The EIS spectra were fitted using an equivalent circuit model based on a Randles-type circuit, as shown in Figure 4.4.

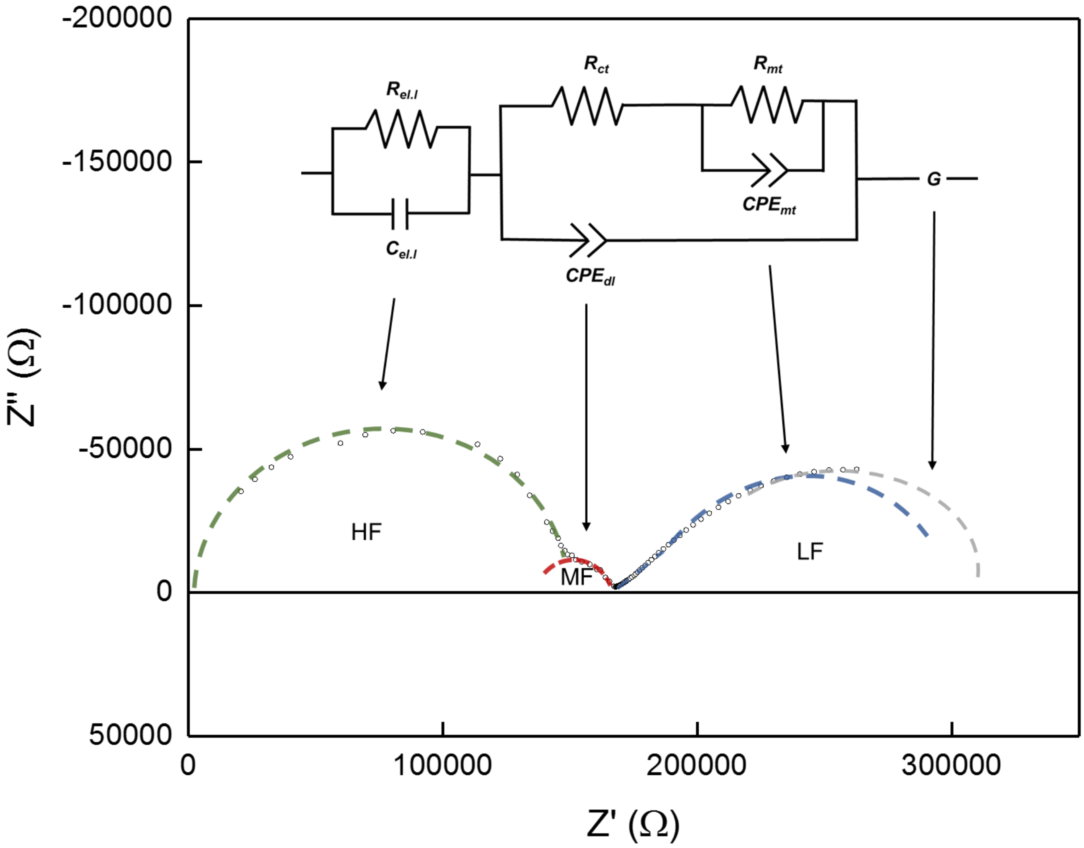

Figure 4.6 Nyquist plot of EIS measurement showing the peak frequencies of contributions assigned to the electrolyte (HF), charge transfer (MF) and mass transfer (LF) contributions.

4.4.2 Electrochemical Analysis

The data obtained from the deconvolutions of the impedance spectra were collected in a spreadsheet in Origin. Plots of temperature, pO_2 and pH_2O dependencies of the charge and mass transfer resistances and their corresponding capacitances in logarithmic scale were used to analyse the general trends. Linear regression was used to obtain the reaction orders for pO_2 and pH_2O dependencies. Furthermore, the activation energies and pre-exponential values for the different processes was determined through Arrhenius plots. As the various data yields information about different parts of the reaction mechanism, reaction models with elementary steps have been developed, and the rate-determining step has been suggested based on the calculations.

4.5 Error and Uncertainty

There are numbers of sources of errors associated with the experimental methods presented here, therefore ascertaining all sources of error and uncertainties is highly unrealistic. However, identifying as many as possible is essential to avoid or minimise them. Systematic errors associated with characterisation methods such as SEM and XRD are well documented and will, therefore, not be discussed.

Firstly, during synthesis, a small number of impurities must be considered regardless of cleaning thorough cleaning of the equipment. Moreover, uncertainties during weighing may occur as the analytical balance used has an uncertainty of ± 0.1 mg.

The gas mixer utilised to regulate the atmosphere in the ProboStat™ during electrochemical measurements may be sources of several errors including gas leakages. According to the manual, the pH_2O of the gas is expected to be $< 1\cdot10^{-6}$ atm after passing the drying stage. However, due to leakages in the system, the values were estimated to be around $3\cdot10^{-5}$ atm by Kofstad and Norby [74]. Furthermore, each flow meter exhibits an accuracy of ± 5 %, which means that the uncertainty increases with the number of flow meters in the gas mix system.

The three-electrode setup for solid-state systems is uncertain due to the much higher resistance of solid electrolytes. The external placement of the reference electrode on the electrolyte surface can cause inaccuracy and misleading results if it is incorrectly placed. The RE should be placed such that the RE equipotential lines does not change position between the high and the low-frequency limit. Ideally, the counter electrode should be symmetrically aligned with the working electrode.

5 Results

In this section, all the research findings are presented. Firstly, the experimental results from microstructure analysis using SEM and EDX are introduced, along with structural characterisation and density measurements through XRD. The following sections focus on the outcomes from the electrochemical measurements carried out under varying conditions.

5.1 Sample Characterisation

Before the electrochemical measurements, the microstructure, the composition and the densities of the sintered pellets were examined. The electrode material should be as dense as possible to obtain better control of the geometry and the contact area. A porous electrode structure is complex and undefined, which may lead to unreliable information about the positrode reaction mechanism. Hence, sintered pellets with relative densities of >80% were used for electrochemical measurements. Higher density was achieved for BGLC1082, >90%, sintered at 1180 °C than SFM25 sintered at 1200 °C.

5.1.1 Microstructure

The microstructure of as-sintered pellets was analysed with SEM through magnifications, EDX was used for elemental characterisation. SEM images of the surface of the sintered BGLC and SFM pellets are presented in Figure 5.1 and Figure 5.3, respectively. Figure 5.2 shows the elemental quantification by EDX of average grains and dark spots found on the BGLC surface.

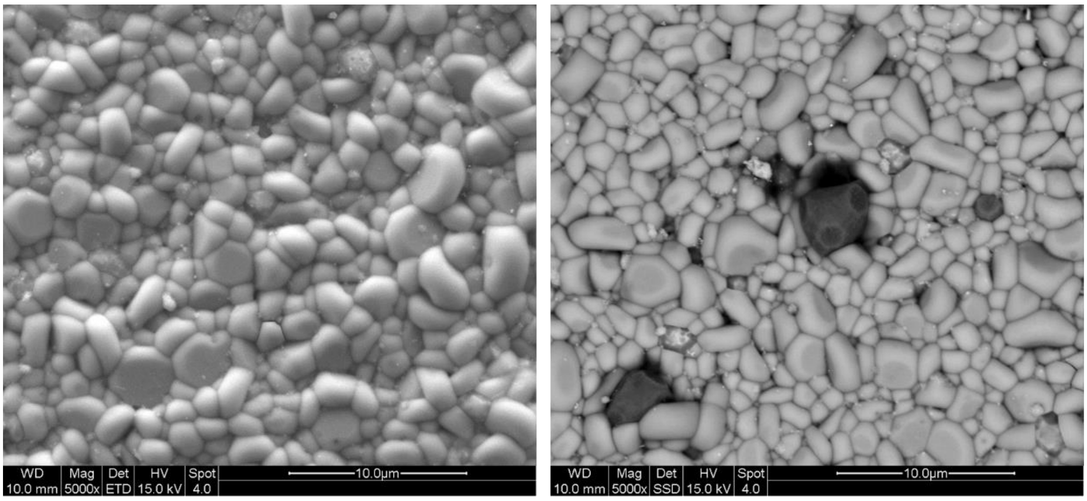

Figure 5.1 Surface of sintered BGLC1082 pellet. The SEM images are taken with ETD (left) and SSD (right) detector. The dark spots are due to the higher content of cobalt on the surface.

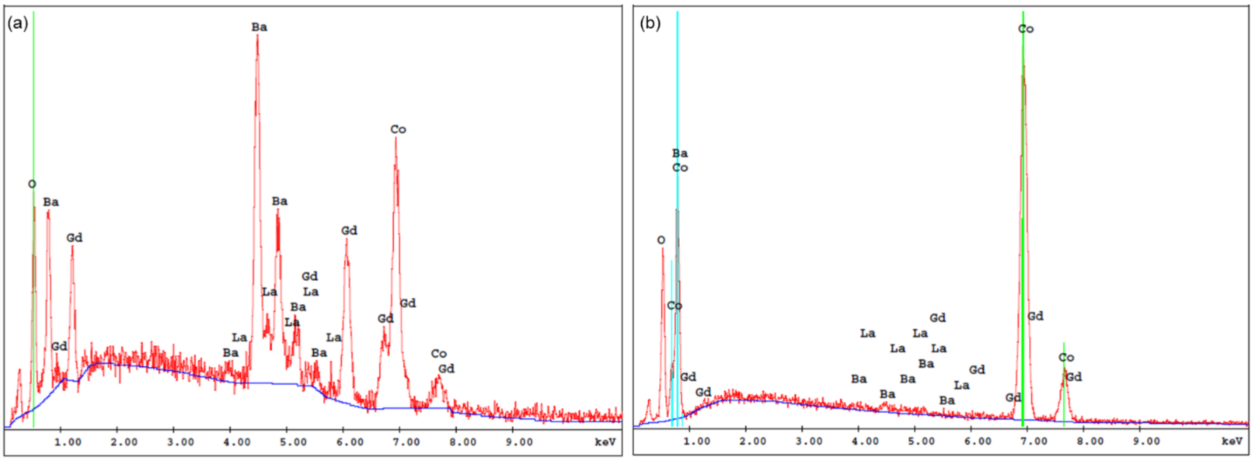

Figure 5.2 EDX spot analysis of BGLC surface where (a) is average grains and (b) is dark spots, as shown in Figure 5.1.

Table 5.1 Atomic percentages of the elements present at the surface of BaGd$_{0.8}$La$_{0.2}$Co$_2$O$_{6-\delta}$ obtained from EDAX analysis of average grains and dark spots.

Element	At % average grains	At % dark spots
Ba	20.77	0.69
Gd	18.68	0.39
La	3.95	0.28
Co	40.06	82.86
O	16.55	15.77

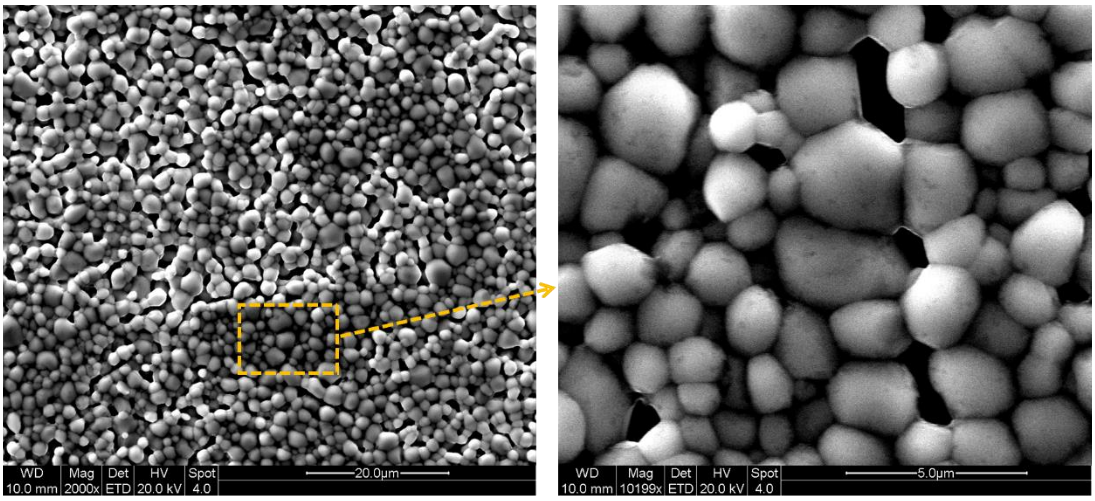
WD
Mag
Det
HV
Spot
10.0 mm
2000x
ETD
20.0 kV
4.0
20.0µm
WD
Mag
Det
HV
Spot
10.0 mm
10199x
ETD
20.0 kV
4.0
5.0µm

Figure 5.3 Surface of pressed and sintered pellet of SFM25 in two different magnifications.

Table 5.2 Atomic percentages of the elements present at the surface of $SrFe_{0.75}Mo_{0.25}O_{6-\delta}$ obtained from EDAX spot analysis.

Element	**At %**
Sr	48.36
Fe	25.90
Mo	9.49
O	16.24

5.1.2 Crystal Structure

Diffractograms of the sintered BGLC and SFM pellets obtained from XRD at room temperature were analysed by Rietveld refinement method. The Rietveld pattern from structure refinement for BGLC and SFM are presented in Figure 5.5 and Figure 5.6, respectively. SFM exhibit a simple cubic structure and show no secondary phases. Diffractogram of BGLC shows a tetragonal structure of the double perovskite. However, there are also peaks which correspond to secondary phases identified as cubic CoO and Co_3O_4.

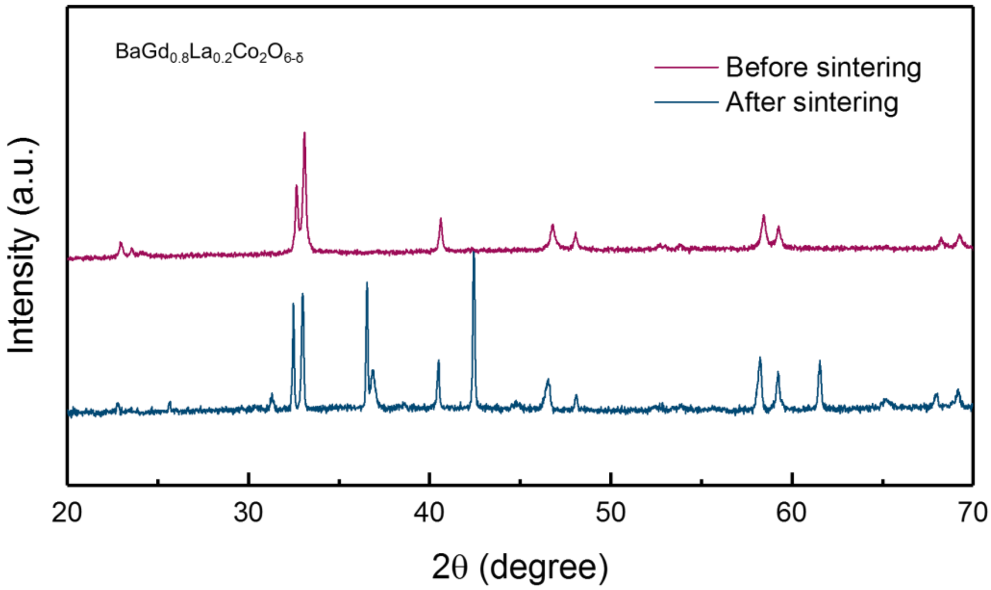

Figure 5.4 Diffractograms of BGLC before sintering[5] (purple) and after sintering (blue) at 1180 °C.

---

[5] The XRD measurement before sintering was conducted by Vøllestad and Strandbakke of BGLC1082 powder from the supplier and was later pressed and sintered and further studied in this work.

Table 5.3 Measured, theoretical and relative densities of the sintered BGLC1082 and SFM25 pellets used in electrochemical measurements. The theoretical density is obtained through refinement.

Compound	**Measured density ρ_m (g/cm^3)**	**Theoretic density ρ_t (g/cm^3)**	**Relative density ρ_r (%)**
BGLC1082	6.78(4)	7.04(1)	96.35
SFM25	4.56(4)	5.54(9)	82.25

The theoretical densities in Table 5.3 are determined through Rietveld refinement.

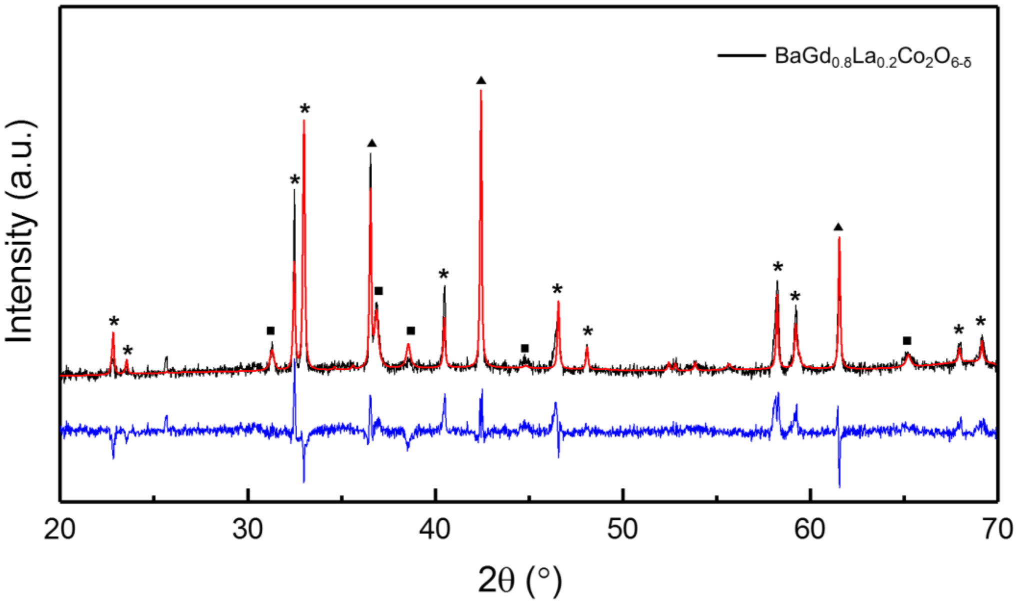

Figure 5.5 X-ray diffraction pattern (black line) for BGLC1082 pellet sintered at 1180 °C in air. Peaks for the tetragonal structure of the double perovskite BGLC are marked with *. Peaks that belongs to secondary phases of cubic CoO and Co_3O_4 are marked with ▲ and ■, respectively. The red line is the calculated pattern from the Rietveld pattern from the structure refinement analysis red line is while the blue line is the difference between the observed and calculated pattern.

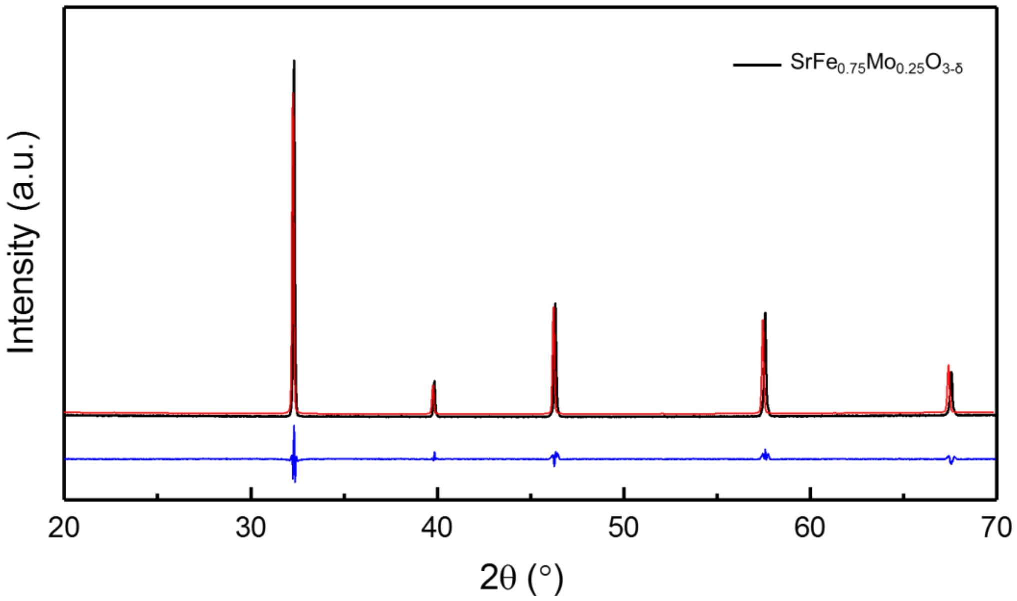

Figure 5.6 Rietveld pattern from the structure refinement analysis of XRD data for SFM25. The black line is the diffraction pattern, while the red line is the calculated pattern. The blue line is the difference between the observed and calculated pattern. The double perovskite exhibits a cubic crystal structure.

Table 5.4 Cell parameters from Rietveld refinement of the studied compounds

Compound	Space group	Cell parameters (Å)	Cell volume (Å^3)
BGLC1082	*P4/mmm*	a = 3.9022(3) c = 7.5701(7)	155.27(2)
SFM25	$Fm\overline{3}m$	a = 7.8423(3)	482.32(5)

5.1.3 Post Characterisation

After the electrochemical measurements, footmark from the electrode on the surface of the BZCY electrolyte was studied through a light microscope. Figure 5.6 shows the rectangularly shaped contact area after BGLC. By means of a digital ruler under and magnification glass, the contact area was estimated to 0.015 cm^2 for BGLC and 0.028 cm^2 for SFM.

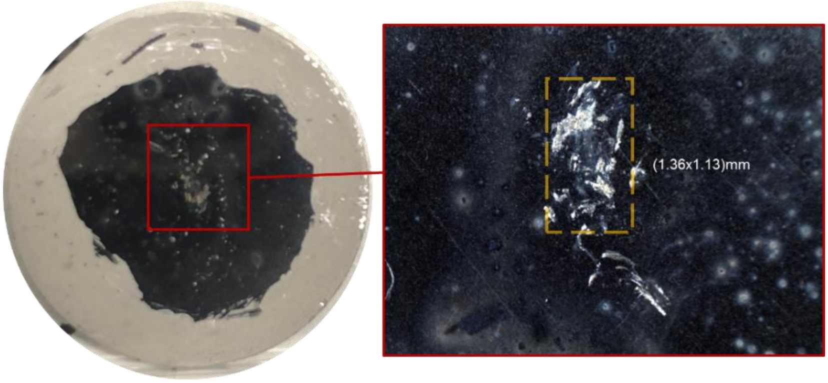

Figure 5.7 Footprint of vertically placed BGLC working electrode on the proton ceramic BZCY72 electrolyte after electrochemical measurements. The rectangular print was measured with a digital ruler (0.015 cm^2) through a magnification glass. The grey ring is the painted reference electrode of Pt.

The results from electrochemical measurements, presented in the following section, were corrected by the measured contact area.

5.2 Electrochemical Measurements

EIS measurements were carried out at OCV under zero DC conditions as a function of temperature and partial pressure of oxygen and water vapour. The impedance spectra yield information of several contributions which can be assigned to particular processes at the interface by deconvolution. Each of the three semi-circles was correlated to the corresponding process through their capacitances. An example of fitting of an impedance spectrum using Randles type equivalent circuit is presented in Figure 5.8. R1 was assigned to the electrolyte. R2 to the charge transfer and R3 to the mass transfer contribution. Whereas high and low-frequency arcs were visible, the mid-frequency response related to charge transfer was more challenging to distinguish and exhibits a higher uncertainty. Furthermore, Gerischer impedance (GE) at low frequency was applied when CPE3 was ill-defined, the GE resistance was added to the mass transfer contributions.

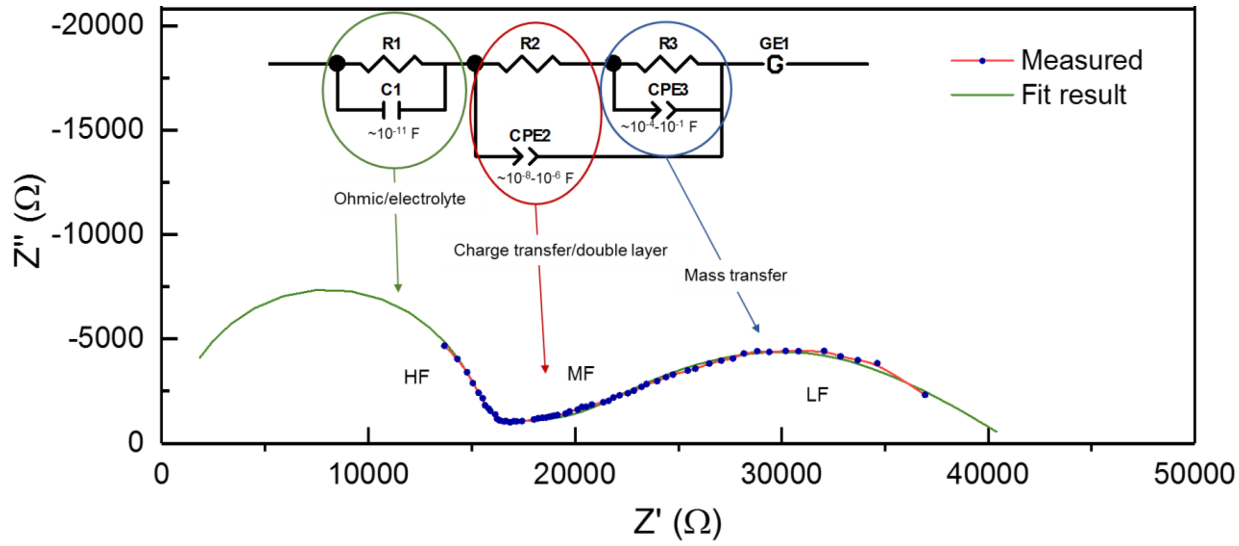

Figure 5.8 EIS spectra resolved with a Randles type equivalent circuit. High frequency (HF) response corresponds to the ohmic contribution, mid-frequency (MF) to the charge transfer and low-frequency (LF) to the mass transfer contribution. The Nyquist plot was obtained by potentiostatic EIS measurement at OCV under wet air (0.20 atm and 0.025 atm pO_2 and pH_2O respectively) at 500 °C.

The resistances and the corresponding capacitances of the various contributions as a function of T, pO_2 and pH_2O are presented in the following sections.

5.2.1 Temperature Dependencies

Both ohmic and polarisation resistances show dependence on temperature.

The Arrhenius plot of R_p in Figure 5.9 shows inconsistent linearity for BGLC. In the low-temperature range, R_p for mass transfer is not as steep as at higher temperatures indicating that the dominating electrode process varies with temperature. The plot of capacitances as a function of temperature reveals that with decreasing temperatures, the double layer and mass transfer contributions overlap and becomes more challenging to distinguish.

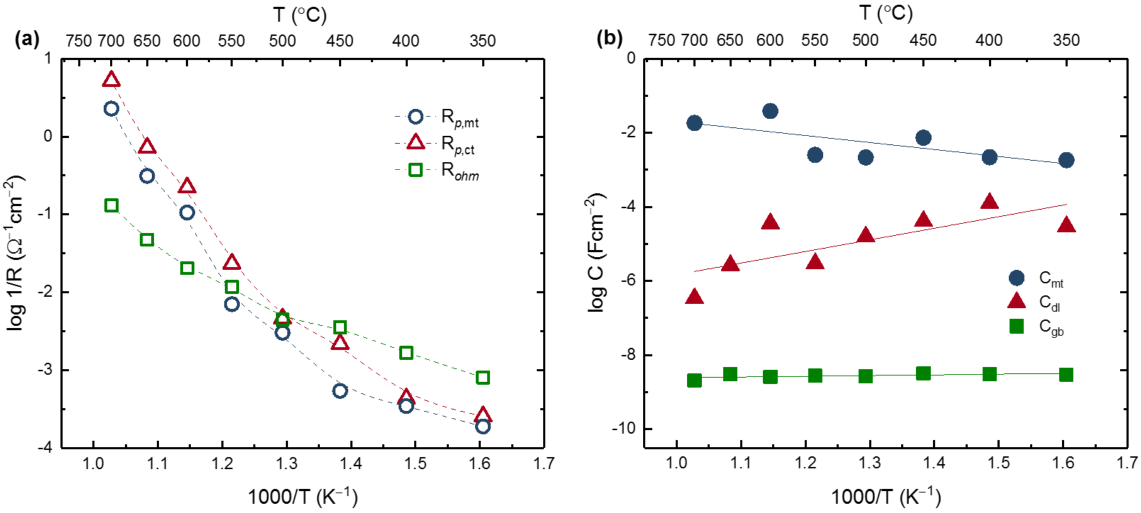

Figure 5.9 Temperature dependencies on BGLC positrode and proton ceramic BZCY electrolyte of (a) the ohmic, charge transfer and mass transfer resistances and the corresponding (b) capacitances of the grain boundary (gb), double layer (dl) and mass transfer. EIS measurements were carried out at OCV under wet air; 0.20 atm pO_2 and 0.025 atm pH_2O

In contrast to BGLC, SFM follows a persistent linear trend for the temperature dependency of R_{p}, as shown in Figure 5.10. Moreover, the double layer and mass transfer capacitances for SFM exhibit opposite temperature dependency than for BGLC, also with decreasing temperature the double layer and electrolyte capacitance values gets similar.

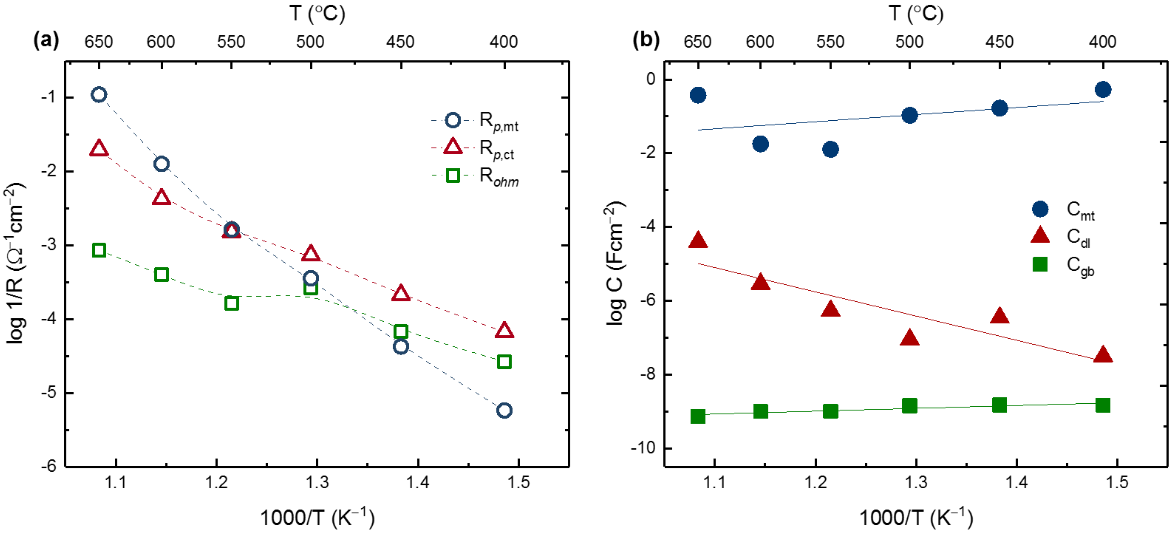

Figure 5.10 Temperature dependencies on SFM positrode and proton ceramic BZCY electrolyte of (a) the ohmic, charge transfer and mass transfer resistances and the corresponding (b) capacitances of the grain boundary (gb), double layer (dl) and mass transfer. EIS measurements were carried out at OCV under wet air; 0.20 atm pO_2 and 0.025 atm pH_2O

Table 5.5 Capacitance values of the grain boundary (gb), double layer (dl) and mass transfer (mt) contribution measured at high, intermediate and low temperature on BGLC and SFM.

	T (°C)	C_{gb} (Fcm^{-2})	C_{dl} (Fcm^{-2})	C_{mt} (Fcm^{-2})
BGLC	700	$2.067\cdot10^{-9}$	$3.427\cdot10^{-7}$	$1.835\cdot10^{-2}$
	500	$2.677\cdot10^{-9}$	$1.572\cdot10^{-5}$	$2.160\cdot10^{-3}$
	350	$3.002\cdot10^{-9}$	$2.968\cdot10^{-5}$	$1.810\cdot10^{-3}$
SFM	650	$7.123\cdot10^{-10}$	$3.975\cdot10^{-5}$	$3.771\cdot10^{-1}$
	500	$1.424\cdot10^{-9}$	$8.887\cdot10^{-8}$	$1.062\cdot10^{-1}$
	400	$1.467\cdot10^{-9}$	$3.144\cdot10^{-8}$	$5.356\cdot10^{-1}$

Table 5.6 Ohmic and polarisation resistances at BGLC and SFM positrodes with proton conducting BZCY electrolyte. The values for each positrode material were obtained at high, intermediate and low temperatures. The measurements were carried out in 0.20 atm pO_2 and 0.025 atm pH_2O.

	T (°C)	R_{ohm} (Ωcm^2)	$R_{p,\mathrm{ct}}$ (Ωcm^2)	$R_{p,\mathrm{mt}}$ (Ωcm^2)
BGLC	700	7.653	0.192	0.437
	500	223.830	216.690	329.910
	350	1239.285	3910.350	5287.572
SFM	650	1166.832	50.400	9.003
	500	3776.544	1349.597	2785.334
	400	37673.280	14935.392	172779.840

As presented in Table 5.6, SFM exhibits larger polarisation resistance for charge transfer than mass transfer at higher temperatures (>500 °C). Contrary, the polarisation resistance for charge transfer at BGLC is lower than that for mass transfer at all temperature ranges.

Activation Energies

Figure 5.11 shows the Arrhenius plots of the ohmic and the polarisation conductance for BGLC from 350 °C to 700 °C. The activation energies, E_a, and the pre-exponential factor, A_o, for the three contributions were determined by linear regression of ln (1/R_{ohm} T) vs 1/T for electrolyte and ln (1/R_p) vs 1/T for electrode processes through the following expression:

$$\frac{1}{R} = A_o \, pO_2^m \, pH_2O^n \;\; exp\left(-\frac{E_a}{RT}\right), \tag{5.1}$$

where R is the gas constant, T is the temperature in Kelvin and m and n corresponds to the dependencies of pO_2 and pH_2O, respectively.

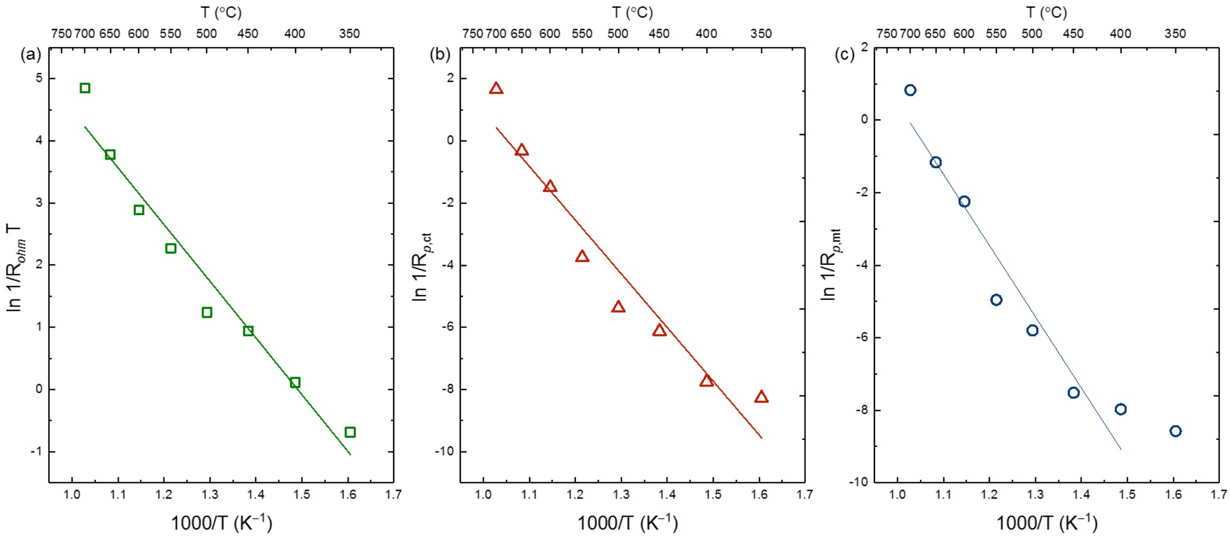

Figure 5.11 Arrhenius plots of the (a) ohmic, (b) charge transfer and (c) mass transfer contributions at BGLC positrode and proton ceramic BZCY electrolyte.

Table 5.7 Activation energies and the pre-exponential factors for the different contributions at BGLC positrode and proton conducting BZCY electrolyte.

Contribution	**T (°C)**	**E_a (eV)**	**Pre-exponential factor**
Ohmic	350 – 700	0.785 (± 0.065)	$8.01 \cdot 10^{5}$ (± 2.650)
Charge transfer	350 – 700	1.344 (± 0.156)	$7.29 \cdot 10^{6}$ (± 11.141)
	350 – 500	0.849 (± 0.136)	$1.52 \cdot 10^{3}$ (± 9.785)
Mass transfer	350 – 700	1.410 (± 0.187)	$1.17 \cdot 10^{7}$ (± 16.544)
	350 – 450	0.410 (± 0.016)	$3.97 \cdot 10^{-1}$ (± 1.323)
	550 – 700	2.549 (± 0.253)	$3.52 \cdot 10^{13}$ (± 26.954)

The Arrhenius plots of the three contributions for SFM in temperature range 400-650 °C are presented in Figure 5.12.

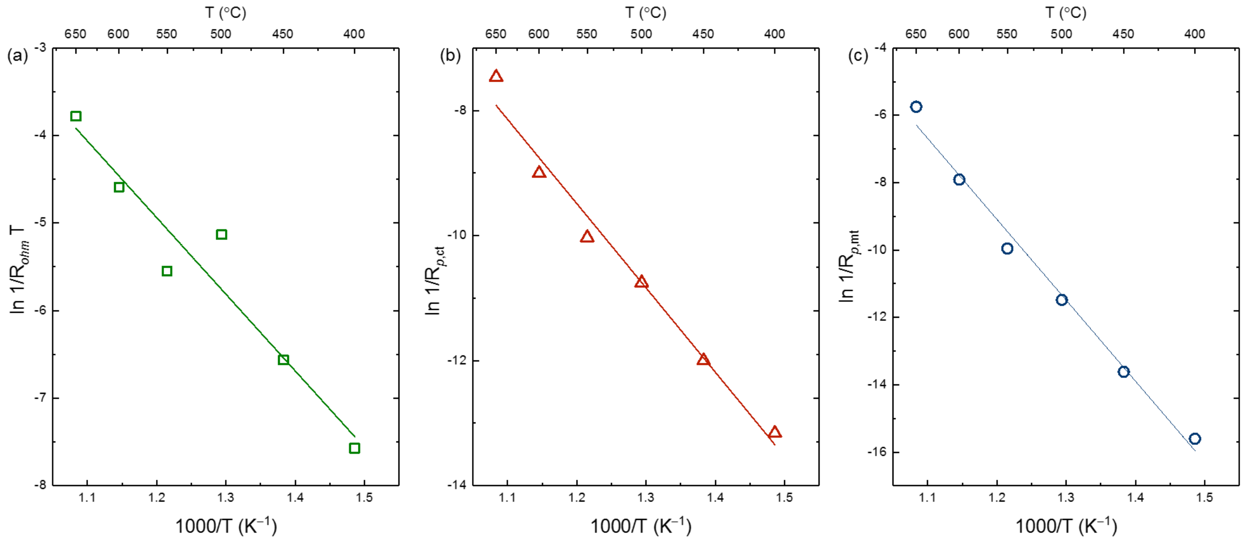

Figure 5.12 Arrhenius plots of the (a) ohmic, (b) charge transfer and (c) mass transfer contributions for SFM positrode and proton ceramic BZCY electrolyte.

Table 5.8 Activation energies and the pre-exponential factors for the different contributions at SFM positrode and proton conducting BZCY electrolyte.

Contribution	**T (°C)**	**E_a (eV)**	**Pre-exponential factor**
Ohmic	400 – 650	0.754 (± 0.105)	$2.58\cdot10^{2}$ (± 4.738)
Charge transfer	400 – 650	1.161 (± 0.083)	$7.95\cdot10^{2}$ (± 3.398)
Mass transfer	400 – 650	2.069 (± 0.109)	$3.72\cdot10^{8}$ (± 5.024)

As the same proton conducting electrolyte is applied for both positrode materials, the resulting activation energies for electrolyte is therefore very similar. The pre-exponential factor is temperature-independent but depends significantly on geometric factors, the concentration of species and attempt rates. Although the activation energies of charge transfer reaction are comparable for BGLC and SFM, 1.34 and 1.16 eV respectively, the charge transfers pre-exponential factor for BGLC is considerably larger than for SFM.

5.2.2 Partial Pressure Dependencies

The effect of varying partial pressures of oxygen and water vapour in the atmosphere yields essential information about the positrode reaction mechanism. By varying temperatures, the dominating charge carriers, their motilities and conductivities changes. By varying partial pressures at the same temperatures, the concentration of the involved species changes, which exposes details of how the positrode reaction occurs, which species are involved, and how they react to the atmosphere. The trends differ to some degree for the two positrode materials as

BGLC is an MPEC and SFM is an O-MIEC. The partial pressure dependencies for both positrode materials are presented in this section.

*p*O₂ - Dependency

The presence of oxygen in the atmosphere is essential for the positrode reaction. By regulating the oxygen partial pressure, the effect on each contribution can be studied. EIS spectra under varying pO_2 at 500 °C are shown in Figure 5.13, the mid-frequency range which is assigned to polarisation resistance (R_p) of the charge transfer process shows no visible change in the EIS spectra. However, the low-frequency response, assigned to R_p of the mass transfer contribution, shows considerable variation from high to low pO_2.

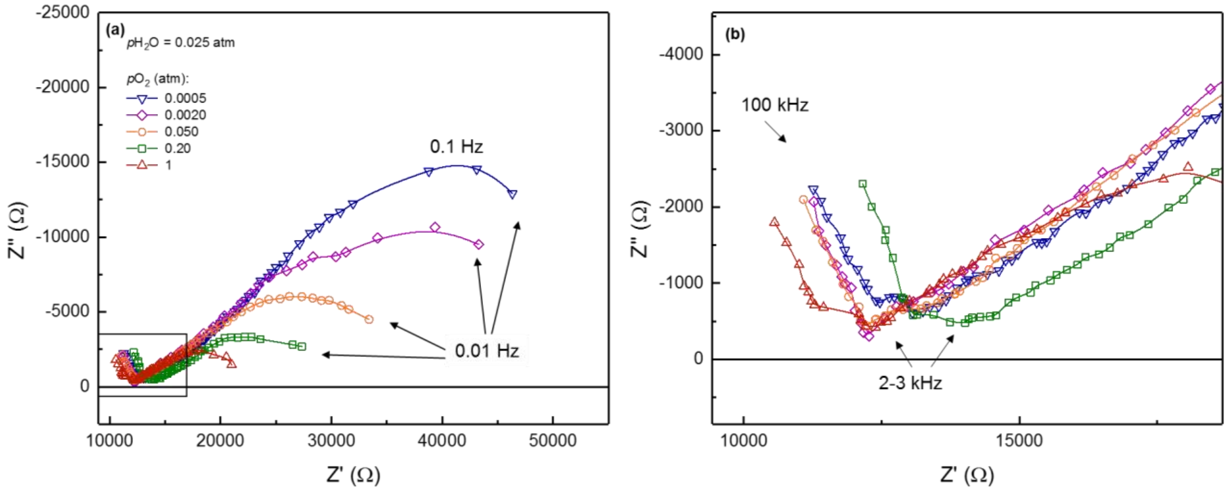

Figure 5.13 Typical EIS spectra obtained under various oxygen partial pressures at 500 °C for BGLC positrode. The sweeps are obtained in the frequency range of (a) 100 kHz to 0.01 Hz. The high-frequency response (b) is from the proton conducting BZCY electrolyte.

By deconvoluting these spectra, the resistances and capacitances of the different contributions were distinguished for every experimental test matrix. The double layer and mass transfer capacitances from deconvolution are presented as a function of pO_2 for BGLC in Figure 5.13.

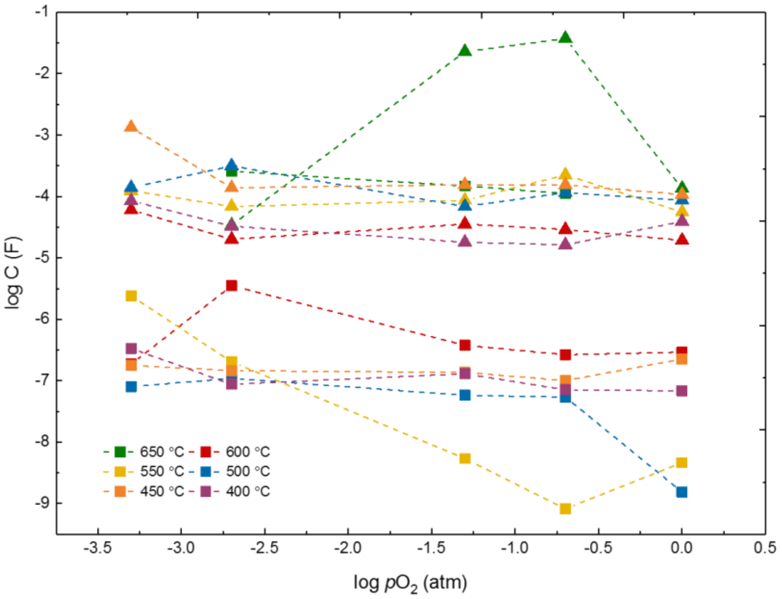

Figure 5.14 Double layer (■) and mass transfer (▲) capacitances as a function of oxygen partial pressure at various temperatures for BGLC positrode.

The dependencies of pO_2 of the ohmic $1/R_{ohm}$ and the two $1/R_p$ for charge and mass transfer at various temperatures for BGLC and SFM are presented in Figure 5.15, Figure 5.16 and Figure 5.17, respectively.

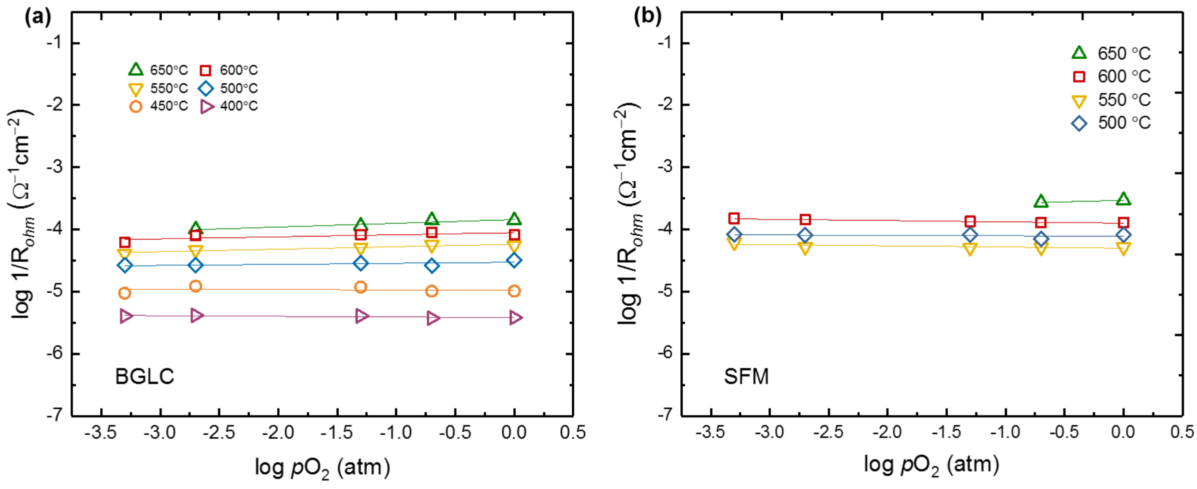

Figure 5.15 Oxygen partial pressure dependencies of the ohmic contribution at various temperatures for (a) BGLC and (b) SFM.

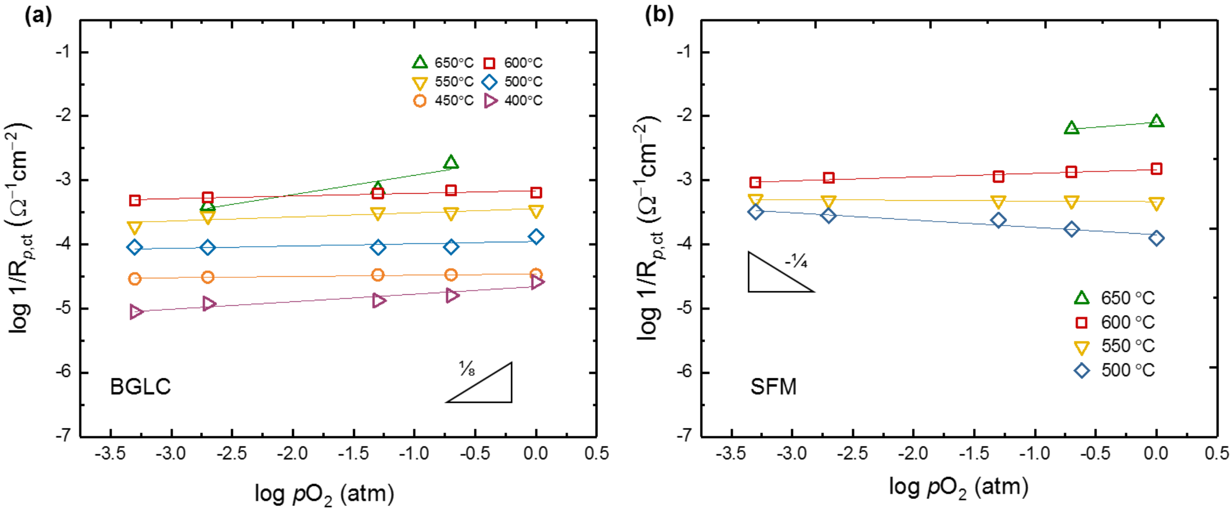

Figure 5.16 Oxygen partial pressure dependencies of the charge transfer contribution at various temperatures for (a) BGLC with a slope of ⅛ at 650°C and (b) SFM where the dependency is – ¼ at 500°C

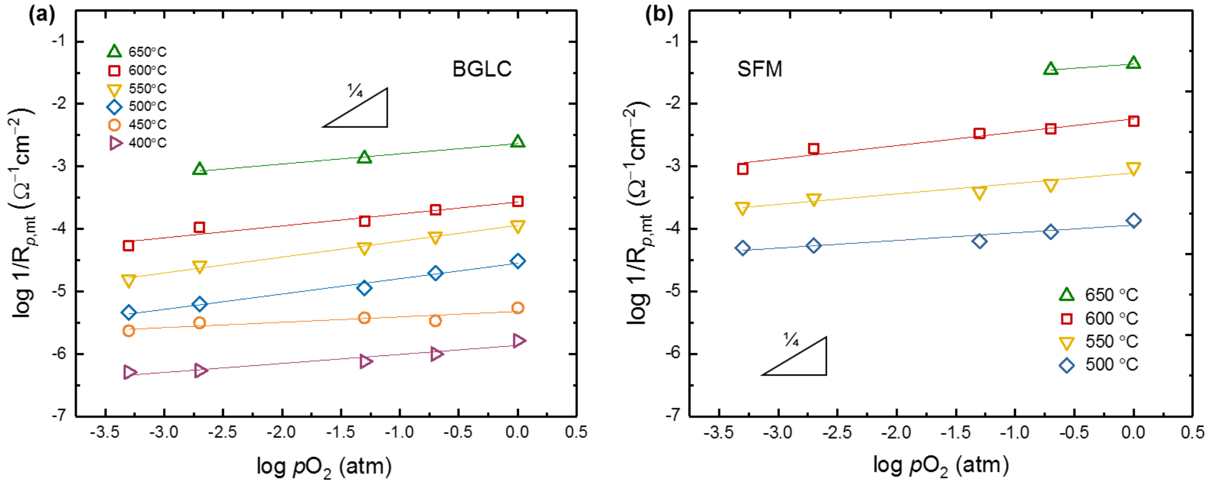

Figure 5.17 Oxygen partial pressure dependencies of mass transfer contribution at various temperatures for (a) BGLC and (b) SFM.

At higher temperatures (> 500 °C), there is a slight increase in the electrolyte conductivity with increasing pO_2 indicating the p-type conductivity for BZCY. Whereas R_p for charge transfer contribution shows slight pO_2 dependency, the mass transfer R_p shows stronger dependency with increasing temperature, which will be discussed later.

pH_2O - Dependency

Figure 5.18 presents Nyquist plots for a series of pH_2O-dependencies. The low-frequency arcs increased significantly with increasing pH_2O. Figure 5.18 (b) demonstrates the high-frequency response assigned to the ohmic, often electrolyte or grain boundary, contribution, and is thus not expected to vary with partial pressure. Though, the electrode may contribute to the ohmic resistance.

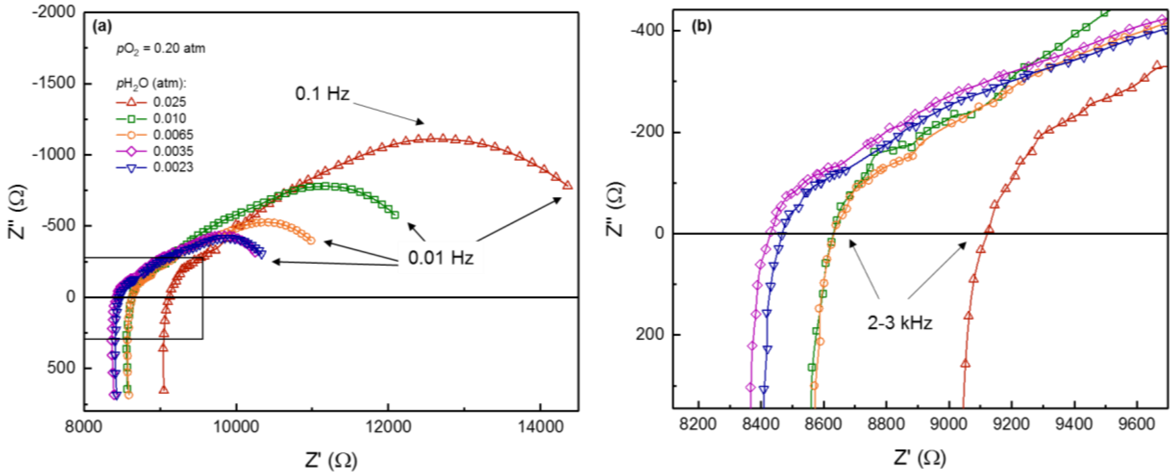

Figure 5.18 Average series of EIS spectra obtained under various water vapour partial pressures at 550 °C for BGLC positrode. The impedance sweeps are obtained in the frequency range of (a) 100 kHz to 0.01 Hz. The high-frequency response (b) is from the proton conducting BZCY electrolyte.

The pH_2O dependencies for the ohmic and charge transfer are presented in Figure 5.19 and 5.20, respectively, for BGLC and SFM positrodes. The $1/R_{ohm}$ did not show any pH_2O dependency while the $1/R_{p,ct}$ increases with increasing pH_2O.

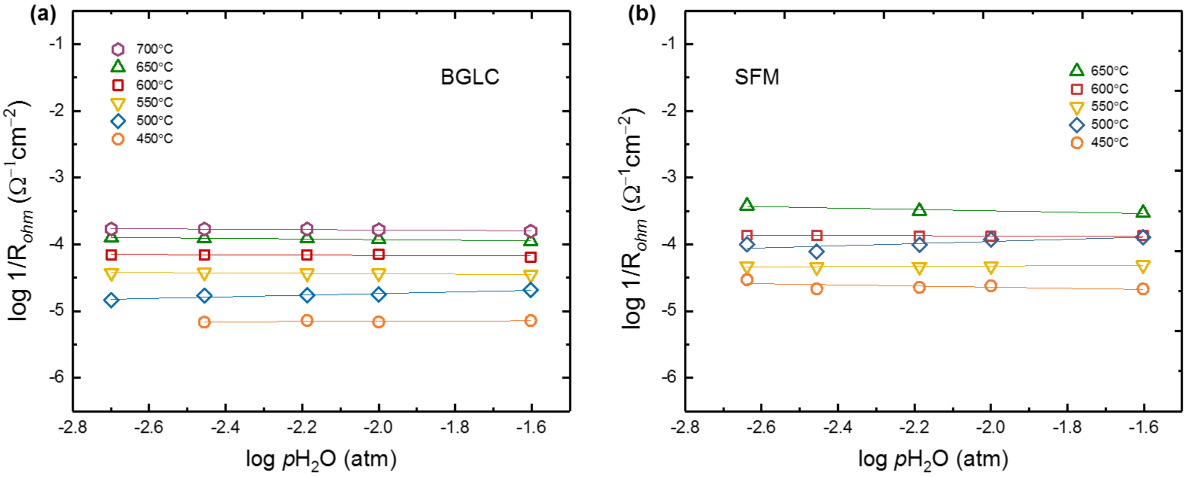

Figure 5.19 Water vapour partial pressure dependencies of the ohmic contribution at various temperatures for (a) BGLC and (b) SFM.

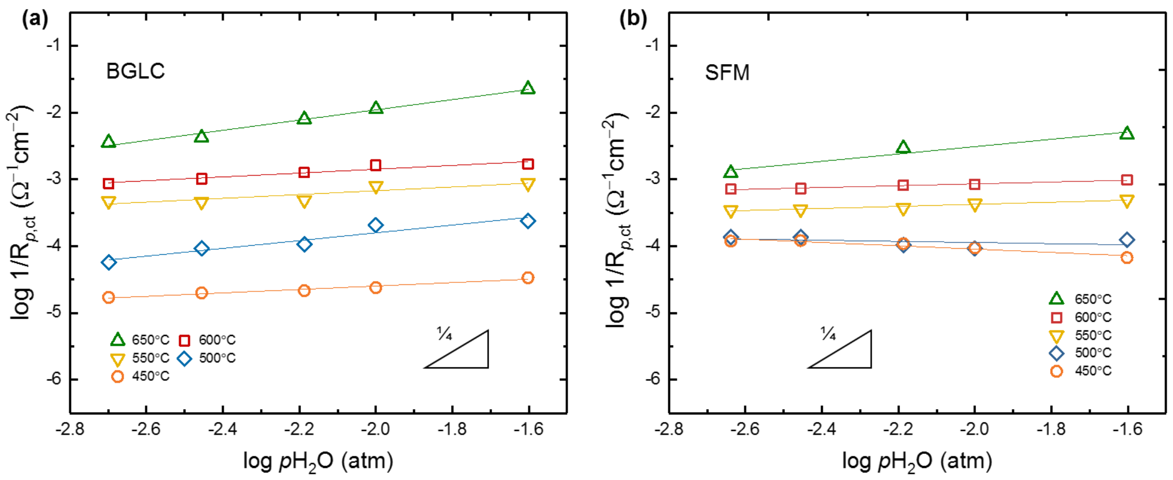

Figure 5.20 Water vapour partial pressure dependencies of the charge transfer contribution at various temperatures for (a) BGLC and (b) SFM.

In contrast to the ohmic and charge transfer resistances, the pH_2O dependency for mass transfer $1/R_p$ yields an opposite trend for both BGLC and SFM, as shown in Figure 5.21. The negative pH_2O dependency of the $1/R_{p,mt}$ emphasises the involvement of protons in the positrode reaction. The surplus water has an undesirable effect on positrode performance.

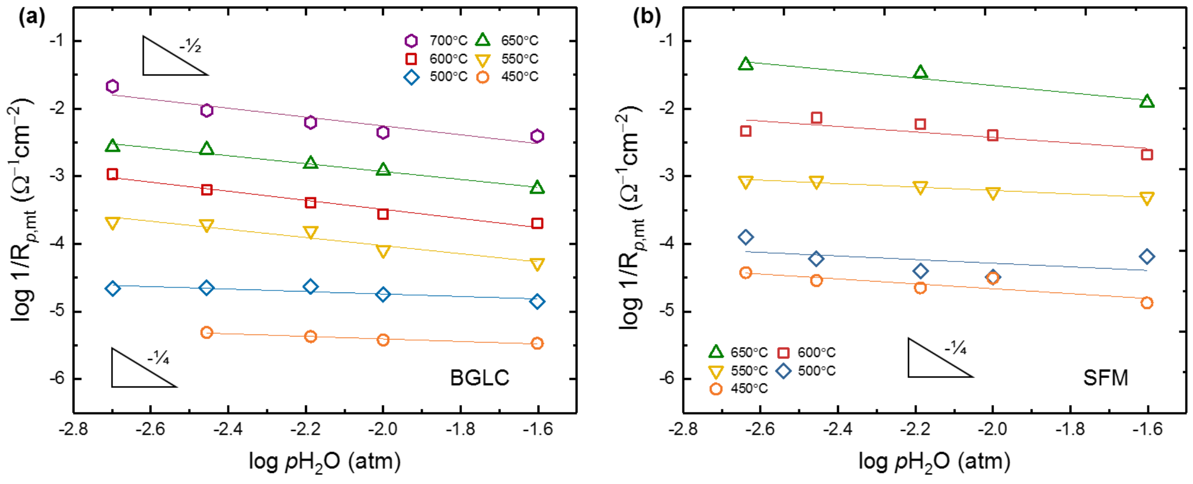

Figure 5. 21 Water vapour partial pressure dependencies of the mass transfer contribution at various temperatures for (a) BGLC and (b) SFM.

Reaction Orders

The oxygen and water vapour partial pressure dependencies, i.e. the *m* and *n* values, respectively, of the electrode contribution, are presented in Table 5.9 and 5.10 for BGLC and SFM, respectively.

Table 5.9 The reaction orders for charge and mass transfer $1/R_p \propto (pO_2)^m\ (pH_2O)^n$ for BGLC

Temperature (°C)	m_{ct}	n_{ct}	m_{mt}	n_{mt}
700	~0	~1	--	- ⅝
650	0	¾	¼	- ½
600	0	¼	¼	- ⅝
550	0	¼	¼	- ½
500	0	½	¼	- ¼
450	0	¼	⅛	- ¼
400	⅛	--	⅛	--

Table 5.10 The reaction orders for charge and mass transfer $1/R_p \propto (pO_2)^m\ (pH_2O)^n$ for SFM

Temperature (°C)	m_{ct}	n_{ct}	m_{mt}	n_{mt}
650	¼	½	⅛	- ½
600	0	¼	¼	- ⅜
550	0	¼	¼	- ¼
500	⅛	~0	⅛	- ¼
450	--	- ½	--	- ⅜

5.2.3 Effect of DC Bias

Nyquist plots obtained by potentiostatic EIS measurements with anodic DC biases for BGLC at 350 °C are shown in Figure 5.22.

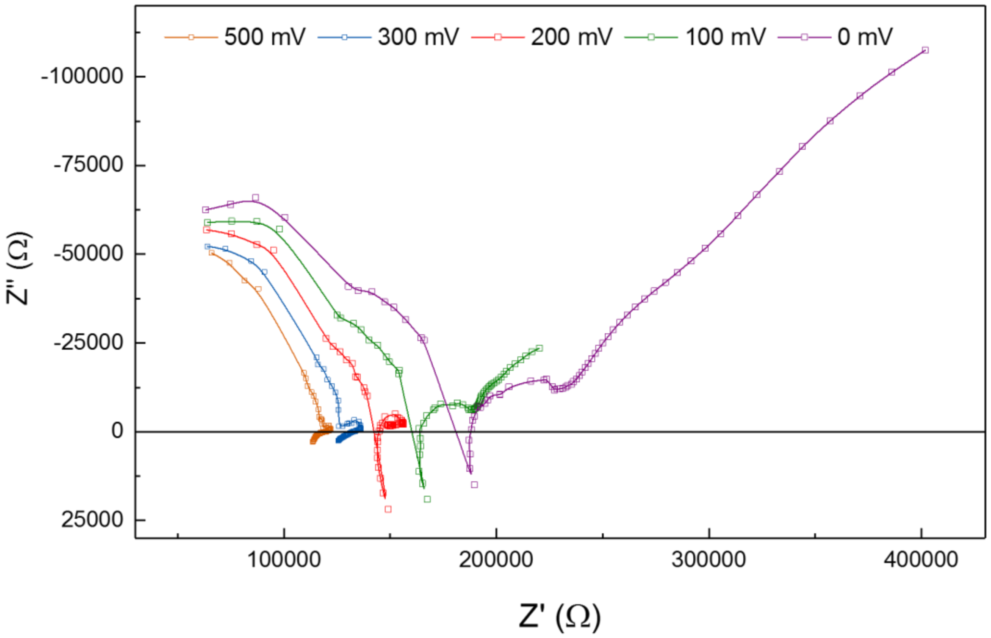

Figure 5.22 EIS spectra obtained at OCV and applied DC potentials for BGLC at 350 °C in wet air with 60 mV AC amplitude. Both real and imaginary impedance decreases with increasing applied potential.

5.3 Electrochemical Interpretation

Results from electrochemical measurements performed on the model electrode for both positrode materials presented in chapter 5.2 yields information about the electrochemical processes taking place at the positrode/electrolyte interface and the surface of the positrodes. The partial pressure dependencies reveal the presence and type of species which may be involved in the various processes which constitute the positrode reaction. However, the reaction mechanism and furthermore the rate-limiting steps cannot be determined only by the partial pressure dependencies. Activation energies and the following pre-exponential factors correspond to different processes as each elementary step is either a transfer or reaction of species, changes in these values may be indicative of changes in dominating charge carriers and rate-limiting steps. In this chapter, temperature dependencies of the charge and mass transfer contributions in varying oxygen and water vapour pressures are presented and will be further discussed in the next section.

Charge Transfer

The frequency response assigned to the charge transfer reaction did not exhibit any significant pO_2. However, the temperature dependency with different content of oxygen in the atmosphere may yield a different temperature dependency and thus different activation energy and pre-exponentials.

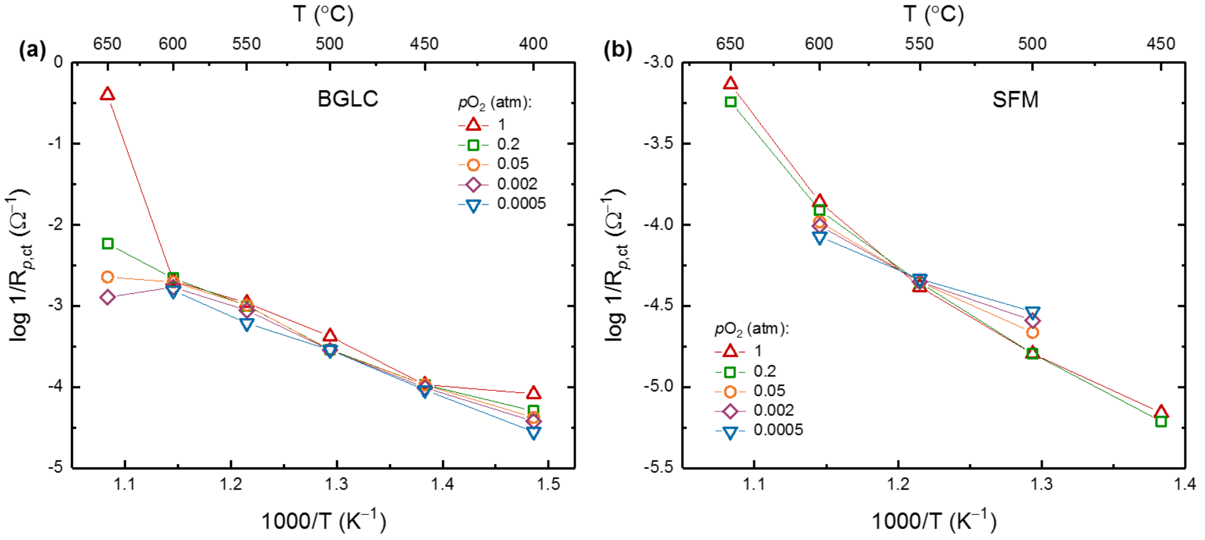

Figure 5.23 Temperature dependencies of charge transfer in various pO_2

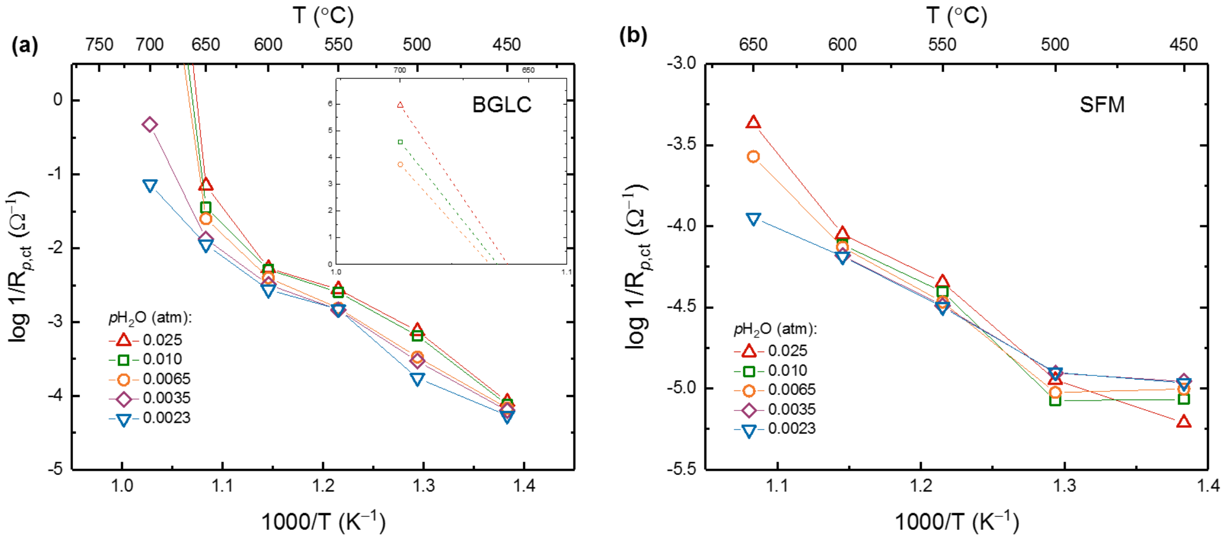

Figure 5.24 Temperature dependencies of charge transfer in various pH_2O

Mass Transfer

The mass transfer reaction exhibits stronger dependencies on both

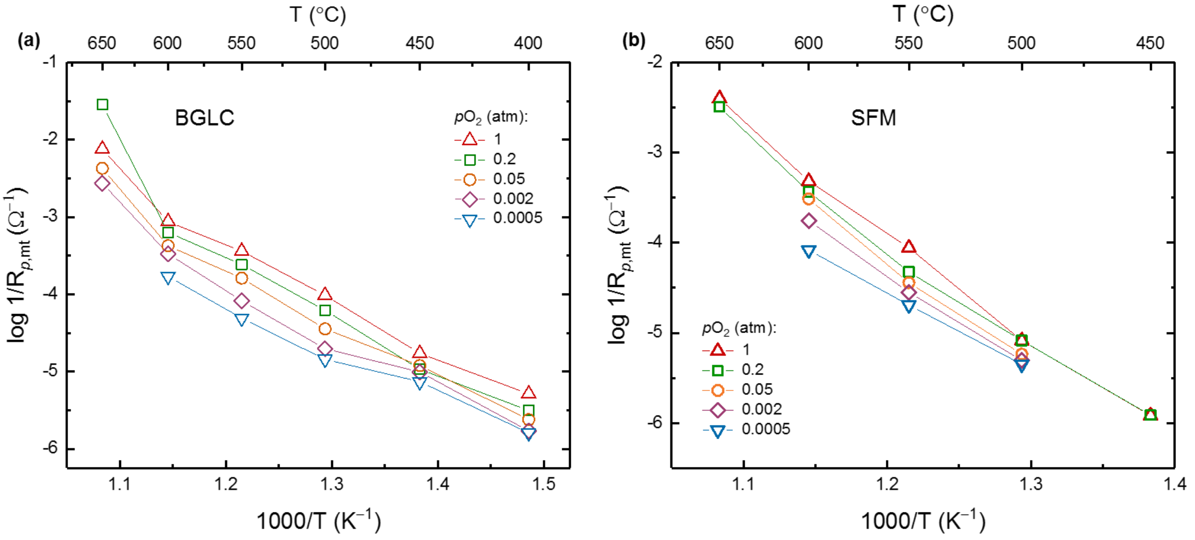

Figure 5.25 Temperature dependencies of mass transfer in various pO_2

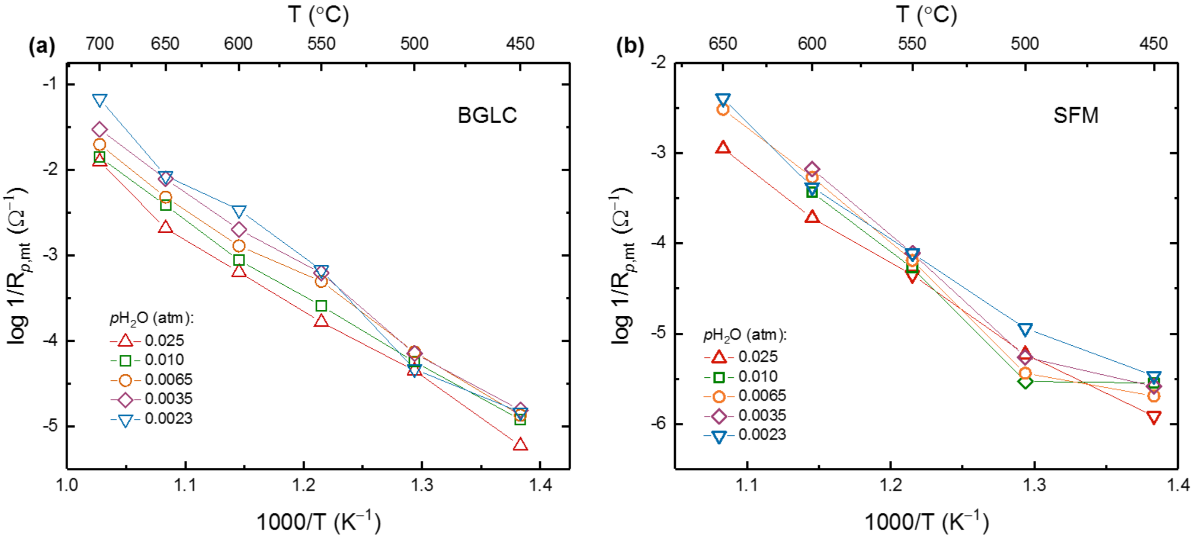

Figure 5.26 Temperature dependencies of mass transfer in various pH_2O

6 Discussion

Interpretation and discussion of the findings in this work are presented in this section with a focus on the development and comparison of the two reaction models describing the positrode reaction mechanism for PCECs concerning BGLC and SFM as positrode materials. Initially, the properties of the materials are discussed. Further on, reaction models for the two materials are developed based on the experimental results. The rate-determining step and reaction pathways are suggested by means of calculated and experimental dependencies for the two positrode materials.

6.1 Crystal Structure and Phase Analysis

The surface of sintered BGLC contains secondary phases of cobalt oxides, which were first observed by SEM through SSD as unevenly distributed dark spots, as shown in Figure 5.1. Furthermore, EDX analysis revealed that the dark spots had an increased concentration (atomic percentage) of Co on compared to average grains, which are presented in Figure 5.2 and Table 5.1. The following characterisation analysis by XRD confirmed the presence of secondary phases containing cobalt on the surface, both cubic CoO and Co_3O_4 was identified (Figure 5.5). Exsolution of cobalt oxides has been observed in double perovskites such as $Ba_{1-x}Pr_{1-x}Co_2O_{6-\delta}$ with under stoichiometry of A-site cation [75].

6.2 Positrode Performance

From the results, it is evident that of the two positrode materials, BGLC showed the best performance. The mass transfer R_p was about 330 and 2790 Ωcm^2 at 500 °C for BGLC and SFM respectively and about 3 and 9 Ωcm^2 at 650 °C. Furthermore, the activation energy for mass transfer at BGLC was estimated at 1.4 eV, much lower than that for SFM, 2.1 eV, for the same contribution. In addition to the lower polarisation resistances and activation energies, measurements were carried out at the temperature as low as 350 °C, which is unexpected for a model electrode where a pellet of the electrode is placed vertically on a button electrolyte supported by alumina sticks to prevent it from tilting during measurements under varying conditions. Although the contact area and the geometry are controlled, the point electrode setup utilised in this work contains several challenges and sources of uncertainty.

The better performance of the BGLC positrode can be considered to be related to the protonic conductivity of the oxide, but it may also be caused by the catalytic activity of the secondary phases of cobalt oxides on the surface.

6.3 Positrode Reaction – Insight

In this section, the results obtained for the two positrode materials are compared and discussed, along with the elaboration of the processes that are expected to participate in the positrode reaction. The differences in BGLC and SFM, i.e. ionic conductivities, transition metals and crystal structure, reveal to what extent the positrode reaction is limited to the properties of the materials concerning the operating conditions. Furthermore, the same systematic measurements performed on a point-contact model electrode using BZCY72 electrolyte for both materials yields information about in what way the different processes at positrodes for PCECs occur and whether the reaction mechanism is analogous to SOECs, as considered in the literature or not. To what degree the protonic conductivity of the positrode affects the PCECs performance will be discussed.

Operating conditions have a strong influence on the reaction mechanism and the kinetics, and considering the properties of the materials, also determines the overall reaction rate and the rate-determining step (RDS). The type of conductivity influences the species that are involved in the different steps and how they are affected by varying conditions.

The experimental results yield information about the involved species and their role in the mechanism. Analysis of the results for the charge and mass transfer contributions obtained from electrochemical measurements are discussed in this section. These electrode processes, explained in broad terms first, will be more closely rationalised in line with the results, which provides the basis for the reaction models presented in the next section.

6.3.1 Charge Transfer

The middle-frequency response with capacitance values from 10^{-8} to 10^{-5} Fcm^{-2} is assigned to the charge transfer contribution. The charge transfer process in this context is the transfer of a proton across a phase boundary, i.e. a proton jumps from the electrolyte bulk into the electrode bulk or to the triple phase boundary (TPB) and vice versa. Although an ion transfer is considered to be a thermally activated process which needs to overcome an energy barrier, it occurs fast and is not expected to be rate determining [45]. Proton transport is a thermally activated hopping mechanism such as the Grotthuss mechanism, which generally entails activation energies approximately around 0.1 and 0.5 eV [76]. Sometimes the activation energy may exceed 0.5 eV [77].

The temperature dependencies of charge transfer resistance for BGLC and SFM are presented in Figure 6.1. Both positrode materials exposed a similar trend; however, the polarisation resistance (R_p) for charge transfer reaction on SFM was about 15 kΩcm^2 at 400 °C, more than six times larger than that for BGLC, which exhibited 2.3 kΩcm^2, at the same temperature. Moreover, the $R_{p,\mathrm{ct}}$ values were as low as 1.4 Ωcm^2 at 650°C for BGLC, while for SFM, the value was about 50.4 Ωcm^2. Regardless of the difference in $R_{p,\mathrm{ct}}$ values, the activation energies were relatively comparable, as presented in Table 5.6 and Table 5.7 for BGLC and SFM, respectively, in the previous section. The activation energy for charge transfer reaction on BGLC increased from about 0.85 eV at low temperatures to 1.34 eV at higher temperatures, slightly higher than that for SFM, which exhibited about 1.16 eV. These results are an indication of that the same process is taking place on both positrode materials. However, the process might experience different limitations.

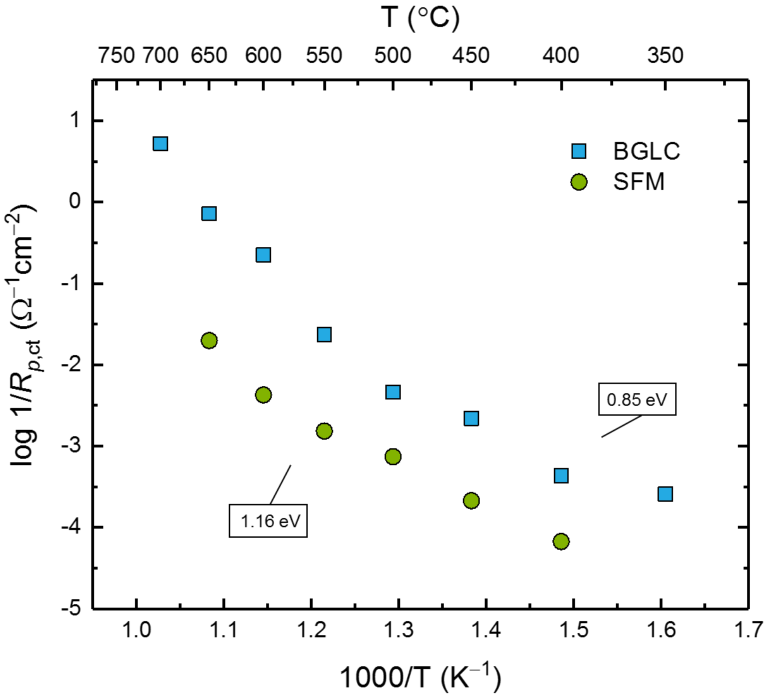

Figure 6.1 Comparison of the temperature dependency of the charge transfer resistance for BGLC and SFM. The measurements were carried out at OCV under wet air, i.e. pO_2 = 0.20 atm and pH_2O = 0.025 atm. The double layer capacitances varied from 10^{-8} to 10^{-5} Fcm^{-2}.

The pre-exponential factor for charge transfer was larger for BGLC than for SFM, as seen in Table 5.7 and 5.8, respectively. An increase in the number of active sites corresponds to a higher value of the pre-exponential factor, which indicates that SFM has fewer available sites for charge transfer to take place than BGLC. The significantly larger value of the pre-exponential factor for BGLC indicates that there are more active sites for the charge transfer reaction to occur at than at SFM positrode. This result is a strong indication of that BGLC enables “bulk path” for proton transport in contrast to SFM where the proton transport is restricted to the surface although both materials are mixed ionic-electronic conducting oxides.

The double layer capacitances (C_{dl}) changes with temperature. Whereas C_{dl} for BGLC (Figure 5.9) decreases with increasing temperature, C_{dl} for SFM exhibits an opposite trend (Figure 5.10). Rendering to Table 5.5, the C_{dl} values for BGLC and SFM are in order of ~10^{-5} and ~10^{-8} Fcm^{-2}, respectively, at intermediate to low temperatures. The higher capacitance value for BGLC is an indication of a larger reaction area for the charge transfer reaction and that it will most likely occur between the electrolyte and BGLC bulk. While for SFM, which does not exhibit proton conductivity, the smaller C_{dl} value implies that the reaction area for charge transfer is smaller, which is thus limited to occur across electrolyte bulk and TPB.

However, as the C_{dl} for both positrodes tend to fluctuate with temperature compared to the ohmic and mass transfer capacitances. The reason is that the charge transfer contribution, observed in the middle-frequency range, is partly overlapped with both the high and low-frequency responses. The distinctness of this particular contribution in the impedance spectra is, to some extent, dependent on the magnitude of the response for the two other contributions.

The *m*-values, i.e. $1/R_p \propto (pO_2)^m (pH_2O)^n$ for charge transfer resistance were close to zero for both positrodes, while the *n*-values varied between ¼ and ½ as displayed in Table 5.9 and 5.10 for BGLC and SFM, respectively. In some oxides, the proton concentration is minor and have a water vapour dependency of ½ (Equation 2.) However, a slight increase in $1/R_p$ with increasing pO_2 was observed at 650°C (only two points for SFM). The *m* and *n* values for both contributions will be further discussed in the following chapter, along with the reaction models.

Activation energies for the charge transfer reaction had the same order of magnitude for both positrode materials. The Arrhenius plots of charge transfer contributions in different pO_2 and pH_2O presented in Figure 5.23 and Figure 5.24, did not show any significant change in the activation energy. However, the pre-exponential values for SFM decreased with decreasing partial pressures of oxygen and water vapour.

6.3.2 Mass Transfer

The low-frequency response is associated with the mass transfer processes. The results from electrochemical measurements are evident on that these processes are slow and more receptive to the operating conditions, compared to the charge transfer, and, more complex, i.e. more involved species, in PCEC systems. The mass transfer contribution, response with capacitances values around 10^{-3} - 10^{-1} Fcm^{-2}, is strongly dependent on temperature, oxygen and water vapour partial pressure and properties of the positrode material. Processes such as gas adsorption/desorption, surface diffusion, surface exchange and redox of oxygen species may be involved in the mass transfer contribution.

In contrast to C_{dl}, the mass transfer capacitances (C_{mt}) did not fluctuate with temperature to the same extent, as shown in Figure 5.9 and 5.10 for BGLC and SFM, respectively. In principle, the surface kinetics is to some degree expected to be alike as both positrode materials are perovskite oxides with mixed ionic and electronic conductivities. The C_{mt} values for SFM were of the order of 10^{-1} Fcm^{-2}, larger than that for BGLC which increased from of order of 10^{-3} to 10^{-2} Fcm^{-2} at 350 - 700 °C, respectively, as presented in Table 5.5. The larger values of C_{mt} for SFM is possibly due to the almost 20 % porosity of the sintered pellets, as can be observed in Figure 5.3 and Table 5.3.

The temperature dependencies of the mass transfer resistances for BGLC and SFM are compared in Figure 6.2. BGLC exhibit a mass transfer R_p of about 5.3 kΩcm^2 at the lowest temperature (350 °C), which decreases to 0.4 Ωcm^2 at 700 °C, the highest temperature. For SFM, the R$_p$ values decrease from about 172 kΩcm^2 to 9 Ωcm^2 at 400 and 650 °C, respectively. These results are an indication of that for BGLC; the favoured reaction path varies with operating conditions.

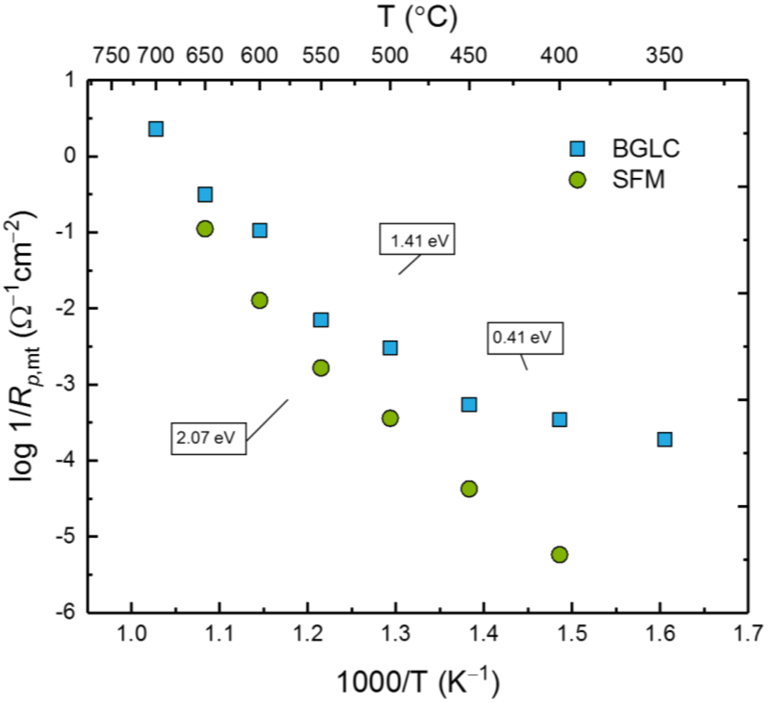

Figure 6.2 Temperature dependencies of mass transfer resistance for BGLC and SFM. The measurements were carried out at OCV under wet air, i.e. pO_2 = 0.20 atm and pH_2O = 0.025 atm. The capacitances varied from 10^{-3} to 10^{-1} Fcm^{-2}.

SFM exhibits activation energy of about 2 eV and a pre-exponential of order 10^8 for the mass transfer reaction, as presented in Table 5.8. The mass transfer activation energies and pre-exponentials at BGLC, on the other hand, vary with temperature. The overall activation energy is about 1.4 eV but increases from 0.4 eV at the low-temperature region to 2.5 eV at temperatures above 500 °C, the following pre-exponentials increases as well from ~10^{-1} to ~10^{13}, respectively. The activation energy is expected to increase with temperature due to activation of oxide ion transport. However, these values are orders of magnitude larger than that in literature [12, 53] The differing activation energies for mass transfer are indicative of different mechanisms. Likewise, the variation in the pre-exponential values may also point towards different processes dominating at different temperatures.

Along with the relatively small polarisation resistance and the low activation energy at low temperatures, BGLC point toward that it might have some bulk transport of protons [9]. SFM, however, seem to have the same mass transfer processes dominating in the whole measured temperature range. At temperatures below 400°C, the low-frequency resistance became so large that the impedance spectra reminded of a blocking electrode. The higher activation energies at increased temperatures can be due to contribution from electronic charge carriers (holes) resulting in increased conductivity of BZCY, which is observed at the highest pO_2 dependencies of the $1/R_{ohm}$.

The pO_2- and pH_2O-dependencies of mass transfer $1/R_p$, presented in Figure 5.17 and 5.21, respectively, are similar for BGLC and SFM. The *m*-values for mass transfer vary between ¼ and ⅛ for both materials. These reaction orders are associated with protonation of adsorbed oxygen species (¼) and a second proton exchange for water formation (⅛) [45].

The $1/R_{p,\mathrm{mt}}$ exhibits a negative pH_2O dependency, i.e. the mass transfer resistances under wet conditions are larger than that under dry conditions for both positrodes. The negative *n*-values, i.e. the increasing mass transfer resistance with increasing pH_2O, indicates that the electrode surface is saturated with protons (or hydroxide ions), hence making the oxygen adsorption more difficult. Also, when there are not dilute conditions, competitive adsorption between oxygen gas and water vapour may also occur. Given that assumption, one water molecule can occupy more than one active site on the oxide surface. Furthermore, the mass transfer resistance increases with decreasing pO_2. Although the pO_2 dependency is the opposite of the pH_2O dependency, it endorses the assumption of oxygen species being limited by water molecules on the surface.

The polarisation resistances in varying partial pressures were further investigated as a function of temperature, the plots are presented in Figure 5.23 and 5.24 for the charge transfer and in Figure 5.25 and 5.26 for the mass transfer $1/R_p$. It is worthy of note that different atmospheres yield the same temperature dependency for both systems. Although the activation energies did not vary in different partial pressures, the positrode performance appeared to reduce with decreasing pO_2 as the polarisation resistances increased.

6.4 Positrode Reaction Models and Kinetics

One of the main objectives of this work is to develop a reaction model describing the positrode reaction mechanism. In the following, two reaction models are developed based on the experimental results with consideration to the properties of the materials. The positrode reaction model, presented as a series of elementary reaction steps, is an assembly of several processes taking place simultaneously and where each can be given a particular reaction order concerning the activity of the involved gases. The reaction path depends on several factors such as involved species, physical and chemical properties of the material, the partial pressure and temperature. Moreover, the rate of the overall positrode reaction depends on the rate of the slowest reaction step, known as the rate-determining step (RDS).

All electrode processes are not chemical reactions; however, they may still be limited due to other actions such as diffusion, and thus affect the overall reaction rate. Rate of a reaction that occurs in a sequence of steps gives an insight into the atomic processes proceeding when the reaction takes place. Many of the more straightforward steps are often combined in the reaction models. Figure 6.3 displays a schematic representation of elementary steps that are expected to take place at the electrolyte/electrode interface and the electrode surface. Unlike the reaction steps found in the literature [71], the diffusion of adsorbed oxygen species is absent here. It follows that as the electrode surface appeared to be saturated by hydroxide ions or water, the transport of protons will be more favourable than the diffusion of adsorbed oxide or hydroxide ions.

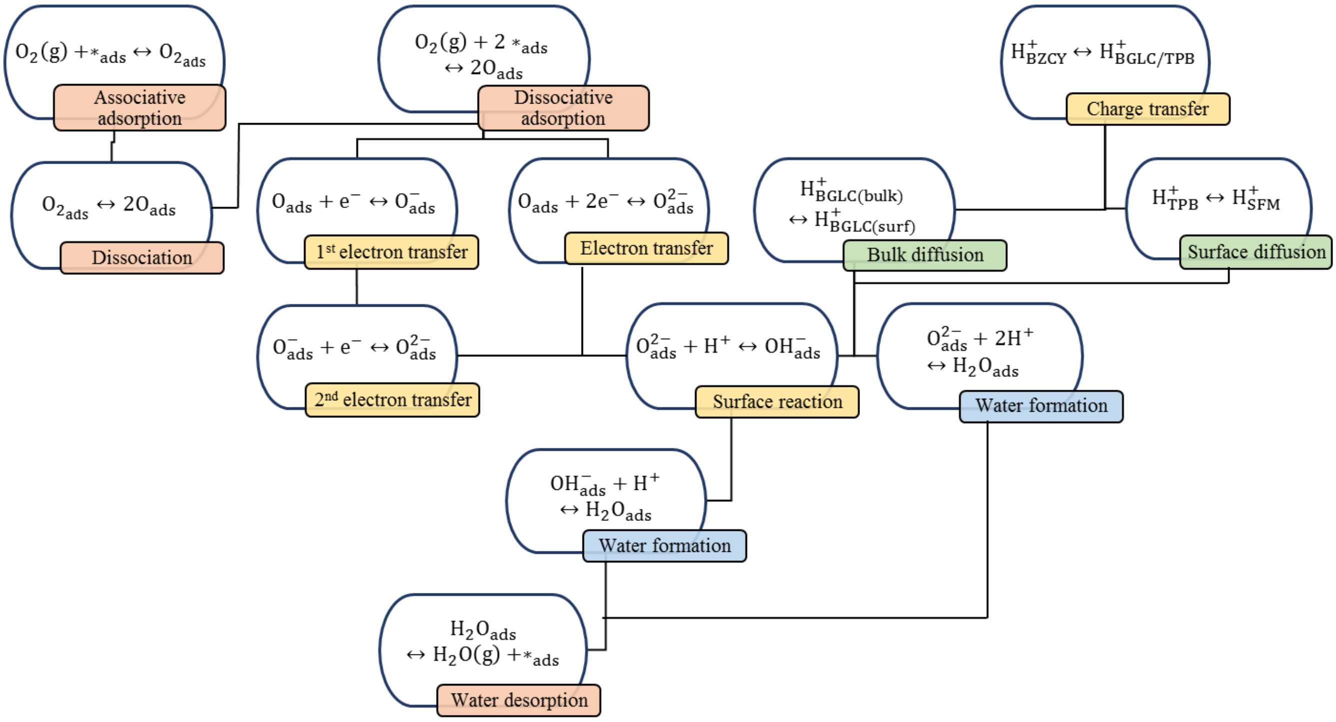
$O_2(g) + *_{ads} \leftrightarrow O_{2ads}$
Associative adsorption
$O_2(g) + 2 *_{ads} \leftrightarrow 2O_{ads}$
Dissociative adsorption
$H^+_{BZCY} \leftrightarrow H^+_{BGLC/TPB}$
Charge transfer
$O_{2ads} \leftrightarrow 2O_{ads}$
Dissociation
$O_{ads} + e^- \leftrightarrow O^-_{ads}$
1st electron transfer
$O_{ads} + 2e^- \leftrightarrow O^{2-}_{ads}$
Electron transfer
$H^+_{BGLC(bulk)} \leftrightarrow H^+_{BGLC(surf)}$
Bulk diffusion
$H^+_{TPB} \leftrightarrow H^+_{SFM}$
Surface diffusion
$O^-_{ads} + e^- \leftrightarrow O^{2-}_{ads}$
2nd electron transfer
$O^{2-}_{ads} + H^+ \leftrightarrow OH^-_{ads}$
Surface reaction
$O^{2-}_{ads} + 2H^+ \leftrightarrow H_2O_{ads}$
Water formation
$OH^-_{ads} + H^+ \leftrightarrow H_2O_{ads}$
Water formation
$H_2O_{ads} \leftrightarrow H_2O(g) + *_{ads}$
Water desorption

Figure 6.3 An extensive reaction model for the positrode reaction. There are several possible pathways for the positrode reaction. Some processes are fast and therefore, often combined. Reaction steps or the processes on the same level take place simultaneously. One or more steps may be limiting, i.e. the "bottleneck", depending on the materials and operating conditions.

The reaction models available in the literature are based on elementary steps for the SOFC cathode, which only includes redox of oxygen [2, 78]. Such reaction models, as presented in Table 3.2, show a common reaction mechanism for PCFC cathode with mixed O^{2-}/e^- conductivity (O-MIEC) [2], the first four steps are the same as for SOFC and steps 5-8 are characteristics for PCFC. With these types of the electrode, the reaction will be restricted to the triple phase boundary (TPB). In the SOFC equivalent steps, oxygen ions diffuse from the electrode surface to the TPB, where they react with protons from the electrolyte. This assumption is based on one of the first studies on PCFC cathode reaction by Uchida et al. [71] where a platinum electrode was used as the cathode. The activation energy of approximately 0.99 eV was associated with the surface diffusion of adsorbed oxygen species on Pt electrode, which was suggested as the rate-determining step. However, at low temperatures and under wet conditions, BGLC exhibit proton transport [12].

Reaction model 1 is developed for BGLC. In the case of a mixed H^+/e^- conductor (MPEC), such as BGLC, the reaction mechanism is different from those based on SOFC, because the protons from the electrolyte can migrate through the electrode bulk, which will activate the whole electrode surface.

Reaction model 2 is developed for SFM as a positrode for PCECs. Although SFM is a mixed O^{2-}/e^- conductor, the reaction mechanism will be different from the ones found in the literature. In contrast to SOFC cathode reaction, the water formation takes place at the PCFC cathode; hence, the water containing atmosphere impacts on the mechanism. The negative $p\mathrm{H_2O}$ dependencies of $1/R_{mt}$ indicate that protons take a more significant part in the positrode reaction and participates earlier in the mechanism than those suggested in the literature. Furthermore, the reaction is not necessarily restricted to occur at the TPB, however, the diffusion of adsorbed oxygen species is most likely too slow compared transport of protons from the electrolyte/TPB to the adsorbed oxygen at the electrode surface.

These models elucidate the key trends of the reaction mechanism based on the findings in this work and are not a description of the details.

6.4.1 Elementary Reactions and Rate-Determining Step

With the aim of further analysis of the reaction processes and kinetics, the partial pressure dependencies of the polarisation resistance need to be addressed. These are suitable parameters to evaluate the performance of an electrode and to determine the RDS.

The reaction orders m and n found experimentally, are dependent on the type of species involved in the rate-limiting steps at the electrode.

Both positrode materials are measured under the same conditions and with the same state-of-the-art proton conducting electrolyte, BZCY. The m and n values are calculated using Butler-Volmer (B-V) theory, Nernst equation and Langmuir isotherm. All reaction steps, except the RDS, which sources the overpotential, are assumed to be in virtual equilibrium. Whereas the Nernst equation shows the relationship between the potential and the concentration of species involved in the electrochemical reaction at equilibrium, the B-V equation describes this relation when the system is not at equilibrium.

The reaction steps before the charge transfer can be divided into associative adsorption followed by dissociation of oxygen or dissociative adsorption. The electron transfer step may also be split into two steps with the diffusion of singular charged oxide ions in between. These steps are common in literature for both SOFC and PCFC [69, 72].

In both reaction models, each reaction step is presented with the corresponding theoretical reaction orders, i.e. m and n values related to $p\mathrm{O_2}$ and $p\mathrm{H_2O}$ dependencies, respectively. The following reaction rate expressions for each step used to calculate the m and n values are given for each model.

Reaction Model 1 – Bulk Path

The "bulk path" model, illustrated in Figure 6.4, is developed for BGLC. Considering the protonic conductivity of the MPEC, it is assumed that the charge transfer occurs across the electrolyte and the electrode, whereas the proton diffuses through BGLC bulk. The entire surface area is activated, given that oxygen gas is adsorbed and reduced (ionised) on the surface.

Table 6.1 Reaction model 1 – "Bulk path". Based on BGLC as positrode. The *m* and *n* values are the reaction orders if the reaction is rate determining. The numbers in the last column are multiplication factors for each step, i.e. the number of times each step has to occurs to get the total reaction.

Step	**Elementary reaction**	**Process**	***m***	***n***	
1	$O_2(g) + 2^*_{BGLC} \leftrightarrow 2O_{BGLC(ads)}$	Exchange of oxygen gas	1	0	× *1*
2	$O_{BGLC(ads)} + 2e^- \leftrightarrow O^{2-}_{BGLC(ads)}$	Electron transfer	½	0	× *2*
3	$H^+_{BZCY} \leftrightarrow H^+_{BGLC(bulk)}$	Charge transfer	0	¼	× *4*
3a	$H^+_{BGLC(bulk)} \leftrightarrow H^+_{BGLC(surf)}$	*Bulk diffusion of protons*	--	--	
4	$O^{2-}_{BGLC(ads)} + H^+_{BGLC(surf)} \leftrightarrow OH^-_{BGLC(ads)}$	Proton exchange	¼	½	× *2*
5	$OH^-_{BGLC(ads)} + H^+_{BGLC(surf)} \leftrightarrow H_2O_{BGLC(ads)}$	Water formation/split	0	1	× *2*
6	$H_2O_{BGLC(ads)} \leftrightarrow H_2O(g) + {}^*_{BGLC}$	Exchange of water vapour	0	1	× *2*
Total reaction: $O_2(g) + 2^*_{BGLC} + 4e^- + 4H^+ \rightleftarrows 2H_2O(g) + 2^*_{BGLC}$					

The corresponding reaction rate equations of the proposed reaction model are:

$$r_1 = k_1^+ pO_2(1 - \Theta_{BGLC})^2 - k_1^- \Theta^2_{O_{BGLC}} \tag{6.1}$$

$$r_2 = k_2^+ \Theta_{O_{BGLC}} - k_2^- \Theta_{O^{2-}_{BGLC}} \tag{6.2}$$

$$r_3 = k_3^+ a_{H^+_{BZCY}} \exp\left(-\frac{F\eta_{ct}}{2RT}\right) - k_3^- a_{H^+_{BGLC(bulk)}} \exp\left(\frac{F\eta_{ct}}{2RT}\right) \tag{6.3}$$

$$r_4 = k_4^+ \Theta_{O^{2-}_{BGLC}} a_{H^+_{BGLC(surf)}} - k_4^- \Theta_{OH^-_{BGLC}} \tag{6.4}$$

$$r_5 = k_5^+ \Theta_{OH^-_{BGLC}} a_{H^+_{BGLC(surf)}} - k_5^- \Theta_{H_2O_{BGLC}} \tag{6.5}$$

$$r_6 = k_6^+ \Theta_{H_2O_{BGLC}} - k_6^- pH_2O \tag{6.6}$$

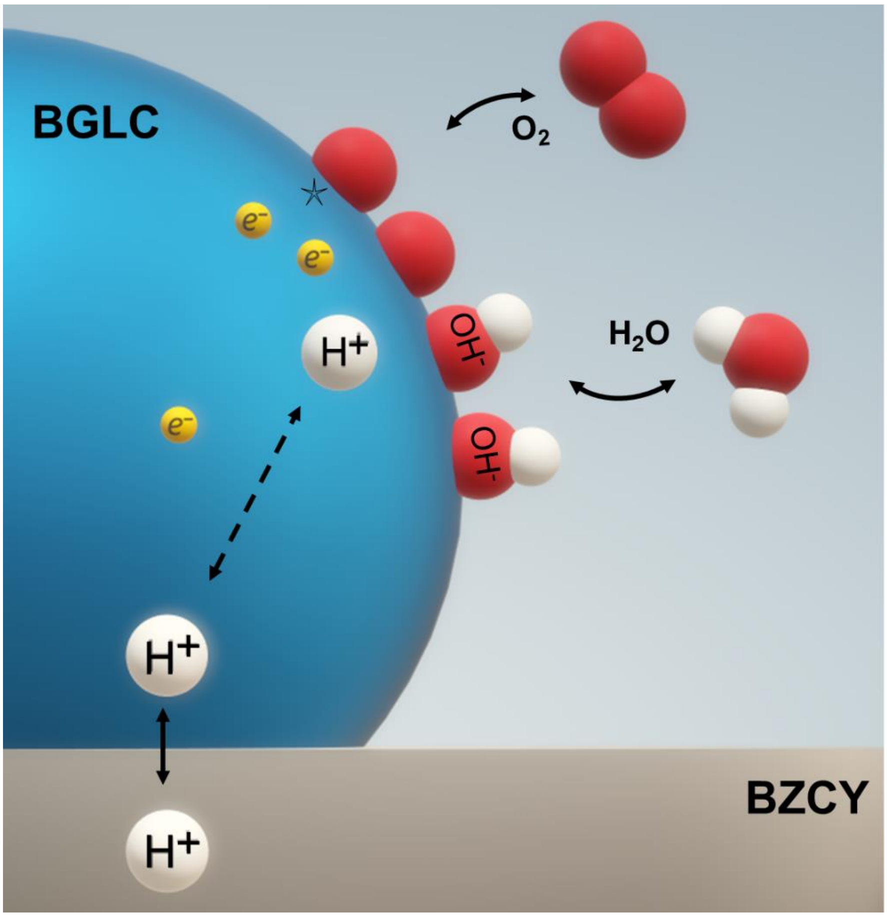

Figure 6.4 Graphics representation of reaction model 1, illustrating the "bulk-path" of protons through BGLC positrode. The charge transfer occurs across BZCY/BGLC interface; protons diffuse through the electrode bulk to the surface.

Reaction Model 2 – Surface Path

Figure 6.5 illustrates the "surface path" model. This reaction model is based on the SFM positrode, which does not exhibit protonic conductivity. Thus, the reaction is utterly restricted to the TPB or the electrode surface.

Table 6.2 Reaction model 2 – "Surface path". Based on SMF as positrode. Note that there is a difference between species with the subscript "SFM (ads)", which means adsorbed species on the electrode surface, and "SFM (surf)" meaning the species are not adsorbed, i.e. does not occupy adsorption sites on the surface. The numbers in the last column are multiplication factors for each step, i.e. the number of times each step has to occurs to get the total reaction.

Step	**Elementary reaction**	**Process**	***m***	***n***	
1	$\mathrm{O_2(g) + 2^*_{SFM} \leftrightarrow 2O_{SFM(ads)}}$	Exchange of oxygen gas	1	0	× *1*
2	$\mathrm{O_{SFM(ads)} + 2e^- \leftrightarrow O^{2-}_{SFM(ads)}}$	Electron transfer	½	0	× *2*
3	$\mathrm{H^+_{BZCY} \leftrightarrow H^+_{TPB}}$	Charge transfer	0	¼	× *4*
3a	$OH^-_{TPB/SFM} \leftrightarrow H^+_{SFM(surf)} + O^{2-}_{SFM(surf)}$	*Surface transport of protons*	--	--	
4	$\mathrm{H^+_{SFM(surf)} + O^{2-}_{SFM(ads)} \leftrightarrow OH^-_{SFM(ads)}}$	Proton exchange	¼	½	× *2*
5	$\mathrm{OH^-_{SFM(ads)} + H^+_{SFM(surf)} \leftrightarrow H_2O_{SFM(ads)}}$	Water formation/split	0	1	× *2*
6	$\mathrm{H_2O_{SFM(ads)} \leftrightarrow H_2O(g) + {}^*_{SFM}}$	Exchange of water vapour	0	1	× *2*

Total reaction: $\mathbf{O_2(g) + 2^*_{SFM} + 4e^- + 4H^+ \rightleftarrows 2H_2O(g) + 2^*_{SFM}}$

The corresponding reaction rate equations of the proposed reaction model are:

$$\mathrm{r_1 = k_1^+}p\mathrm{O_2 - k_1^- \Theta^2_{O_{SFM}}} \tag{6.7}$$

$$\mathrm{r_2 = k_2^+ \Theta_{O_{SFM}} - k_2^- \Theta_{O^{2-}_{SFM}}} \tag{6.8}$$

$$\mathrm{r_3 = k_3^+} a_{\mathrm{H^+_{BZCY}}} \mathrm{exp}\left(-\frac{\mathrm{F\eta_{ct}}}{\mathrm{2RT}}\right) - \mathrm{k_3^-} a_{\mathrm{H^+_{TPB}}} \mathrm{exp}\left(\frac{\mathrm{F\eta_{ct}}}{\mathrm{2RT}}\right) \tag{6.9}$$

$$\mathrm{r_4 = k_4^+ \Theta_{O^{2-}_{SFM}}} a_{\mathrm{H^+_{SFM(surf)}}} - \mathrm{k_4^- \Theta_{OH^-_{SFM}}} \tag{6.10}$$

$$\mathrm{r_5 = k_5^+ \Theta_{OH^-_{SFM}}} a_{\mathrm{H^+_{SFM(surf)}}} - \mathrm{k_5^- \Theta_{H_2O_{SFM}}} \tag{6.11}$$

$$\mathrm{r_6 = k_6^+ \Theta_{H_2O_{SFM}} - k_6^-}p\mathrm{H_2O} \tag{6.12}$$

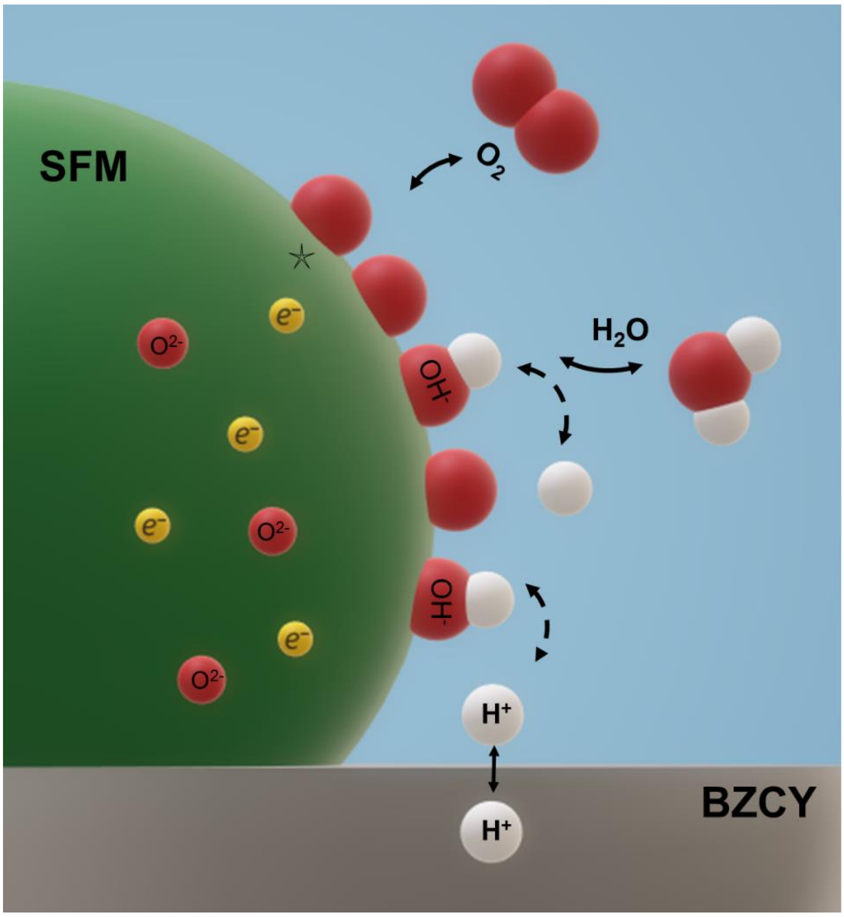

Figure 6.5 Graphic representation of reaction model 2 illustrating the "surface-path" of protons on SFM positrode, which does not exhibit protonic conductivity. The charge transfer occurs across BZCY/TPB; protons migrate on the electrode surface.

Comparison and Interpretation of the Reaction Models

The following discussion and interpretations of the elementary reaction are described in PCFC direction.

In principle, both reaction models exhibit the same mechanism, and the theoretical reaction orders are thus equivalent. The surface reactions are, as discussed above, expected to be similar on both oxides. However, since BGLC exhibit proton transport at low temperatures in a water-rich atmosphere [12], the charge transfer reaction occurs across BZCY and BGLC bulk, as illustrated in Figure 6.4. In contrast, SFM is mainly a *p*-type electronic conductor under the tested conditions and may have a minor contribution of the ionic charge carriers, oxide ions, at high temperatures [39]. Consequently, the charge transfer reaction in Model 2, demonstrated in Figure 6.5, occur across BZCY and TPB. The higher value of the C_{dl} along with the greater charge transfer pre-exponential factor for BGLC, which are indicative of a larger reaction area and more active reaction sites, respectively, supports these suggestions.

Dissociative adsorption of oxygen gas is suggested as **Step 1** in both models, which have a pO_2-dependency of order 1 and no pH_2O-dependency. The following reaction rate, Equation 6.1 and 6.7, is expressed in terms of om Langmuir isotherm. However, it is assumed that it is dilute conditions, and there are thus always sufficient vacant adsorption sites. Therefore, Θ is not treated as a limiting factor in the following steps. Consequently, the first step is not considered as RDS.

Reaction **Step 2** yields a double electron transfer reaction. In general, the rate expressions for steps involving electron transfer includes an exponential term based on the Butler-Volmer theory, relating the overpotential with current density. However, for gas/solid reactions, the electric potential at the surface is not equal to the overpotential for charge transfer across the phase boundary and since both negative charges (e^-) are located at the same place no potential differences arise, i.e. no charge gradient. Because of that, an applied potential will not change the electric potential at the surface of the oxide, and the reaction is not affected by changes in the Nernst potential. Therefore, the reaction rate expression for this step does not include an exponential term. Also, the reaction step is not dependent on pH_2O, but have a pO_2 dependency of order ½.

Although reaction **Step 3**, the charge transfer reaction, is different for the two models, as discussed above, both reaction rate expressions (Equations 6.3 and 6.9) contains the exponential term comprising the overpotential, as defined under section 2.3.2. The overpotential stems from the charge transfer reaction and affects the rates of the other reaction steps through, e.g. concentration limitations. The overpotential observed for mass transfer is also originated from the charge transfer process since both resistances are coupled in series, they experience the same current, i.e. have the same rate. The magnitude of this current is commonly limited by the sluggishness of one or more rate-limiting steps. Moreover, the current density is driven by a certain overpotential, which is the sum of all reactions and observed as the polarisation resistance [79].

The transport process of protons in step 3a, followed by the charge transfer reaction, is not a chemical reaction but rather a physical displacement and is thus not affected by any changes in the potential. Although the process does not take a reaction rate expression, the process can still contribute to the total reaction rate due to, e.g. concentration limitations.

Reaction **Step 4**, which comprise the proton exchange, have both pO_2 and pH_2O dependency of ¼ and ½, respectively. Whether the proton diffuses along the electrode surface or migrates through the bulk, the reaction seems to be limited by the proton exchange, the, i.e. reaction of a proton with the adsorbed oxide ions. As presented in Table 5.9 and 5.10, the *m* values for the mass transfer are for the most part ¼ while the *n* values are negative and varies from -¼ to -½ for both positrode materials. A negative pH_2O dependency can mean that protons do not participate before or in the RDS [45].

Reaction **Step 5** and **Step 6**, formation and desorption of water, have the same theoretical pH_2O dependency. The last step is analogous to the first, with the same following partial pressure dependency.

Determining the RDS

Based on the similar reaction models, the calculated *m* and *n* values for each step, if rate-determining, are also equal. The mathematical analysis, along with the analyses of the experimental results suggest that the RDS is the proton exchange, precisely the reaction of protons and adsorbed oxide ions to form hydroxides. According to Poetzsch et al. the experimental *m*-values for mass transfer suggests that the protonation of adsorbed oxygen and the proton exchange reaction to form water, step 4 and 5 respectively, are the RDS [45].

The negative *n*-values are a strong indication of that there were not dilute conditions in any of the measured systems. The surfaces appear to be saturated with OH^-/H_2O. Given that, the calculated reaction orders for pH_2O-dependency do not yield information about the RDS.

There are also other factors that influence the performance of the performance. The resistances for BGLC are much lower than that for SFM, which mean that BGLC is a better positrode. While the $R_{p,\,mt}$ values for at SFM keeps increasing with decreasing temperatures, they seem to be more even for BGLC, which indicates that another process is taking over.

Figure 6.6 represents a model, which relates the current and voltage in a Butler-Volmer for the charge transfer and mass transfer process at both positrodes. The current distribution can provide information about mass transfer limitations in the regime where diffusion or adsorption is the RDS. The mass transfer overpotential is a sum of the total voltage output.

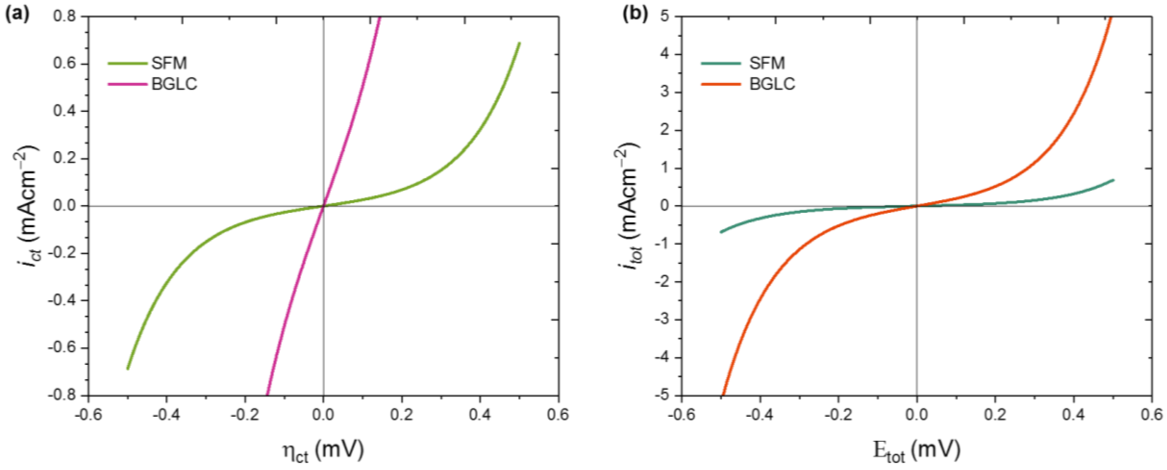

Figure 6.6 Butler-Volmer plots constructed from the calculated values of i_0 from (a) charge transfer resistances and (b) total R_p, (R_{ct} + R_{mt}) at 500°C for BGLC and SFM. The current-voltage relation can be expressed as mass transfer limitations in the regime where diffusion or adsorption is the RDS.

6.4.2 Further Work

The present work has examined the various aspects of the performance of the positrodes for proton ceramic electrochemical cells. BGLC is obviously the best candidate for positrode material in PCECs as it has the flexibility to change reaction paths concurring to the operating conditions. As several results were indicative of proton transport through BGLC bulk at lower temperatures, a natural continuation of the work is to the investigation of conductivities and transference numbers of the charge carriers. More importantly, however, is a thorough characterisation of the mass transfer limitations at the surface. The EIS measurements with positive DC bias (Figure 5.23) showed that the polarisation resistance decreased with a higher value of the applied potential. Further investigation on this manner with DC bias applied in both directions will provide more information about the charge transfer reaction and the overpotentials.

7 Conclusions

In the present work, performance and kinetics of $BaGd_{0.8}La_{0.2}Co_2O_{6-\delta}$ and $SrFe_{0.75}Mo_{0.25}O_{3-\delta}$ as PCECs positrodes have been thoroughly studied. SFM was synthesised by solid-state reaction, while a supplier delivered powder of BGLC. Both materials were pressed to pellets and sintered to density above 80 %. EDS and XRD analysis revealed secondary phases containing cubic cobalt oxide on the BGLC surface. SFM is a perovskite oxide that exhibits mixed ionic (O^{2-}) and electronic conductivity (O-MIEC). BGLC is a double perovskite with mixed ionic (protonic) and electronic conductivity (MPEC).

A model electrode with point contact was made by placing the dense positrode pellet vertically on the state-of-the-art proton ceramic BZCY button electrolyte with counter and reference electrodes of Pt. Electrochemical impedance measurements under controlled atmospheres and varying temperatures were successfully carried out for both systems.

The charge transfer polarisation resistance for SFM was about 15 kΩcm^2 at 400 °C, more than six times larger than that for BGLC, which exhibited 2.3 kΩcm^2, at the same temperature. At 650 °C the $R_{p,\mathrm{ct}}$ value was decreased to 1.4 Ωcm^2 for BGLC, while for SFM, the value was about 50.4 Ωcm^2. The corresponding double layer capacitances, C_{dl}, for BGLC and SFM were in the order of ~10^{-5} and ~10^{-8} Fcm^{-2}, respectively, at intermediate to low temperatures.

Furthermore, the charge transfer reaction did not show any significant pO_2 dependency in any of the tested systems. There was, however, a pH_2O-dependency with reaction order between ¼ and ½. The mass transfer resistances also increased with decreasing pO_2. On the other hand, the mass transfer 1/R_p exhibited a negative pH_2O dependency, i.e. the mass transfer resistances under wet conditions were larger than that under dry conditions for both positrodes.

BGLC exhibited a mass transfer R_p of about 5.3 kΩcm^2 at the lowest measured temperature (350 °C), which decreased to 0.4 Ωcm^2 at 700 °C, the highest measured temperature. For SFM, the R_p values decrease from about 172 kΩcm^2 to 9 Ωcm^2 at 400 and 650 °C, respectively. Whereas $R_{p,\mathrm{mt}}$ for SFM yield a continuously linear increase with decreasing temperatures, BGLC exhibited different linearity at lower temperatures.

Based on the electrochemical measurements and with the consideration of the different properties of BGLC and SFM, two reaction models describing the positrode reaction mechanism was developed. Both reaction models are in principle similar. The differences in the two systems are related to the ionic charge carriers in and on the positrode materials. The differences in the pre-exponential factors for the charge transfer process at the BGLC and SFM was indicative of that BGLC enables a bulk path for proton transport. However, the dominating charge carriers in BGLC seems to vary with temperature as the activation energies showed a definite change from high to the low-temperature regime. At lower temperatures, the activation energy for BGLC of 0.4 eV signifies that the dominating charge carriers are protons, while at high temperatures, the activation energy exceeds 2.5 eV. The activation energy is expected to increase with increasing temperature as the transport of oxide ions is thermally activated.

However, the high-temperature activation energy was higher than what is found in the literature and may be caused by a combination of several processes co-occurring, which are difficult to distinguish by electrochemical impedance measurements or deconvolution. The partial pressure dependencies suggest that the overpotential stems from the charge transfer process at the interface of BZCY electrolyte and BGLC bulk or TPB.

The theoretical reaction rate models assume an abundance of adsorption sites on the surface, though the experimental results revealed that ambient water has a negative effect on the reaction rate. The surfaces appear to be saturated with OH^-/H_2O.

The proton transport through bulk seems to take place only at low temperatures.

The overpotential stems from the charge transfer reaction and the observed overpotential for mass transfer is due to the concentration differences caused by the $\eta_{ct.}$ A model, which relates the current and voltage in a Butler-Volmer manner, was developed. The current-voltage can be expressed as mass transport limited in a regime where diffusion or adsorption is rate-limiting steps.

The reaction between adsorbed oxide ion and proton appeared to be the RDS for both positrode materials.

This work on the positrode reaction kinetics has contributed to a new understanding of the overpotential originated from the charge transfer reaction and, moreover, the relation to the mass transfer limitations.

Lastly, this work is a decent contribution to the development of the-state-of-the-art positrode BGLC, which is a promising candidate for future technologies such as water electrolysis for hydrogen production and intermediate temperature fuel cells.

Bibliography

1. Crabtree, G.W., M.S. Dresselhaus, and M.V. Buchanan, *The hydrogen economy.* Physics today, 2004. **57**(12): p. 39-44.
2. He, F., et al., *Cathode reaction models and performance analysis of Sm0.5Sr0.5CoO3−δ–BaCe0.8Sm0.2O3−δ composite cathode for solid oxide fuel cells with proton conducting electrolyte.* Journal of Power Sources, 2009. **194**(1): p. 263-268.
3. Serra, J.M., *Electrifying chemistry with protonic cells.* Nature Energy, 2019. **4**(3): p. 178-179.
4. Bi, L., S. Boulfrad, and E. Traversa, *Steam electrolysis by solid oxide electrolysis cells (SOECs) with proton-conducting oxides.* Chemical Society Reviews, 2014. **43**(24): p. 8255-8270.
5. Shim, J.H., *Ceramics breakthrough.* Nature Energy, 2018. **3**(3): p. 168-169.
6. Duan, C., et al., *Readily processed protonic ceramic fuel cells with high performance at low temperatures.* Science, 2015. **349**(6254): p. 1321-6.
7. Lo Faro, M., et al., *Fuel flexibility: A key challenge for SOFC technology.* Fuel, 2012. **102**: p. 554-559.
8. Fabbri, E., D. Pergolesi, and E. Traversa, *Materials challenges toward proton-conducting oxide fuel cells: a critical review.* Chemical Society Reviews, 2010. **39**(11): p. 4355-4369.
9. Kreuer, K.D., *Proton-Conducting Oxides.* Annual Review of Materials Research, 2003. **33**(1): p. 333-359.
10. Dubois, A., S. Ricote, and R.J. Braun, *Benchmarking the expected stack manufacturing cost of next generation, intermediate-temperature protonic ceramic fuel cells with solid oxide fuel cell technology.* Journal of Power Sources, 2017. **369**(Supplement C): p. 65-77.
11. Choi, S., et al., *Exceptional power density and stability at intermediate temperatures in protonic ceramic fuel cells.* Nature Energy, 2018. **3**(3): p. 202-210.
12. Strandbakke, R., et al., *Gd- and Pr-based double perovskite cobaltites as oxygen electrodes for proton ceramic fuel cells and electrolyser cells.* Solid State Ionics, 2015. **278**: p. 120-132.
13. Vøllestad, E., et al., *Mixed proton and electron conducting double perovskite anodes for stable and efficient tubular proton ceramic electrolysers*, in *Nature Materials*. 2019.
14. Vøllestad, E., et al., *Relating defect chemistry and electronic transport in the double perovskite Ba1−xGd0.8La0.2+xCo2O6−δ (BGLC).* Journal of Materials Chemistry A, 2017. **5**(30): p. 15743-15751.
15. Strandbakke, R., et al., *Ba0. 5Gd0. 8La0. 7Co2O6-δ Infiltrated in Porous BaZr0. 7Ce0. 2Y0. 1O3 Backbones as Electrode Material for Proton Ceramic Electrolytes.* Journal of The Electrochemical Society, 2017. **164**(4): p. F196-F202.
16. Fernández-Ropero, A.J., et al., *High valence transition metal doped strontium ferrites for electrode materials in symmetrical SOFCs.* Journal of Power Sources, 2014. **249**: p. 405-413.
17. Chen, W.-T., et al., *Ligand-hole localization in oxides with unusual valence Fe.* Scientific Reports, 2012. **2**: p. 449.
18. Irvine, J.T., D.C. Sinclair, and A.R. West, *Electroceramics: characterization by impedance spectroscopy.* Advanced Materials, 1990. **2**(3): p. 132-138.

19. Stambouli, A.B. and E. Traversa, *Solid oxide fuel cells (SOFCs): a review of an environmentally clean and efficient source of energy.* Renewable and Sustainable Energy Reviews, 2002. **6**(5): p. 433-455.
20. Adler, S.B., *Factors Governing Oxygen Reduction in Solid Oxide Fuel Cell Cathodes.* Chemical Reviews, 2004. **104**(10): p. 4791-4844.
21. Matsuzaki, Y., et al., *Effect of proton-conduction in electrolyte on electric efficiency of multi-stage solid oxide fuel cells.* Scientific Reports, 2015. **5**: p. 12640.
22. Song, C., *Fuel processing for low-temperature and high-temperature fuel cells: Challenges, and opportunities for sustainable development in the 21st century.* Catalysis Today, 2002. **77**(1): p. 17-49.
23. Adams, T.A., et al., *Energy Conversion with Solid Oxide Fuel Cell Systems: A Review of Concepts and Outlooks for the Short- and Long-Term.* Industrial & Engineering Chemistry Research, 2013. **52**(9): p. 3089-3111.
24. Fabbri, E., D. Pergolesi, and E. Traversa, *Electrode materials: a challenge for the exploitation of protonic solid oxide fuel cells.* Science and Technology of Advanced Materials, 2010. **11**(4): p. 044301.
25. Norby, T. and Y. Larring, *Concentration and transport of protons in oxides.* Current Opinion in Solid State and Materials Science, 1997. **2**(5): p. 593-599.
26. Kreuer, K.D., *On the development of proton conducting materials for technological applications.* Solid State Ionics, 1997. **97**(1): p. 1-15.
27. Iwahara, H., et al., *Proton conduction in sintered oxides and its application to steam electrolysis for hydrogen production.* Solid State Ionics, 1981. **3-4**: p. 359-363.
28. Iwahara, H., H. Uchida, and N. Maeda, *High temperature fuel and steam electrolysis cells using proton conductive solid electrolytes.* Journal of Power Sources, 1982. **7**(3): p. 293-301.
29. Iwahara, H., *High temperature proton conducting oxides and their applications to solid electrolyte fuel cells and steam electrolyzer for hydrogen production.* Solid State Ionics, 1988. **28-30**: p. 573-578.
30. Iwahara, H., *Oxide-ionic and protonic conductors based on perovskite-type oxides and their possible applications.* Solid State Ionics, 1992. **52**(1): p. 99-104.
31. Iwahara, H., T. Yajima, and H. Ushida, *Effect of ionic radii of dopants on mixed ionic conduction (H++O2-) in BaCeO3-based electrolytes.* Solid State Ionics, 1994. **70-71**(PART 1): p. 267-271.
32. Bonanos, N., K.S. Knight, and B. Ellis, *Perovskite solid electrolytes: Structure, transport properties and fuel cell applications.* Solid State Ionics, 1995. **79**: p. 161-170.
33. Katahira, K., et al., *Protonic conduction in Zr-substituted BaCeO3.* Solid State Ionics, 2000. **138**(1): p. 91-98.
34. Dubal, S.U., et al., *Proton conducting BaCe0.7Zr0.1Y0.2O2.9 thin films by spray deposition for solid oxide fuel cell.* Applied Surface Science, 2015. **324**: p. 871-876.
35. Fabbri, E., et al., *Tailoring the chemical stability of Ba(Ce0.8−xZrx)Y0.2O3−δ protonic conductors for Intermediate Temperature Solid Oxide Fuel Cells (IT-SOFCs).* Solid State Ionics, 2008. **179**(15): p. 558-564.
36. Yoo, Y. and N. Lim, *Performance and stability of proton conducting solid oxide fuel cells based on yttrium-doped barium cerate-zirconate thin-film electrolyte.* Journal of Power Sources, 2013. **229**: p. 48-57.
37. Richter, J., et al., *Materials design for perovskite SOFC cathodes.* Monatshefte für Chemie - Chemical Monthly, 2009. **140**(9): p. 985-999.
38. Yamaura, H., et al., *Cathodic polarization of strontium-doped lanthanum ferrite in proton-conducting solid oxide fuel cell.* Solid State Ionics, 2005. **176**(3): p. 269-274.

39. Liu, Q., et al., *A Novel Electrode Material for Symmetrical SOFCs.* Advanced Materials, 2010. **22**(48): p. 5478-5482.
40. Tao, S.W., et al., *Electrode materials for intermediate temperature proton-conducting fuel cells.* Journal of Applied Electrochemistry, 2000. **30**(2): p. 153-157.
41. Dailly, J., et al., *Perovskite and A2MO4-type oxides as new cathode materials for protonic solid oxide fuel cells.* Electrochimica Acta, 2010. **55**(20): p. 5847-5853.
42. Singh, K., A.K. Baral, and V. Thangadurai, *Electrochemical studies of Gd0.5Pr0.5BaCo2O5+δ (GPBC) cathode for oxide ion and proton conducting solid oxide fuel cells.* Solid State Ionics, 2016. **288**: p. 351 - 356.
43. Batocchi, P., et al., *Electrical and electrochemical properties of architectured electrodes based on perovskite and A2MO4-type oxides for Protonic Ceramic Fuel Cell.* Electrochimica Acta, 2014. **145**: p. 1 - 10.
44. Fan, L. and P.-C. Su, *Layer-structured LiNi0.8Co0.2O2: A new triple (H+/O2−/e−) conducting cathode for low temperature proton conducting solid oxide fuel cells.* Journal of Power Sources, 2016. **306**: p. 369-377.
45. Poetzsch, D., R. Merkle, and J. Maier, *Oxygen Reduction at Dense Thin-Film Microelectrodes on a Proton-Conducting Electrolyte I. Considerations on Reaction Mechanism and Electronic Leakage Effects.* J. Electrochem. Soc., 2015. **162**(9): p. F939-F950.
46. Sun, C., R. Hui, and J. Roller, *Cathode materials for solid oxide fuel cells: a review.* Journal of Solid State Electrochemistry, 2010. **14**(7): p. 1125-1144.
47. Meng, J., et al., *SrFe0.8Mo0.2O3-δ: Cathode material for intermediate temperature solid oxide fuel cells.* Solid State Ionics, 2014. **260**: p. 43-48.
48. Meng, X., et al., *Symmetrical solid oxide fuel cells with impregnated SrFe0.75Mo0.25O3−δ electrodes.* Journal of Power Sources, 2014. **252**: p. 58-63.
49. Lakshminarayanan, N., et al., *Doped LaFeO3 as SOFC catalysts: Control of oxygen mobility and oxidation activity.* Catalysis Today, 2010. **157**(1): p. 446-450.
50. Sunarso, J., et al., *Mixed ionic–electronic conducting (MIEC) ceramic-based membranes for oxygen separation.* Journal of Membrane Science, 2008. **320**(1): p. 13-41.
51. Park, J.W. and K.T. Lee, *Enhancing performance of La0.8Sr0.2MnO3−δ-infiltrated Er0.4Bi1.6O3 cathodes via controlling wettability and catalyst loading of the precursor solution for IT-SOFCs.* Journal of Industrial and Engineering Chemistry, 2018. **60**: p. 505-512.
52. De Souza, R.A. and J.A. Kilner, *Oxygen transport in La1−xSrxMn1−yCoyO3±δ perovskites: Part I. Oxygen tracer diffusion.* Solid State Ionics, 1998. **106**(3): p. 175-187.
53. Strandbakke, R., et al., *Reaction kinetics of protons and oxide ions in LSM/lanthanum tungstate cathodes with Pt nanoparticle activation.* Journal of The Electrochemical Society, 2016. **163**(6): p. F507-F515.
54. Wu, T., et al., *Nano-sized Sm0.5Sr0.5CoO3−δ as the cathode for solid oxide fuel cells with proton-conducting electrolytes of BaCe0.8Sm0.2O2.9.* Electrochimica Acta, 2009. **54**(21): p. 4888 - 4892.
55. Sahibzada, M., et al., *Development of solid oxide fuel cells based on a Ce(Gd)O2−x electrolyte film for intermediate temperature operation.* Catalysis Today, 1997. **38**(4): p. 459-466.
56. Grimaud, A., et al., *Hydration properties and rate determining steps of the oxygen reduction reaction of perovskite-related oxides as H+-SOFC cathodes.* Journal of The Electrochemical Society, 2012. **159**(6): p. B683-B694.

57. Patrakeev, M.V., et al., *Ion–electron transport in strontium ferrites: relationships with structural features and stability.* Solid State Sciences, 2004. **6**(9): p. 907-913.
58. Zohourian, R., et al., *Mixed-Conducting Perovskites as Cathode Materials for Protonic Ceramic Fuel Cells: Understanding the Trends in Proton Uptake.* Advanced Functional Materials, 2018. **28**(35): p. 1801241.
59. Goupil, G., et al., *Stability study of possible air electrode materials for proton conducting electrochemical cells.* Solid State Ionics, 2012. **209-210**: p. 36-42.
60. Jarry, A., et al., *Rare earth effect on conductivity and stability properties of doped barium indates as potential proton-conducting fuel cell electrolytes.* Solid State Ionics, 2012. **216**: p. 11-14.
61. Goupil, G., et al., *Selection and study of basic layered cobaltites as mixed ionic–electronic conductors for proton conducting fuel cells.* Solid State Ionics, 2014. **263**: p. 15-22.
62. Hermet, J., B. Dupé, and G. Dezanneau, *Simulations of REBaCo2O5.5 (REGd, La, Y) cathode materials through energy minimisation and molecular dynamics.* Solid State Ionics, 2012. **216**: p. 50-53.
63. Lin, Y., et al., *Evaluation of Ba0.5Sr0.5Co0.8Fe0.2O3−δ as a potential cathode for an anode-supported proton-conducting solid-oxide fuel cell.* Journal of Power Sources, 2008. **180**(1): p. 15-22.
64. Ding, H. and X. Xue, *Novel layered perovskite GdBaCoFeO5+δ as a potential cathode for proton-conducting solid oxide fuel cells.* International Journal of Hydrogen Energy, 2010. **35**(9): p. 4311-4315.
65. Chang, A., S.J. Skinner, and J.A. Kilner, *Electrical properties of GdBaCo2O5+x for ITSOFC applications.* Solid State Ionics, 2006. **177**(19): p. 2009-2011.
66. Peng, R., et al., *Cathode processes and materials for solid oxide fuel cells with proton conductors as electrolytes.* Journal of Materials Chemistry, 2010. **20**(30): p. 6218-6225.
67. Ni, M., M.K.H. Leung, and D.Y.C. Leung, *Mathematical Modelling of Proton‐Conducting Solid Oxide Fuel Cells and Comparison with Oxygen‐Ion‐Conducting Counterpart.* Fuel Cells, 2007. **7**(4): p. 269-278.
68. Strandbakke, R., *Oxygen electrodes for ceramic fuel cells with proton and oxide ion conducting electrolytes*. 2014.
69. Ricote, S., et al., *LaCoO3: Promising cathode material for protonic ceramic fuel cells based on a BaCe0.2Zr0.7Y0.1O3−δ electrolyte.* Journal of Power Sources, 2012. **218**: p. 313-319.
70. Zhao, L., et al., *Reaction model for cathodes cooperated with oxygen-ion conductors for solid oxide fuel cells using proton-conducting electrolytes.* International Journal of Hydrogen Energy, 2012. **37**(1): p. 548-554.
71. Uchida, H., S. Tanaka, and H. Iwahara, *Polarization at Pt electrodes of a fuel cell with a high temperature-type proton conductive solid electrolyte.* Journal of applied electrochemistry, 1985. **15**(1): p. 93-97.
72. Kim, J.-D., et al., *Characterization of LSM–YSZ composite electrode by ac impedance spectroscopy.* Solid State Ionics, 2001. **143**(3): p. 379-389.
73. Fleig, J., *Solid Oxide Fuel Cell Cathodes: Polarization Mechanisms and Modeling of the Electrochemical Performance.* Annual Review of Materials Research, 2003. **33**(1): p. 361-382.
74. Norby, T. and P. Kofstad, *Electrical Conductivity and Defect Structure of Y2O3 as a Function of Water Vapor Pressure.* Journal of the American Ceramic Society, 1984. **67**(12): p. 786-792.

75. Tsvetkov, D.S., et al., *Oxygen content, cobalt oxide exsolution and defect structure of the double perovskite PrBaCo2O6−δ.* Journal of Materials Chemistry A, 2016. **4**(5): p. 1962-1969.
76. Kreuer, K.D., *On the complexity of proton conduction phenomena.* Solid State Ionics, 2000. **136-137**: p. 149-160.
77. Kochetova, N., et al., *Recent activity in the development of proton-conducting oxides for high-temperature applications.* RSC Advances, 2016. **6**(77): p. 73222-73268.
78. Miyoshi, S., et al., *Rate-determining elementary step of oxygen reduction reaction at (La,Sr)CoO3-based cathode surface.* Solid State Ionics, 2016. **285**: p. 202-208.
79. Robinson, S.A., *Development of Cu-based electrodes for proton-conducting membrane reactors.* 2017.

Appendix A

Calculation of the Rate-Determining Step (Example)

If step 2 is the RDS, step 1 and steps 3-6 are in virtual equilibrium:

$$\mathrm{r}_2 = \mathrm{k}_2^{+}\Theta_{\mathrm{O}_{\mathrm{BGLC(ads)}}} - \mathrm{k}_2^{-}\Theta_{\mathrm{O}^{2-}_{\mathrm{BGLC(ads)}}} \tag{A.1}$$

The equilibrium expressions are:

$$\Theta_{\mathrm{O}_{\mathrm{BGLC(ads)}}} = \left(\frac{\mathrm{k}_1^{+}}{\mathrm{k}_1^{-}}\right)^{\frac{1}{2}} p\mathrm{O}_2^{\frac{1}{2}} \tag{A.2}$$

$$\Theta_{\mathrm{O}^{2-}_{\mathrm{BGLC(ads)}}} = \frac{1}{\mathrm{K}_6\mathrm{K}_5\mathrm{K}_4\mathrm{K}_3^2}\frac{1}{a^2_{\mathrm{H}^{+}_{\mathrm{El.l}}}}p\mathrm{H}_2\mathrm{O}\ \exp\left(\frac{2\mathrm{FE}}{\mathrm{RT}}\right) \tag{A.3}$$

When a net current is running, the anodic and cathodic reaction rates, respectively, becomes:

$$i_a = \mathrm{nFk}_2^{-}\Theta_{\mathrm{O}^{2-}_{\mathrm{BGLC(ads)}}}\exp\left(\frac{\mathrm{FE}}{\mathrm{RT}}\right) = \mathrm{nFk}_2^{-}\frac{1}{\mathrm{K}_6\mathrm{K}_5\mathrm{K}_4\mathrm{K}_3^2}\mathrm{pH}_2\mathrm{O}\ \exp\left(\frac{\mathrm{FE}}{\mathrm{RT}}\right) \tag{A.4}$$

$$i_c = \mathrm{nFk}_2^{+}\Theta_{\mathrm{O}_{\mathrm{BGLC(ads)}}}\exp\left(-\frac{\mathrm{FE}}{\mathrm{RT}}\right) = \left(\frac{\mathrm{k}_1^{+}}{\mathrm{k}_1^{-}}\right)^{\frac{1}{2}} p\mathrm{O}_2^{\frac{1}{2}}\exp\left(-\frac{\mathrm{FE}}{\mathrm{RT}}\right) \tag{A.5}$$

The total rate:

$$i_2 = \mathrm{nFk}_2^{-}\frac{1}{\mathrm{K}_6\mathrm{K}_5\mathrm{K}_4\mathrm{K}_3^2}p\mathrm{H}_2\mathrm{O}\ \exp\left(\frac{\mathrm{FE}}{\mathrm{RT}}\right) - \left(\frac{\mathrm{k}_1^{+}}{\mathrm{k}_1^{-}}\right)^{\frac{1}{2}} p\mathrm{O}_2^{\frac{1}{2}}\exp\left(-\frac{\mathrm{FE}}{\mathrm{RT}}\right) \tag{A.6}$$

RDS causes the overpotential, thus $\eta = E - E_N$.

By inserting in Butler-Volmer equation, assume $\beta = ½$:

$$i_{0,2} = i_a = i_c = n\mathrm{F}\mathrm{k}_{2,*}^{-}\, p\mathrm{H_2O}\, \exp\left(\frac{\mathrm{F}\eta}{\mathrm{RT}}\right) = n\mathrm{F}\mathrm{k}_{2,*}^{+}\, p\mathrm{O}_2^{\frac{1}{2}} \exp\left(-\frac{\mathrm{F}\eta}{\mathrm{RT}}\right) \qquad (\mathrm{A}.7)$$

The rate constant with subscript $*$ includes all rate constants.

The reaction order of the rate-determining step is proportional to:

$$i_{0,2} \propto p\mathrm{O}_2^{\frac{1}{2}}\, p\mathrm{H_2O}^0 \qquad (\mathrm{A}.8)$$